

# Development of Laser-Spectroscopic Techniques for New Detection Schemes in Combustion Diagnostics

Doctoral Dissertation

Johan Zetterberg

Division of Combustion Physics  
Department of Physics



LUND UNIVERSITY

© 2001-2008 Johan Zetterberg and the respective publishers  
Printed at Tryckeriet i E-huset, Lund, Sweden  
January 2008

Lund Reports on Combustion Physics, LRCP 124  
ISSN 1102-8718  
ISRN LUTFD2/TFCP--08/124--SE  
ISBN 978-91-628-7392-9

Johan Zetterberg  
Division of Combustion Physics  
Department of Physics  
Lund University  
P.O. Box 118  
SE-221 00 Lund, Sweden

*Till min familj*



# Abstract

The thesis work, aimed at the development of laser-spectroscopic detection schemes, consists of three parts, concerned with the development and application of different techniques. The development of UV filtered Rayleigh scattering (FRS) for thermometry and fuel/air ratio measurements, using a frequency tripled, single-longitudinal-mode alexandrite laser at  $\sim 254$  nm together with an isotopically enhanced mercury filter, is examined first. Mercury has almost ideal features for serving as an atomic filter, having sharp cut-off slopes and a high extinction ratio, making it possible to effectively block unbroadened scattered light from particles, for example, and still let Doppler broadened light from the gas-phase pass through. The S6-model was utilized to model the Rayleigh-Brillouin scattering lineprofile. The FRS was employed in several applications, the thermometry measurements agreeing well with earlier measurements and calculations. Fuel/air ratio measurements were also obtained, various preliminary results being discussed.

A second area considered was use of polarization spectroscopy (PS) to probe species relevant to combustion. The CH radical was studied in a low-pressure methane/oxygen flame and compared with laser-induced fluorescence (LIF) measurements acquired simultaneously. Atomic hydrogen was imaged at ambient pressure in a hydrogen/oxygen flame, utilizing a two-photon-pump polarization spectroscopy probe (TPP-PSP) approach in which a 243 nm laser beam was used to excite the atoms through a two-photon process to the  $2s$  state. The  $2s$  state was then probed by use of the  $2s$ - $4p$  transition through a PS scheme employing 486 nm. PS was also extended into the mid-infrared spectral regime and used to probe ro-vibrational transitions of species not accessible in the UV and visible spectral range. Use of infrared PS (IRPS) for detection of minor species such as OH and  $C_2H_2$  produced in flames, as well as of stable species such as  $CO_2$ ,  $CH_4$  and  $H_2O$  was demonstrated. The signal-to-noise ratio obtained was higher than for IRLIF.

Finally, the development of planar LIF (PLIF) for CH involving improved detection sensitivity for a single-shot investigation of lean and turbulent premixed flames was reported. An alexandrite laser characterized by a long pulse duration ( $\sim 150$  ns) and the possibility to operate both in a single-mode manner with a narrow bandwidth ( $\sim 100$  MHz) and in a multimode manner with a broad bandwidth ( $\sim 8$   $cm^{-1}$ ), was utilized to excite the B-X (0,0) band. A sharp and thin CH layer was visible from  $\Phi = 0.6$  to  $\Phi = 1.5$  in methane/air flames. Finally, use of the technique in a lean and partially premixed methane/air flame in a co-axial jet flame burner was demonstrated.



# Sammanfattning

Förbränning förknippas av många som förlegat. Att utvinna energi genom att "elda" har människan gjort under årtusenden, men trots det bestod Sveriges totala energiproduktion 2004 till 52 % av förbränning. De flesta bilar, båtar, flyg och i vissa fall även tåg utnyttjar den kemiskt lagrade energin i fossila bränslen. Uppvärmningen av bostäder är inte heller att förringa, där olja fortfarande har en betydande roll.

Under det gångna decenniet har diskussionen om växthuseffekten stadigt ökat i både internationella och nationella medier och nådde sin kulmen 2007 då Al Gore och FN:s klimatpanel erhöll Nobels fredspris för sina insatser.

Oberoende av vilket bränsle som väljs så ger förbränning upphov till föroreningar, inte bara koldioxid (som tills för ett antal år sedan ansågs som mer eller mindre helt ofarlig) utan även kväveoxider, svaveloxider, sot och oförbrända kolväten är föroreningar som förbränning för med sig. Kväveoxider och sot till exempel, uppkommer även vid förbränning av biobränslen. För att kunna minska de olika utsläppen krävs en djup förståelse för de komplexa, fundamentala processer som styr förbränningen. Att förstå flöden, koncentrationer av olika ämnen och temperaturer vid olika tidpunkter i förbränningsprocessen är avgörande för effektivare och miljömässigt godtagbar förbränning.

I denna doktorsavhandling beskrivs utvecklingen av ett antal laserspektroskopiska mätmetoder för att studera just dessa parametrar. Lasermätmetoder har stora fördelar jämfört med traditionella mätmetoder, med en möjlighet att mäta väldigt snabba förlopp (kortare än en miljarddel sekund), väldigt små strukturer i rummet (ner till nästan 50 miljontedels meter) och i princip beröringsfritt, det vill säga utan att påverka förbränningen.

I avhandlingen beskrivs bland annat hur noggranna temperaturmätningar kan göras genom att studera spritt ljus från molekyler. Molekylernas hastighet beror på temperaturen, därför kan Dopplerbreddningen på det spridda ljuset utnyttjas för att ta reda på temperaturen i till exempel en flamma eller en gnistcell. Mätmetoden kallas filtrerad Rayleighspridning och mäter, med 5-10 % noggrannhet, temperaturer upp emot 2000 °C utan att störa förbränningen. Filtrerad Rayleigh spridning och har i arbetet tillämpats vid olika situationer.

Polarisationsspektroskopi är en annan metod som har utvecklats och använts i avhandlingen. Den kan användas till att exempelvis mäta ämnens koncentrationer med hög noggrannhet och i väldigt små kvantiteter. Mycket av de studier som har genomförts i avhandlingen ligger i det infraröda området, dvs. värmestrålning. Här

kan nämligen molekyler studeras som inte kan nås i det synliga eller ultravioletta området. Resultaten resulterar i stor utsträckning i spektrum från olika molekyler, och eftersom ett spektrums utseende förändras med temperaturen kan även den bestämmas med denna metod.

Den sista metoden som har utnyttjats i arbetet är laser inducerad fluorescence. Med hjälp av fluorescence kan bland annat strukturer i turbulenta flammor studeras. Turbulent förbränning anses idag som en god möjlighet att både få effektivare förbränning med lägre bränsleförbrukning och mindre utsläpp.

Molekylen CH, lyser med den blålila färg som man kan se runt ett stearinljus, markerar flamfronten och är därför viktig i förbränningen. Flamfronten är där själva förbränningen startar och är viktig att förstå.

En fortsatt utveckling av lasermätmetoder är en förutsättning för att vi ska kunna öka vår förståelse och kunskap om alla de processer som styr förbränningen. Med ökad förståelse och kunskap finns det utsikter att kunna effektivisera värmekraftverk och bilmotorer samt minska utsläppen – minskade utsläpp är trots allt nog den enda lösningen till en hållbar utveckling, både kort och på lång sikt.

# List of papers

- I. Li, Z.S., Afzelius, M., Zetterberg, J., and Aldén, M., *Applications of a single-longitudinal-mode alexandrite laser for diagnostics of parameters of combustion interest*. Review of Scientific Instruments, **75**:3208-3215, 2004
- II. Zetterberg, J., Li, Z.S., Afzelius, M., and Aldén, M., *Two-dimensional temperature measurements in flames using filtered Rayleigh scattering at 254 nm*. Submitted to Applied Spectroscopy, 2008
- III. Petersson, P., Olofsson, J., Brackman, C., Seyfried, H., Zetterberg, J., Richter, M., Aldén, M., Linne, M.A., Cheng, R.K., Nauert, A., Geyer, D., and Dreizler, A., *Simultaneous PIV/PH-PLIF, Rayleigh thermometry/OH-PLIF and stereo PIV measurements in a low-swirl-flame*. Applied Optics, **46**:3928-3936, 2007
- IV. Brübach, J., Zetterberg, J., Omrane, A., Li, Z.S., Aldén, M., and Dreizler, A., *Determination of surface normal temperature gradients using thermographic phosphors and filtered Rayleigh scattering*. Applied Physics B-Lasers and Optics, **84**:537-541, 2006
- V. Kiefer, J., Li, Z.S., Zetterberg, J., Linvin, M., and Aldén, M., *Simultaneous laser-induced fluorescence and sub-Doppler polarization spectroscopy of the CH radical*. Optics Communications, **270**:347-352, 2007
- VI. Linvin, M., Li, Z.S., Zetterberg, J., and Aldén, M., *Single-shot imaging of ground-state hydrogen atoms with a nonlinear laser spectroscopic technique*. Optics Letters, **32**:1569-1571, 2007
- VII. Alwahabi, Z.T., Zetterberg, J., Li, Z.S., and Aldén, M., *High resolution polarization spectroscopy and laser induced fluorescence of CO<sub>2</sub> around 2 μm*. European Physical Journal D, **42**:41-47, 2007
- VIII. Li, Z.S., Rupinski, M., Zetterberg, J., Alwahabi, Z.T., and Aldén, M., *Detection of methane with mid-infrared polarization spectroscopy*. Applied Physics B-Lasers and Optics, **79**:135-138, 2004
- IX. Li, Z.S., Rupinski, M., Zetterberg, J., and Aldén, M., *Mid-infrared PS and LIF detection of CH<sub>4</sub> and C<sub>2</sub>H<sub>6</sub> in cold flows and flames at atmospheric pressure*. Proceedings of the Combustion Institute, **30**:1629-1636, 2005

- X. Li, Z.S., Linvin, M., Zetterberg, J., Kiefer, J., and Aldén, M., *Mid-infrared polarization spectroscopy of C<sub>2</sub>H<sub>2</sub>: Non-intrusive spatial-resolved measurements of polyatomic hydrocarbon molecules for combustion diagnostics*. Proceedings of the Combustion Institute, **31**:817-824, 2007
- XI. Li, Z.S., Rupinski, M., Zetterberg, J., Alwahabi, Z.T., and Aldén, M., *Mid-infrared polarization spectroscopy of polyatomic molecules: Detection of nascent CO<sub>2</sub> and H<sub>2</sub>O in atmospheric pressure flames*. Chemical Physics Letters, **407**:243-248, 2005
- XII. Li, Z.S., Hu, C.H., Zetterberg, J., Linvin, M., and Aldén, M., *Midinfrared polarization spectroscopy of OH and hot water in low pressure lean premixed flames*. Journal of Chemical Physics, **127**:084310-1-9, 2007
- XIII. Li, Z.S., Kiefer, J., Zetterberg, J., Linvin, M., Leipertz, A., Bai, X.S., and Aldén, M., *Development of improved PLIF CH detection using an Alexandrite laser for single-shot investigation of turbulent and lean flames*. Proceedings of the Combustion Institute, **31**:727-735, 2007

## Related work

- A. Nogenmyr, K.J., Petersson, P., Bai, X.S., Nauert, A., Olofsson, J., Brackman, C., Seyfried, H., Zetterberg, J., Li, Z.S., Richter, M., Dreizler, A., Linne, M., and Aldén, M., *Large eddy simulation and experiments of stratified lean premixed methane/air turbulent flames*. Proceedings of the Combustion Institute, **31**:1467-1475, 2007
- B. Alwahabi, Z.T., Li, Z.S., Zetterberg, J., and Aldén, M., *Infrared polarization spectroscopy of CO<sub>2</sub> at atmospheric pressure*. Optics Communications, **233**:373-381, 2004
- C. Alwahabi, Z.T., Zetterberg, J., Li, Z.S., and Aldén, M., *Measurements of collisional broadening coefficients by infrared polarization spectroscopy*. Applied Spectroscopy, **61**:424-427, 2007
- D. Kiefer, J., Li, Z.S., Zetterberg, J., Bai, X.S., and Aldén, M., *Investigation of local jet flames using simultaneous single-shot CH and OH planar laser-induced fluorescence imaging*. Submitted to Combustion and Flames, 2008



# Contents

Abstract.....	i
Sammanfattning.....	iii
List of papers.....	iii
Related work.....	vii
Contents .....	ix
Chapter 1 – Introduction .....	1
1.1 Laser diagnostics.....	2
1.2 Thesis outline.....	3
Chapter 2 – Experimental apparatus .....	5
2.1 The Nd:YAG laser.....	5
2.2 Tunable laser systems .....	6
2.5.1 Dye laser .....	7
2.5.2 Optical Parametric Oscillator, OPO.....	8
2.3 Frequency extension .....	8
2.4 The Alexandrite laser.....	9
2.5 Detectors.....	12
2.5.1 Photodiode .....	13
2.5.2 Photomultiplier tube, PMT .....	13
2.5.3 ICCD camera.....	14
2.5.4 Infrared detectors .....	15
2.6 Optical components .....	16
2.6.1 From UV to IR. What materials to choose. ....	17
2.6.2 Polarizers.....	18
2.7 Burners .....	18
2.7.1 Co-axial jet flame burner.....	19
2.7.2 Low-swirl burner.....	20
2.7.3 Wolfhard-Parker burner.....	21
2.7.4 The porous plug burner .....	21
Chapter 3 – Filtered Rayleigh scattering (FRS).....	23
3.1 Basic features of filtered Rayleigh scattering (FRS).....	23

3.2	The mercury absorption filter.....	24
3.2.1	Mercury as a filter candidate.....	24
3.2.2	Characterization of the mercury absorption filter.....	25
3.2.3	Experimental setup and measurements .....	26
3.3	Rayleigh - Brillouin scattering .....	27
3.3.1	Rayleigh scattering cross-section.....	28
3.3.2	Lineshapes of Rayleigh-Brillouin scattering .....	30
3.4	Filtered Rayleigh scattering theory.....	32
3.5	Experimental setup.....	34
3.6	The application of FRS in combustion diagnostics .....	35
3.6.1	Thermometry measurements in fuel-rich, premixed flames.....	35
3.6.2	Thermometry measurements in a lean, premixed, low-swirl burner ...	36
3.6.3	Thermometry measurements in a Wolfhard-Parker diffusion flame..	38
3.6.4	Temperature gradients close to surfaces .....	39
3.6.5	Temperature measurements in an ignition cell .....	40
3.6.6	Fuel/air ratio measurements .....	43
Chapter 4	– Polarization spectroscopy (PS) .....	45
4.1	Introduction to polarization spectroscopy.....	45
4.2	Basic concepts of polarization spectroscopy .....	46
4.2.1	Line profiles of the PS-signal .....	48
4.2.2	PS-signal dependence on laser fluence .....	50
4.3	Application of PS in combustion diagnostics .....	51
4.3.1	Detection of the CH radical through PS .....	52
4.3.2	Imaging of hydrogen atoms in flames .....	53
4.3.3	Infrared polarization spectroscopy of combustion related species .....	55
Chapter 5	– Laser-induced fluorescence (LIF) .....	61
5.1	A basic account of laser-induced fluorescence .....	61
5.2	Laser-induced fluorescence for CH detection .....	63
5.3	Mid-infrared laser-induced fluorescence (IRLIF) .....	66
Chapter 6	– Summary and outlook .....	69
Bibliography	.....	71
Acknowledgements	.....	85
Summary of papers.....		89

# Chapter 1

## Introduction

Mankind has always had a fascination for combustion, which has dictated people's lives in many respects, and continues doing so today. Combustion has been important in all cultures and throughout most of human history, as representing the only or most effective way of lighting up the night, maintaining the warmth and preparing the food in more than raw form.

Already around the year 1600 the Flemish physicist and alchemist Johann van Helmont (1577-1644) conducted some detailed studies of combustion, realizing that the "air-like" thing created in the process was indeed not air. He coined the word *gas*, probably a Flemish transcription of the Greek word "chaos" that Paracelsus (1493-1541) had used to describe air, and specifically named carbon dioxide *gas sylvestre* [1]. This was, in a way, the first study of combustion products. Today the word *gas* as such is used in several different languages and at present, some 400 years later, and the study of combustion processes is conducted to a large extent by studying the flow, temperatures and concentrations of gases.

The industrial revolution was made possible by the discovery of coal and oil and is that which led to the prosperity in the world today. The need of energy at

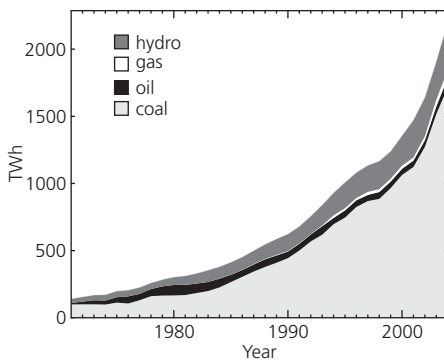


**Figure 1.1** Evolution of the generation of electricity in P.R. China by fuel from 1971 to 2004. [2]

present is greater than ever and the use of fossil fuel for combustion is increasing all the time. China can be mentioned as an example. The development of industry and the increase in production have boosted the demand for electricity there enormously, as shown in Fig. 1.1, concerning the production of electricity in China [2]. The increase in the production of electricity in China has almost been exponential and is today more than ten times as high as 30 years ago. The energy source of the increase has been coal, due mainly to the large amounts of coal found in China. At present, combustion is the dominant energy

source there, as it is in the rest of the world, its providing more than 97 % of the total energy production.

During the last few years, the concern for global warming has peaked and is on everyone's lips. Scientists have not arrived at a complete consensus, but most signs indicate that the addition to global warming that man has created disturbs the sensitive nature appreciably. The combustion of fossil fuel releases large amounts of carbon dioxide. Carbon dioxide, being a product species in hydrocarbon combustion impossible to avoid, is a greenhouse gas. In addition, combustion is associated with other emissions, such as of  $\text{NO}_x$ ,  $\text{SO}_x$ , soot, unburned hydrocarbons and CO, each emission having its own effect on the environment; smog is created by  $\text{NO}_x$  and soot, while  $\text{SO}_x$  and  $\text{NO}_x$  contribute to acidification, and so on.

The demand for energy in Europe has been stable for the last ten years and dependence on coal has decreased. The creation and development of new energy sources and the exploitation of established alternatives to use of fossil fuel is the only solution to the need of decreasing emissions. According to the International Energy Agency (IEA), however, achieving this to any marked degree at present seems unlikely, its appearing that fossil fuel will be the dominant source of energy in the foreseeable future. It should also be noted that even if the demand for fossil fuel decrease, use of combustion will probably be almost as great as before through the combustion of biomass and waste.

Although there are no simple solutions to the problems here, it is absolutely essential that the level of emissions be lowered. Combustion research aimed at gaining an understanding of the fundamental mechanisms of combustion and at being able to predict its behaviour and control it is thus highly important. Questions of overall efficiency need to be addressed. Investigations of biofuel combustion, which creates new challenges for engineers and combustion scientists, are important here. In order to address the various problems that exist, both measurements and modelling of the processes involved are needed. These can provide a better understanding of the processes and enable more efficient devices with low emission levels to be constructed.

## 1.1 Laser diagnostics

Laser diagnostic techniques represent a highly effective way of measuring quantities related to combustion processes [3,4]. Optical techniques have certain advantages as compared with traditional probing techniques, especially the possibility of measuring *in situ* without disturbing the measurement region, at least if used wisely. When high spatial and temporal resolution is sought, laser diagnostics is generally needed.

The temporal resolution achieved by use of laser diagnostics is determined by the length of the laser pulse and the lifetime of the process probed which may be as

short as tens of femtoseconds. In combustion diagnostics, the most utilized lasers have a typical pulse length of  $\sim 10$  ns. This is usually sufficient for the combustion process to be considered as stable or as “frozen” on this time scale.

In most diagnostics, high spatial resolution is essential. Through two-dimensional detectors such as ICCD cameras (discussed in Chapter 2), images of the process involved can be obtained in which the spatial resolution in the  $x$ - and  $y$ -directions is determined by the imaging optics and the intensifier and CCD-chip of the ICCD camera. A high resolution in the  $z$ -direction as well can be achieved by focusing the laser in the measurement region properly, a resolution of  $\sim 50$   $\mu\text{m}$  in all directions being attainable then.

This thesis is concerned with new detection schemes for measuring quantities relevant to combustion. Having knowledge of the temperature, the species distributions/concentrations and the velocity fields involved is of central importance to an understanding of the combustion processes occurring. In the thesis, means of utilizing filtered Rayleigh scattering, polarization spectroscopy and laser-induced fluorescence to measure these quantities are developed and applications of them studied.

## **1.2 Thesis outline**

The three chapters concerned with these techniques (chapters 3, 4 and 5) can each be considered more or less stand-alone.

In Chapter 2 most of the experimental equipment used during the present experimental work is described and its specifications examined in detail. Chapter 3 describes the development and utilization of filtered Rayleigh scattering for temperature and fuel/air ratio measurements, applications of it in both sooty and lean combustion being reported. Polarization spectroscopy for detection of minor species, with an emphasis on the mid-infrared spectral region, is taken up in Chapter 4, and the visualization of minor species, especially of CH, for flame-front detection by means of laser-induced fluorescence, together with infrared laser-induced fluorescence measurements of  $\text{CO}_2$  in Chapter 5. The work conducted is summarized then and a view of possible future developments presented in Chapter 6.



# Chapter 2

## Experimental apparatus

In modern, experimental science, apparatus is highly important. In order to obtain reliable, sensitive, time- and spectrally-resolved measurements, use of well characterized equipment is essential. In the present chapter, a brief account of the main pieces of equipment used in the present work is provided. Laser-diagnostic techniques generally require advanced and complex setups. The variety of laser-diagnostic and spectroscopic techniques employed in the thesis work have required the use of several different laser systems and detectors. The lasers employed have all been flashlamp-pumped, Q-switched lasers, each of them having high peak power and fairly short pulse durations.

### 2.1 The Nd:YAG laser

The Nd:YAG laser is the most commonly employed high-power pulsed laser system. It is used in a variety of applications, such as for pumping dye-lasers or Ti:sapphire lasers and for direct measurements, such as in fuel and formaldehyde visualisation [5-7] and particle-induced velocimetry (PIV). The Nd:YAG laser is a solid-state laser in which the active medium is the neodymium doped yttrium-aluminium-garnet crystal  $Y_3Al_5O_{12}$ . It is a four-level system in which the lasing occurs between the third and the fourth level, as shown in Fig. 2.1.

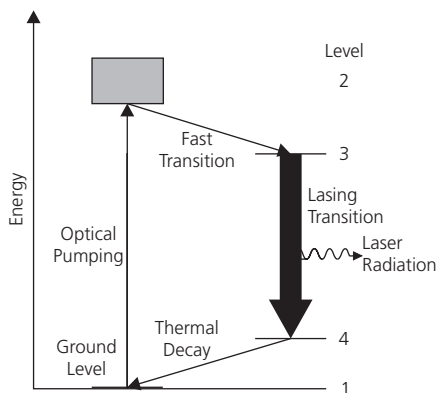


*Figure 2.1 Schematic energy level diagram of the Nd:YAG laser.*

The Nd:YAG is non-tuneable and has a fundamental output of 1064 nm. Through frequency conversion, doubling, tripling and quadrupling, 532 nm, 355 nm and 266 nm can all be at high peak-power when reached. The laser has a

typical pulse duration of 8-10 ns and runs at a 10 Hz repetition rate. Its peak power can exceed 2.5 J at 1064 nm, although the systems used in the present work range from 400 – 1000 mJ at 532 nm. For a more complete and thorough account of the Nd:YAG laser see ref. [8,9].

Two different Nd:YAG laser systems were employed in the applications involved in the present work. First, a Spectra-Physics<sup>TM</sup> Quanta-Ray Pro-290 was used to pump both an optical parametric oscillator (OPO) and a Sirah dye laser (both will be described later). This work is taken up in Papers VIII-XII. The system is a very powerful injection-seeded, single-mode Nd:YAG laser having an excellent beam profile and high reliability. In addition, a Continuum NY82-10 was utilized to pump a dye laser in the OH-LIF measurements reported in Paper D. Still a further useful laser is the Brilliant B from Quantel. This very small and handy laser system without external cooling is capable of delivering high-power, pulsed emission at a 10 Hz repetition rate. A dual version of it was used for the PIV measurements reported in Paper III.

The major specifications of these three different lasers are presented in Table 2.1 for comparison purposes.

*Table 2.1 The specifications of the different Nd:YAG laser systems employed as provided by the producers, [10-12]. The Continuum laser was outfitted with injection seeding, although this was not in function at the time. In the case of injection seeding, both the linewidth and the pulse energy are affected.*

Output Characteristics	Spectra-Physics <sup>TM</sup> Quanta-Ray Pro-290	Quantel Brilliant B	Continuum NY82-10
$E_{pulse}$ at 1064 nm	2000 mJ	850 mJ	1800 mJ
$E_{pulse}$ at 532 nm	1000 mJ	400 mJ	900 mJ
$E_{pulse}$ at 355 nm	550 mJ	165 mJ	450 mJ
$E_{pulse}$ at 266 nm	180 mJ	90 mJ	200 mJ
Pulse duration	8-12 ns at 1064 nm	~6 ns	7-10 ns at 1064 nm
Repetition rate	10Hz	10 Hz	10 Hz
Line width	<0.003 cm <sup>-1</sup>	0.7 cm <sup>-1</sup>	1 cm <sup>-1</sup>

## 2.2 Tunable laser systems

A large variety of wavelengths are needed in order to be able to obtain species-specific measurements. The Nd:YAG lasers described above can only supply a very limited range of wavelengths. Use of other laser sources in addition is essential in order to reach other more specific wavelengths. In the present work both dye lasers (in Papers VIII-XII and D) and an optical parametric oscillator (in Paper VI) have been employed. These are described briefly below.

### 2.5.1 Dye laser

The dye laser is the type of tuneable laser that is used most. It differs fundamentally from the Nd:YAG laser. In a dye laser the active medium consists of a solution of an organic dye in a liquid solvent. Many different solvents can be used, but in all of the measurements conducted only methanol was used as a solvent. The dye generally consists of polyatomic molecules containing long chains

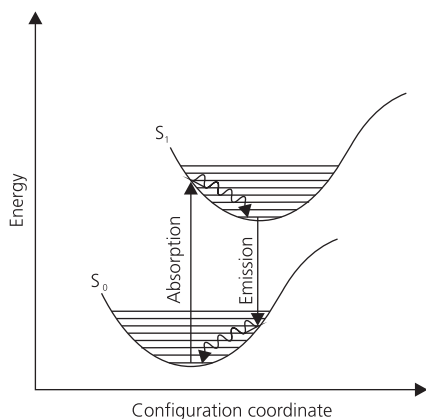


*Figure 2.2 A simplified schematic energy level diagram of the dye laser principle, the configuration coordinate is a coordinate describing the vibrational modes of the dye molecule.*

of conjugated double bonds. A simplified energy level diagram is shown in Fig. 2.2. In the figure it can be seen that the dye laser functions in accordance with a four level scheme. The molecules are excited to a high electronic energy level, where they quickly ( $\sim 100$  fs) relax down to the ground vibrational level of the electronically excited state. Taking account of the Franck-Condon principle, lasing can occur here between the upper ground vibrational state and several lower vibrational states. Through broadening mechanisms, the lower vibrational states create a fluorescent continuum, giving the dye laser its tunability. The molecule undergoes then rapid non-radiative decay within the ground state, becoming depopulated to the lowest vibrational state.

A problem in connection with dye lasers is that the lifetime of the upper state is very short. Thus, the pumping power that goes into the dye laser needs to be high in order for a sufficiently large population to be obtained in the upper state.

The dye lasers used in these measurements are all high-peak-power, pulsed lasers pumped by pulsed Nd:YAG lasers at 532 nm. For the OH-LIF measurements presented in Paper D, use was made of a Continuum ND60 dye laser, one that has a tuning range of between 380 nm and 740 nm. In most of the IRPS measurements in Chapter 4 and in Papers VIII-XII, a Spectra-Physics<sup>TM</sup> Quanta-Ray Pro-290 was used to pump a Sirah, PrecisionScan PRSC-D-18 dye laser. The Sirah dye laser has a narrow linewidth,  $0.05\text{ cm}^{-1}$  at 625 nm, a tuning range of 410 – 900 nm and an 1800 groves/mm grating, although the active medium needs to be changed to encompass the entire range. It delivers a pulse energy of  $\sim 75$  mJ at 810 nm [13].

## 2.5.2 Optical Parametric Oscillator, OPO

The OPO laser is not a laser in the classic sense. It was demonstrated experimentally for the first time in 1965 [14]. The lasers discussed thus far derive their gain from stimulated emission generated by atomic transitions. The OPO laser in contrast, is based instead on frequency conversion. It needs to be pumped by another high energy laser. It contains a non-linear crystal, one that is usually a BBO-crystal, used to convert the energy of an incoming pump photon with a frequency,  $\omega_p$ , to a signal and an idler photon, the frequencies of the two being,  $\omega_s$  and  $\omega_i$ , respectively. These frequencies are related by  $\omega_p = \omega_s + \omega_i$ , their relations being determined by the phase-matching condition [15,16], ascertaining in practical terms this being done by tuning the angle of the non-linear crystal.

For measurements of hydrogen atoms, discussed in Chapter 4 and in Paper VI the Spectra-Physics<sup>TM</sup> Quanta-Ray Pro-290 was used to pump the OPO resonator (Spectra-Physics<sup>TM</sup> MOPO-730) with 355 nm. The output of the signal and the idler can be tuned to 356 – 1000 nm and 440 – 2000 nm, respectively. A frequency-doubling option allows 220 – 345 nm to be reached. The intracavity dispersive elements yield a linewidth of 0.07 cm<sup>-1</sup>.

There are several pros and cons of an OPO system as compared with other tuneable systems. One advantage is the possibility it provides of achieving a large wavelength range without a change in the lasing medium. The OPO system is very sensitive, however, and needs to be pumped by lasers with a high quality beam profile.

## 2.3 Frequency extension

The Sirah dye laser is equipped with a frequency extension unit that can be used either for frequency doubling or for difference frequency mixing (DFM). In order to achieve laser radiation in the mid-infrared (IR) spectral region, use is made of the frequency extension unit when light from the visible/near-IR is mixed. The fundamental from the pumping Nd:YAG laser at 1064 nm and the fundamental from the dye laser (the wavelength depends upon the dye involved and can also be tuned) is mixed in a LiNbO<sub>3</sub> crystal. The resulting IR-radiation appears between 1.4  $\mu\text{m}$  and 5.2  $\mu\text{m}$  [17], see Fig. 2.3. This is the total range, three different crystals being needed to cover it, due to the cut angle of the crystal. Within this wavelength region several important, combustion-related species can be probed, such as CO<sub>2</sub>, H<sub>2</sub>O, CH<sub>4</sub> and C<sub>2</sub>H<sub>2</sub>. The typical pulse energy and linewidth at 3  $\mu\text{m}$  are 2-3 mJ and 0.025 cm<sup>-1</sup>, respectively.

Since in many applications the energy from the DFM does not suffice, the original DFM part may need to be exchanged for a combined DFM and optical parametric amplifier (OPA) unit. Although the linewidth is not affected by this

upgrade, the energy is increased by approximately a factor of two. The wavelength range is slightly reduced, however, the laser only covering the range of 1.4 – 4.2  $\mu\text{m}$  [18], due to the cut angle of the crystals. This system, with its OPA is made use of in Papers X and XII, whereas a system without an OPA is utilized in Papers VIII, IX and IX, various of the findings are discussed in Chapter 4.

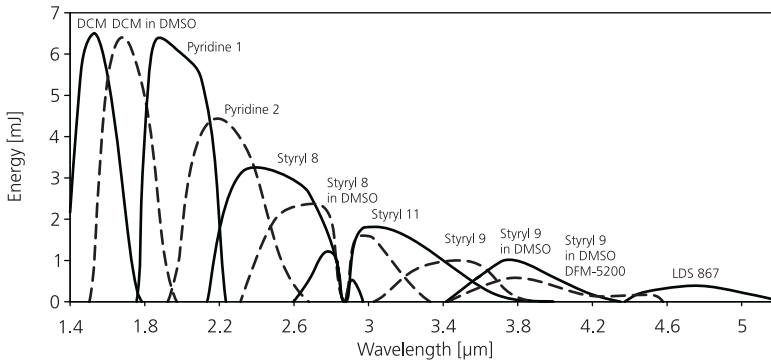


*Figure 2.3 Output energy from the mixing unit as a function of wavelength and dye [17]. In the case of an amplifying OPA the energy increases roughly by a factor of two [18].*

## 2.4 The Alexandrite laser

Alexandrite, which is chromium-doped chrysoberyl, is a crystal of  $\text{BeAl}_2\text{O}_2$  in which  $\text{Cr}^{3+}$  ions replace some of the  $\text{Al}^{3+}$  ions. The energy state of the  $\text{Cr}^{3+}$  ion is similar to that of other hosts having an octahedral, crystal structure, such as the ruby laser. The alexandrite laser is tunable, however, whereas the ruby laser is not. To explain this, a schematic energy level diagram for the alexandrite laser showing the energy states involved as a function of the distance between the  $\text{Cr}^{3+}$  ion and the  $\text{O}^{2-}$  anions in the octahedral structure of the alexandrite crystal is presented in Fig. 2.4. As can be seen, the  ${}^4T_2$  and  ${}^2T_1$  states (where the superscript to the left of the letter denotes the multiplicity of the state and the letter itself the particular rotational symmetry of it) are shifted in comparison with the  ${}^4A_2$  and  ${}^2E$  states. The decay from the  ${}^4T_2$  to the  ${}^2E$  state occurs very rapidly through internal conversion (the decay time is less than 1 ps), probably on the basis of a level crossing between the two states. The two levels can be considered to be in thermal equilibrium at all times. Since the energy difference between the two lowest vibrational levels in each state is very small ( $\Delta E = 800 \text{ cm}^{-1}$ ) a large population is found at the lower vibrational levels in  ${}^4T_2$  when  ${}^2E$  is populated. Taking into account of the Franck-Condon principle (see Fig. 2.4), it can be seen that a large number of vibronic transitions between the  ${}^4T_2$  and the  ${}^4A_2$  state is favorable, yielding a broadband emission of 700-800nm.

The  ${}^2E$  state is a long-lived, meta-stable state since  ${}^2E \rightarrow {}^4A_2$  is spin-forbidden and can thus act as a reservoir for the  ${}^4T_2$  state, helping to maintain the population inversion [8]. In the ruby laser, the lasing occurs between the  ${}^2E$  and the  ${}^4A_2$  state, the ruby laser operating as a three-level system that de-excites to the ground vibrational level in the  ${}^4A_2$  state.

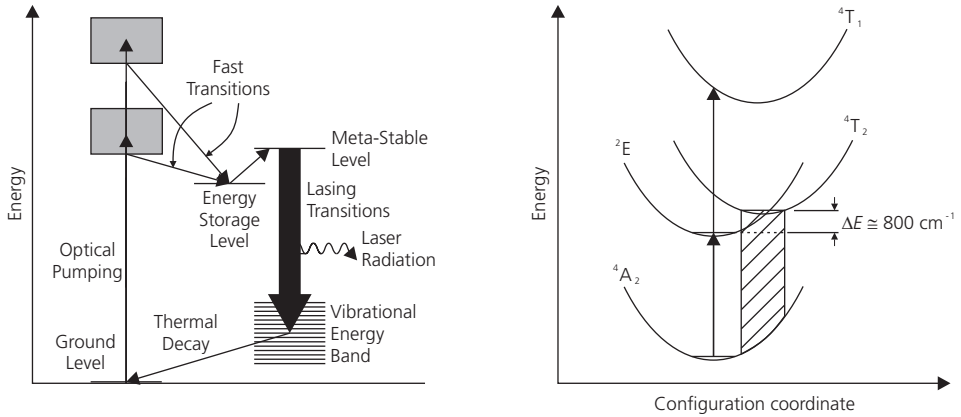


*Figure 2.4* A schematic energy level diagram of the alexandrite laser is shown at the left, whereas a diagram in which the energy level is shown as a function of the configuration coordinate, i.e. as the distance between the  $\text{Cr}^{3+}$  ions and the  $\text{O}^{2-}$  anions, is presented at the right. The tunability of the alexandrite arises from the many vibrational energy levels available on account of the Franck-Condon principle.

The alexandrite crystal was already used as a flashlamp-pumped laser medium in the 1970s. To date, application of alexandrite lasers within the combustion community has been very limited, the most common applications having been in the medical [19] and meteorological areas, it having been used in the latter area for temperature and differential absorption lidar measurements in particular [20-22].

The alexandrite laser used in the measurements that follow is an injection-seeded single-longitudinal-mode (SLM) pulsed ring-cavity laser (PAL/PRO™ 101 Light Age Inc.). It is characterized by its narrow linewidth, high peak power and broad tunability. It has ideal features as a laser medium, such as long fluorescence lifetime (long pulse duration), excellent energy storage and broad gain bandwidth. The broad gain bandwidth gives the alexandrite its tunability from  $\sim 720$  to  $790$  nm and the long pulse duration of  $\sim 80$ - $120$  ns, provides a narrow linewidth, typically in the order of  $50$ - $60$  MHz. These characteristics, together with its relatively small frequency chirp makes it an attractive alternative to Ti:sapphire lasers [23]. It runs at a  $10$  Hz repetition rate and has a peak power of  $150$ - $200$  mJ, depending upon the wavelength. Two different tunable, single-frequency, external-cavity diode (ELD) lasers (Newport 2020A and Toptica DL-100) are utilized as seed source in order to narrow the emission frequency and tune it continuously. For the Newport 2020A, use was made of three different laser modules to cover the

spectral range of 739-785 nm, whereas with the use of the present diode the Toptica covers a range of 750 – 770 nm.

Detailed specifications of the alexandrite laser can be found in ref. [23] and Paper I. There are various differences between the system used here and that used by P. Bakule and co-workers [23], e.g. the piezo-mounted glass plate for reducing the time jitter and the intra-cavity electro-optic modulators for reducing the linewidth used by Bakule et al. is not employed in the present system. The schematic layout of the laser system is shown in Fig. 2.5.

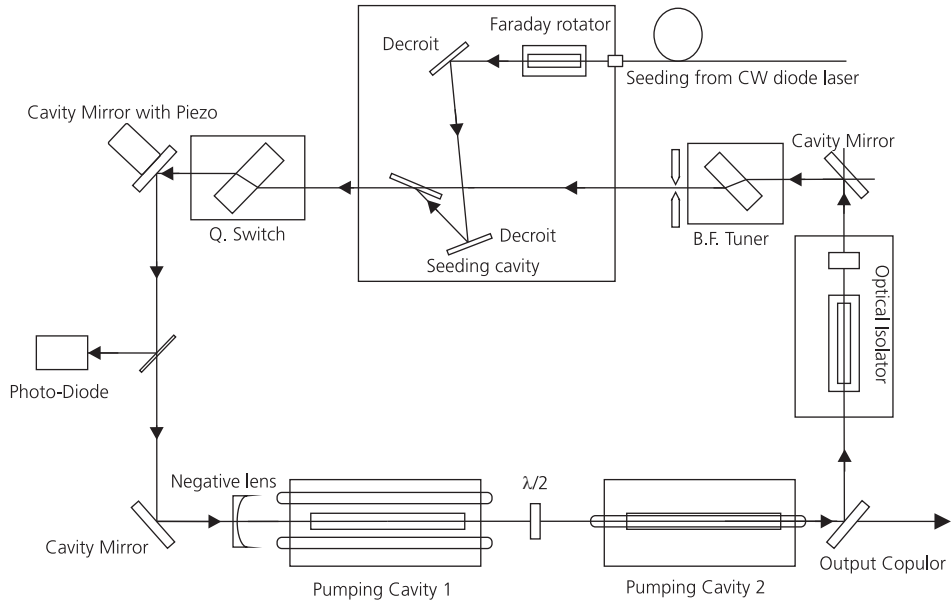


*Figure 2.5 Schematic layout of the PAL101, the B.F. tuner is used to select a particular part of the gain profile.*

The gain profile of the alexandrite crystal shifts with temperature and needs to be adjusted so as to favor the desired wavelength. The higher the temperature the more the gain profile maximum shifts towards longer wavelength. According to V. Wulfmeyer [21] the optimal temperature at 730 nm is 60 °C, whereas it is as high as 90 °C for 770 nm. For more detailed information on the alexandrite laser see ref. [24-27].

The most significant feature of the alexandrite laser is its broad tunability. Through different non-linear techniques, such as frequency doubling, tripling or quadrupling and stimulated Raman scattering (SRS) in H<sub>2</sub> and D<sub>2</sub>, a broad spectral range (from ~220 nm to 5 μm with certain gaps) can be achieved, see Table 2.2. The pulse energy at these wavelengths varies, of course, by orders of magnitude.

The original PAL101 system described above was upgraded with an amplifier, which is stand-alone and can boost the pulse energy by roughly a factor of two,

giving the original system a pulse energy of  $\sim 450$  mJ at 760 nm and up to  $\sim 50$  mJ at the third harmonic, at 254 nm (important for the filtered Rayleigh scattering measurements taken up in Chapter 3). The increased pulse energy and the long pulse duration make the system attractive for Raman measurements.

A unique feature of the PAL101 was utilized in Paper XIII and D, the seeding laser there being turned off, the only thing narrowing the linewidth then being the birefringent plate located in the cavity. This resulted in the linewidth becoming much broader,  $\sim 8$   $\text{cm}^{-1}$ , enabling several lines in the CH molecule to be covered at the same time. This is discussed further in Chapter 5.

*Table 2.2 Molecular or atomic species of interest for combustion diagnostics that have a frequency accessible with use of the SLM laser system. The nonlinear conversion schemes employed are shown, together with the estimated pulse energy and the linewidth (the pulse energies given are those obtained without an amplifier).*

Species	Wavelength	Conversion Scheme	Pulse Energy	Linewidth
NO, O	226 nm	SHG + S <sub>1</sub> (H <sub>2</sub> ) + SHG	5 mJ	400 MHz
CO	230 nm	SHG + S <sub>1</sub> (H <sub>2</sub> ) + SHG	5 mJ	400 $\pm$ 50 MHz
H <sub>2</sub> O	248 nm	THG	20 mJ	100 MHz
HCO	254 nm	THG	20 mJ	100 MHz
NH <sub>3</sub>	305 nm	THG + S <sub>2</sub> (H <sub>2</sub> )	2 mJ	-
OH	281 nm	THG + S <sub>1</sub> (H <sub>2</sub> )	5 mJ	300 MHz
C	287 nm	THG + S <sub>1</sub> (H <sub>2</sub> )	5 mJ	300 MHz
CN	388 nm	SHG	50 mJ	80 MHz
CH	431 nm	SHG + S <sub>1</sub> (D <sub>2</sub> )	5 mJ	-
CH	387 nm	SHG	50 mJ	100 MHz / 8 $\text{cm}^{-1}$
C <sub>2</sub>	563 nm	S <sub>1</sub> (H <sub>2</sub> ) + SHG	10 mJ	300 MHz
CO <sub>2</sub>	2 $\mu\text{m}$	S <sub>2</sub> (H <sub>2</sub> )	6 mJ	-
C <sub>2</sub> H <sub>2</sub> , CH <sub>4</sub>	3-3.5 $\mu\text{m}$	S <sub>2</sub> (D <sub>2</sub> ) + S <sub>1</sub> (H <sub>2</sub> )	0.5 mJ	-
CO, NO	4-5 $\mu\text{m}$	S <sub>2</sub> (H <sub>2</sub> ) + S <sub>1</sub> (D <sub>2</sub> )	0.5 mJ	-

<sup>a</sup> SHG: Frequency doubling; S<sub>1</sub>: 1<sup>st</sup> Stokes; S<sub>2</sub>: 2<sup>nd</sup> Stokes; S<sub>3</sub>: 3<sup>rd</sup> Stokes; THG: Frequency tripling; AS<sub>1</sub>: 1<sup>st</sup> anti-Stokes.

## 2.5 Detectors

The importance of using the appropriate detector for a given measurement cannot be exaggerated. Today, many different detectors are available, both point and two-dimensional detectors. These differ both in their sensitivity and in the spectral regions in which measurements can be made. In this section, a brief account is given of the detectors used in the different applications involved in the thesis work. *Photosensitivity* and *quantum efficiency* (QE) are important parameters that apply to

photosensitive devices. The photosensitivity of a detector is the ratio of the radiant energy (W) incident on the detector to the resulting photocurrent (A) coming out from the detector, whereas the quantum efficiency of a detector is defined as the percentage of photons hitting the photoreactive surface that produces the signal (which is a photo-electronic effect occurring in a photomultiplier tube or in an electron-hole pair in a semiconductor detector). Usually, both the photosensitivity and quantum efficiency are measured as a function of wavelength.

### **2.5.1 Photodiode**

The photodiode is the most robust detector of all. There are several different materials a photodiode can be composed of, the material(s) involved determines the properties of the photodiode, such as its sensitivity and its wavelength range. The most common photodiodes are silicon-based. They generate very little noise and are sensitive in the region of 190 – 1100 nm. Photodiodes generally have a high quantum efficiency, although their sensitivity is not even close to that of photomultiplier tubes, for example. They are used mainly for monitoring fluctuations in the pulse energy of the laser or for determining the temporal profile of the laser pulse. In the present work it was used to monitor the single-mode operation of the alexandrite laser. The typical rise time for a photodiode is in the order of a few nanoseconds to several hundred nanoseconds, although new and much faster diodes with rise times as low as hundreds of picoseconds are available.

### **2.5.2 Photomultiplier tube, PMT**

The photomultiplier tube (PMT) is a very sensitive detector, one that can be used even for single photon detection. Although its QE is not as high as that of the photodiode, its sensitivity is much greater. This is due mainly to the gain build-up produced by the avalanche of electrons through the PMT, delivering a gain five orders of magnitude greater than that of a photodiode. The size of the collection area is also larger than for a photodiode. Different photocathode materials must be used, depending upon the spectral region of interest. The spectral region is generally narrower than for a photodiode. A typical spectral response is shown in Fig. 2.6. Its rise time is very fast from  $\sim 1$  ns. The much faster MCP-PMT is also available. It has a microchannel plate (MCP) in front of the PMT, the MCP being that which creates the electron avalanche that the PMT detects. This brings the rise time of the MCP-PMT down to  $\sim 120$  ps. For a further account of the PMT, the reader is referred to ref. [28,29].

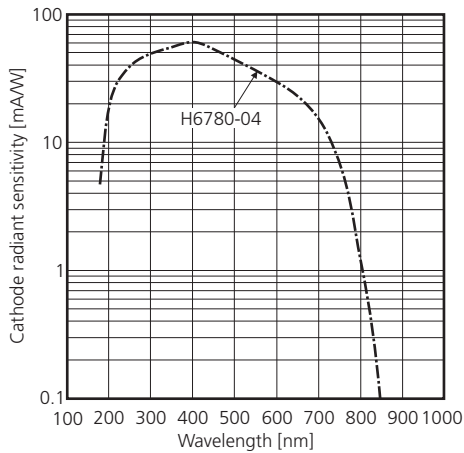


*Figure 2.6 The spectral response of a typical PMT, in this case a H6780-04 PMT from Hamamatsu.*

### 2.5.3 ICCD camera

An intensified charge-coupled device (ICCD) camera is based on a CCD detector coupled with an image intensifier placed in front of it. There are three advantages in particular the ICCD camera has compared with an ordinary CCD. These are:

- That the sensitivity is markedly increased allowing single photons to be measured.
- That the sensitivity can be extended down to the UV (180 nm) region.
- That the gating times are extremely short (in the order of nanoseconds).

All three points are extremely important in combustion diagnostics, where a short gate time is essential, due to the strong background luminescence. In an ICCD the intensifier (which consists of three parts: a photocathode, an MCP and a phosphorous material) is coupled with the CCD by optical fibres. The photons are detected and transferred to electrons in the photocathode and amplified in the MCP. The cascade of electrons the MCP creates for each photoelectron then reacts with the phosphorous material (each electron gives rise to ~200 photons in the phosphor). The photons from the phosphorous material are transferred by the optical fibres to the CCD, where they are detected. Each pixel of the CCD array is in a sense a separate detector in which the charge of the pixel is read out. The colour information is lost in the detection process.

*Table 2.3 Specifications of the ICCD camera systems used in the thesis work, [30-32].*

Parameter	ICCD 576S/RB-T, Princeton Instruments	ICCD MAX, Princeton Instruments	Flamestar II F, LaVision GmbH
Pixels	576 x 384	512 x 512	576 x 384
Pixel size	23 $\mu\text{m}$ x 23 $\mu\text{m}$	19 $\mu\text{m}$ x 19 $\mu\text{m}$	23 $\mu\text{m}$ x 23 $\mu\text{m}$
Chip size	13.2 mm x 8.8 mm	9.7 mm x 9.7 mm	13.2 mm x 8.8 mm
QE	$\geq 13$ % at 250 nm	See Fig. 2.7	See Fig. 2.7
Dynamic range	14 bit	16 bit	14 bit
Readout speed	$\sim 0.5$ frames/s	2-3 frames/s	2.5 frames/s

Three different ICCD camera systems were used for the measurements made in the thesis work. An ICCD 576S/RB-T from Princeton Instruments Inc. was used for the atomic hydrogen measurements reported in Paper VI. The LaVision, Flamestar II F was used in the studies reported in Papers I ,IV and XIII and an ICCD MAX camera from Princeton Instruments Inc. was used in the studies reported in Paper II and III. Certain selected specifications of the three camera systems are listed in Table 2.3 for comparison purposes, the QE of ICCD MAX and Flamestar II F as a function of wavelength can be found in Fig. 2.7.

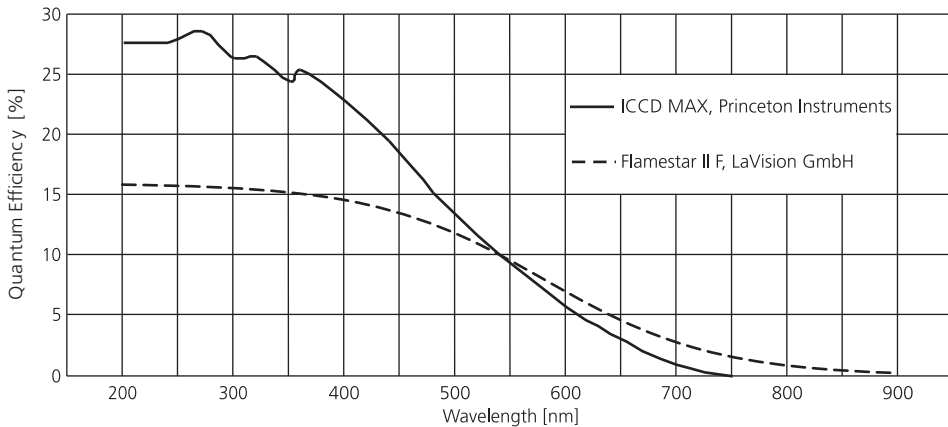


*Figure 2.7 The quantum efficiency of IMAX [31] and of Flamestar II F, measurements of the quantum efficiency of the latter was reported on in ref. [32].*

#### 2.5.4 Infrared detectors

In earlier parts of this section different detectors in the UV and visible spectral range were discussed, yet there are several species important in combustion that

possess no accessible transitions within the spectral range. The infrared regime is becoming increasingly important in efforts to overcome this problem. Both point detectors and imaging detectors that are generally liquid nitrogen cooled and working at 77 K are readily available. The detectors used in the thesis work are described below.

The point detector employed is an InSb detector, Judson Technologies J10D-M204-R04M-60, sensitive between 1.0 and 5.3  $\mu\text{m}$  (the spectral response is shown in Fig. 2.8). It is liquid-nitrogen cooled and has an active size of 4 mm [33].

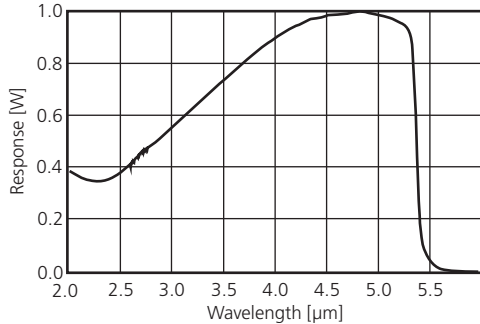


*Figure 2.8 Spectral response of the InSb-detector, J10D-M204-R04M-60 [33].*

The imaging detector is a Santa Barbara Focalplane SBF-134. This is an InSb detector with a maximum framerate of  $\sim 230$  frames/s and a  $256 \times 256$  array size, the pixels being  $30 \times 30 \mu\text{m}$  [34]. It is a sensitive detector specified as being able to measure temperature differences smaller than 20 mK. Its QE ranges between 85 and 95 % in the 1.0 – 5.3  $\mu\text{m}$  region [35]. The SBF-134 pixel response needs to be calibrated to a homogeneous back body emitter whenever a change in the integration time occurs. A typical planar laser-induced fluorescence (PLIF) image acquired by the SBF-134 camera is shown in Fig. 2.9.

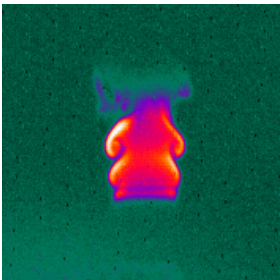


*Figure 2.9 An IR-PLIF image of a  $\text{CO}_2$  gas jet in open air at 4.27  $\mu\text{m}$ , acquired by the SBF-134 camera.*

## 2.6 Optical components

In terms of the spectral region involved, the measurements reported in the thesis range from UV to the mid-IR. Accordingly, a variety of different optical materials

are needed. A very brief account of the optical materials and of certain special optical components is provided in this section.

### 2.6.1 From UV to IR. What materials to choose.

The choice of optical material for measurements within in the visible spectral range is obvious. Glass, or BK7 which is the more correct term, has a good transmission within the visible range and out to the near-IR (350 – 2000 nm) range, as well as its being cheap. Still other materials are needed too, both at shorter and longer wavelengths. For shorter wavelengths (180 – 2000 nm), UV-grade fused silica (FS) is what is most commonly used. Since FS has a higher damage threshold than BK7, it may also be preferable within the visible spectral range if the laser fluence is very high. There are other alternatives to FS as well but the low price and high availability makes FS the most attractive choice within the UV spectral range.

Within the near- and the mid-IR spectral region, there are other materials that are more attractive, although FS has a narrow window of transmission around 3  $\mu\text{m}$ . Here  $\text{MgF}_2$  and  $\text{CaF}_2$  is the dominant optical materials.  $\text{MgF}_2$  (130 – 8000 nm) is very rugged, its being a hard crystal that is resistant to mechanical and thermal shock. It also handles high laser energies well and its performance in the VUV is appreciated by excimer laser users, for example.  $\text{CaF}_2$  (150 – 8000 nm) is more commonly used for IR measurements. The  $\text{CaF}_2$  has a slightly better transmission at longer wavelengths. It is not as hard and resistant as  $\text{MgF}_2$  but has become the most important material for use in the mid-IR spectral range. The transmission profiles of the abovementioned materials are shown in Fig. 2.10.

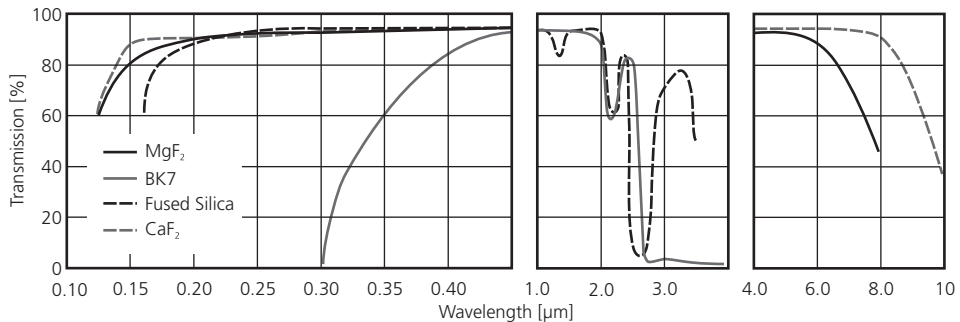


**Figure 2.10** Transmission profiles of the optical materials most commonly used for UV to mid-IR spectroscopy [36].

There are still other materials, such as calcite ( $\text{CaCO}_3$ ),  $\alpha$ -BBO and  $\text{YVO}_4$ , used for polarizers and certain other optical components. These are all commonly employed in Glan Taylor, Glan Thompson and Glan laser polarizers. As can be seen in Fig. 2.11, the  $\text{YVO}_4$  polarizer can be recommended for measurements within the IR-region whereas calcite is optimal for use within the UV-spectral

region. Calcite is soft and easy to scratch and has a lower damage threshold than  $\alpha$ -BBO. Both  $\alpha$ -BBO and  $\text{YVO}_4$  have a very large birefringent coefficient, making them ideal polarizer materials. The transmission profiles of the most common polarizer crystals are shown in Fig. 2.11. There are several other optical materials, but these will not be dealt with here.

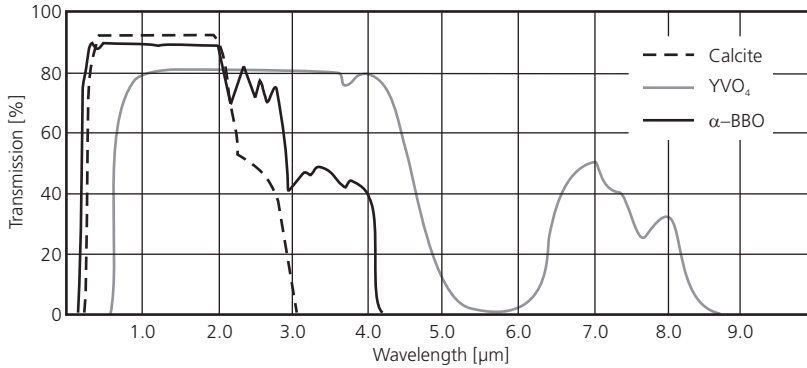


*Figure 2.11 Transmission profiles of four different polarizer materials [37].*

## 2.6.2 Polarizers

A large part of the thesis work is concerned primarily with polarization spectroscopy (PS). A well matched polarizer pair is needed in order for precise PS measurements to be performed. This means the extinction ratio of the two crossed polarizers being good (typically in the order of  $10^{-6}$  or better). The polarizers used in these measurements are Glan-laser, Glan-Taylor and Glan-Thomson polarizers. Two prisms are cemented together in the Glan-Thomson polarizer, resulting in its not being able to withstand a high laser fluence, although high extinction ratios are obtainable. It has a wider acceptance angle than the Glan-laser and the Glan-Taylor polarizers do.

The Glan-laser and the Glan-Taylor polarizers are very similar. Both of them have an air space between the two prisms, enabling them to be manufactured for the IR-spectral range. The escape window which the Glan-laser has is the only major difference between them. Glan-laser polarizers can thus withstand the highest laser fluence and are often the best choice for PS measurements.

## 2.7 Burners

New diagnostic techniques for combustion that are being developed need to be tested and calibrated on relatively small and well-known laboratory flames. When such techniques are well calibrated, they are utilized to gain information on new

laboratory flames and are often compared with computational fluid dynamics (CFD) simulations. The major types of burners used in the thesis work will now be described.

### 2.7.1 Co-axial jet flame burner

Turbulence is very important in combustion. It increases the flame velocity making it possible for leaner mixtures to be burned, this serving to effectively reduce pollutants. Use of a lean mixture reduces  $\text{NO}_x$ , CO and soot emissions, the  $\text{CO}_2$  emissions also being reduced, since less fuel is consumed. Considerations of this sort have led to increasing attention being directed at the study of turbulent, premixed, lean combustion. A co-axial jet flame burner has been studied in Paper XIII and Paper D. The results of this investigation are still being compared with LES modelling. The burner consists of two metal tubes, the inner one having a diameter of 2.2 mm and the outer one a diameter of 22 mm, see Fig. 2.12. The two tubes can be fed independently of each other with differing gas mixtures, making it possible to use the large outer tube for a pilot-flame, one burning a slightly rich mixture, and the inner one to provide either a fuel/air gas mixture or pure fuel or air. The flow in the inner tube can reach flow speeds of more than 120 m/s, which produces a highly turbulent flame with a low global equivalence ratio. In ref. [38] and [39], Lee and Mitrovic have described a burner very similar to that employed here. The gas flow to the present burner, which is regulated by mass-flowmeters (Bronkhorst El-Flow), can be precisely controlled.

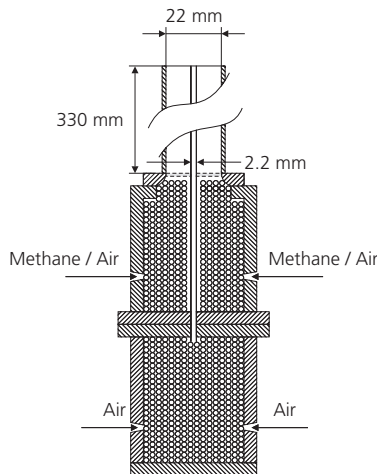


*Figure 2.12 Schematic of the co-axial jet flame burner.*

### 2.7.2 Low-swirl burner

As indicated in Section 2.7.1, the development of lean premixed combustion has become an important option for reducing  $\text{NO}_x$  emissions, especially from natural gas heating and from power systems. The low-swirl conception, initiated by R. K. Cheng and co-workers [40,41], holds the potential for enabling ultralow  $\text{NO}_x$  emission levels ( $< 5 \text{ ppm NO}_x$  (15%  $\text{O}_2$ )) to be achieved in stationary gas turbines [42]. Up till now, no standard for low-swirl flames has been employed. A new low-swirl burner, designed by R. K. Cheng and co-workers and employed in Paper III, appears to possibly be one that can serve as a standard for the low-swirl flames it provides. This burner, which has been manufactured in three identical examples, is found at three different locations in the world: Lund, Darmstadt and Berkley. Its major characteristic is that of providing a detached flame that propagates freely in a diverging, intensely turbulent flow field. This allows very lean flames to be stabilized, without recirculation so as to anchor the flame needing to be relied on. Even under conditions of very intense turbulence, it stabilizes lean premixed flames at a level very close to the flammability limit [41]. The burner design includes an annular swirler consisting of eight curved vanes used in conjunction with a perforated plate fitted to the entrance of the centre channel, see Fig. 2.13. Fixed vanes rather than air jets are employed here, due to the need of the flames in the three different burners being reproducible. The inner nozzle has a diameter of 50 mm, whereas the outer co-flow is 600 mm in diameter. The flame typically burns a methane/air or a natural gas/air mixture, and the co-flow being fed by air. A cross-section of the burner is shown in Fig. 2.13.



*Figure 2.13 A cross-section of the low-swirl burner is shown at the left. A photograph of the burner and the co-flow surrounding it is shown at the upper right and a photograph of the inside of the burner nozzle is shown at the lower right, the vanes and the perforated plate being visible.*

### 2.7.3 Wolfhard-Parker burner

The Wolfhard-Parker burner (WP-burner) was introduced by Wolfhard and Parker in 1949 [43] and has since been used in a number of experiments. It is used most frequently for studying diffusion flames. The flame, due to its one-dimensional and stable appearance, is attractive for use in very thorough studies. Smyth et al. [44] provide an excellent account of its construction and of the setup. The fuel flows through an 8 mm x 41 mm centre slot and the air through two 16 mm x 41 mm slots on each side of the fuel slot, creating two flame fronts. In order to obtain uniform conditions, the burner chambers are filled with 1 mm diameter glass beads and are covered with a copper screening 3–4 mm below the burner surface. A rectangular mesh-chimney is used to stabilize the flame. Smyth et al. [44] conducted a thorough investigation of the major species concentrations, flows and temperatures in the flame, these data and an exact copy of the burner are being utilized in Paper II. The temperature data of Smyth et al. was later confirmed by Vestin et al. in 2007, using rotational coherent anti-Stokes Raman scattering (CARS) [45]. The burner was also employed by Beyrau et al. in investigations of partially premixed methane/air flames [46], mainly by use of CARS. The burner was utilized in the same way in Paper XIII.

### 2.7.4 The porous plug burner

As already indicated, the calibration of new spectroscopic and diagnostic techniques is highly important to their development. This requires use of well characterized and geometrically simple flames. Premixed flat flames fulfil both these criteria. The one-dimensional structure of a premixed flat flame, in which the only change in parameters is in the height above the burner, creates a stable and reproducible flame. A premixed flat flame is achieved by using a porous plug burner, often referred to as a McKenna burner due to its main manufacturer, the firm McKenna Products. Fig. 2.14 shows a schematic image of the construction of a porous plug burner. The fuel/air mixture enters at the bottom and is pressed through a sintered metal plug in the centre of the burner. A second plug is placed concentrically around the centre plug as a co-flow. The co-flow is used to stabilize the flame and also to shield it from oxygen entrainment from the surrounding air. The centre plug is 60 mm in diameter. A steel cylinder, 21 mm in diameter, is placed above the burner in order to stabilize the flame, a laminar, one-dimensional flame being obtained in this way.

A second premixed flat flame burner, located inside a low-pressure chamber, was used in the studies reported in Papers V, X and XII. It lacks a co-flow and it is only 30 mm in diameter. A more detailed account of this burner is provided by Walewski et al. [47]. Both burners are water-cooled in order not to damage the sintered plug.

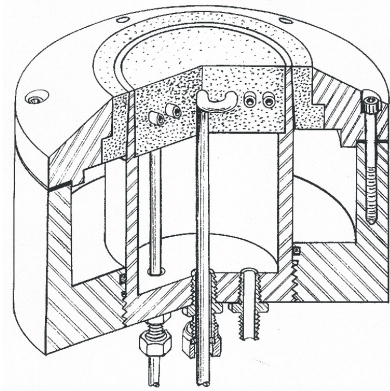


*Figure 2.14 A schematic of the construction of the McKenna burner which is described.*

# Chapter 3

## Filtered Rayleigh scattering (FRS)

There are several important quantities to be measured in combustion. Velocity, species concentration and temperature are three of these. Temperature, one of the most crucial parameters, needs to be determined with particular accuracy. The use of two-dimensional (2D) measurements both in laboratory environments and real-life applications is increasing. In the present chapter the development and application of filtered Rayleigh scattering (FRS) as a tool for 2D-temperature measurements is discussed.

### 3.1 Basic features of filtered Rayleigh scattering (FRS)

Various techniques for temperature measurements have been developed over the years. These include two-line atomic laser-induced fluorescence (TLAF), laser-induced fluorescence (LIF), Raman scattering, CARS, and laser Rayleigh scattering (LRS). Each technique has its own special problems. TLAF needs a seeded fluorescent species (such as indium [48]). LIF suffers from absorption and fluorescence trapping, as well as saturation and quenching; Raman scattering is species-specific but suffers from low signal levels. CARS is very accurate but is limited to point detection. LRS is one of the techniques able to provide 2D-thermometry, having a high degree of accuracy [49] (6% for single shot and 4% for averaged measurements at 300 – 2000 K). Due to its elastic nature, LRS is subject to strong interference from stray light, however, the marked elastic scattering produced by aerosols, optics, burners, and the like can completely bury the Rayleigh signal. An approach to dealing with the stray-light issue was introduced by Miles et al. in 1990 [50]. It was followed up and demonstrated in 1992 [51] by the same group and was given the name filtered Rayleigh scattering (FRS). Through utilizing a narrow-linewidth laser at 532 nm and a molecular iodine filter, the group was able to filter out the spurious scattering and achieve flow field measurements at Mach 3 and 5, utilizing the fact that the irradiated light is Doppler shifted by the high speed flow of the molecules in the sample. Placing a narrow-linewidth laser at the centre of the absorption notch filter allows the un-broadened spurious scattering to be filtered away, the Doppler broadened wings, from molecular thermal motion, of the scattering profile being transmitted

through. Since 1992 a number of groups have developed FRS further and applied it in combustion and flow diagnostics. Hoffman et al. made the first thermometry measurements in sooting flames in 1996 [52,53], and work in supersonic flows was continued by Elliott and co-workers [54-57]. In 2001 both Most et al. and Elliott et al. employed FRS for measuring temperature, simultaneous with the use of particle-induced velocimetry (PIV) for flow field measurements [58,59]. Parallel to this, the Princeton group developed a UV, narrow-linewidth, high-power laser system that was paired with an atomic mercury filter [60,61]. This was a logical choice, since the Rayleigh scattering cross-section scales as  $\nu^4$ . As a filter, mercury is superior to molecular iodine, due to its higher extinction ratio. Accordingly the thesis work has been concentrated on the development of UV-FRS at the strong mercury absorption line at around 254 nm, where the single-longitudinal-mode alexandrite laser described in Section 2.4 was paired together with an isotopically enhanced  $^{202}\text{Hg}$  cell.

### 3.2 The mercury absorption filter

The strong  $6s6p\ ^3P_1 - 6s^2\ ^1S_0$  transition (oscillator strength  $f = 0.0024$  [62]) of mercury is suitable as a narrow-band absorption filter. Mercury has seven naturally occurring isotopes, each with a slightly different transition energy. The isotopes are listed in Table 3.1 together with the relative energy shift of each with respect to  $^{202}\text{Hg}$ .

*Table 3.1 The frequency difference in GHz relative to  $^{202}\text{Hg}$ . [63,64]. The species  $^{197}\text{Hg}$  and  $^{197}\text{Hg}^*$ , non-abundant under natural conditions, are omitted.*

Isotope	$\Delta\nu$ [GHz], Proffitt et al.	$\Delta\nu$ [GHz], as observed by Bitter
196	14.579	14.213
198	10.384	10.106
199	16.909	16.834
199	-4.997	-5.303
200	5.125	5.301
201	16.909	16.978
201	9.452	9.43
201	-4.531	-4.556
202	0	0
204	-4.997	-5.207

#### 3.2.1 Mercury as a filter candidate

The most important characteristics of an ideal notch filter are 1) a high transmission rate outside the absorption band, 2) a sharp cut-off slope, 3) a high

rejection ratio (or low transmission) inside the absorption band, and 4) the width of the absorption profile needing to be narrow and in some experiments to be variable. The transmission through an atomic or molecular filter is strongly dependent upon the temperature – the higher the temperature, the higher the rejection ratio and the broader the line is, i.e. the broader the absorption notch. As can be seen in Table 3.1 the frequency differences between the peaks are very small. If the cell were kept at high temperature or pressure, these lines would blend together and become one broad and featureless line, due to broadening mechanisms such as pressure broadening and Doppler broadening. To avoid this and be able to control the linewidth and the extinction ratio, the cell is kept at low pressure ( $10^{-3}$  mtorr). To control the number density of mercury in the cell the temperature of the cell can be adjusted. In Fig. 3.1 the relationship between number density and temperature is shown.

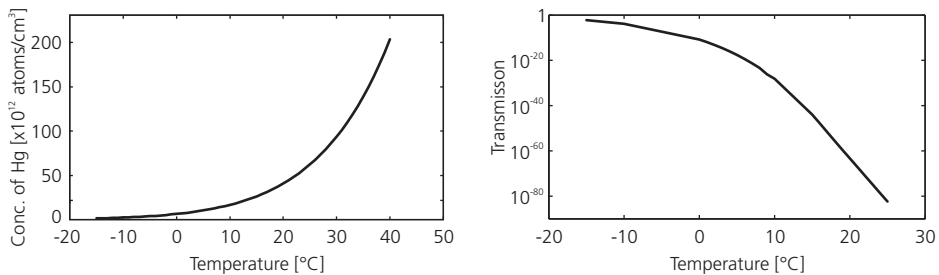


**Figure 3.1** The number density of Hg in the cell as a function of temperature is shown at the left [65], and transmission through the cell as a function of temperature at the right. The transmission is calculated for a 7 cm path of Hg assuming an unlimited amount of Hg and a 100 MHz Gaussian laser lineshape.

Mercury possesses the features mentioned earlier as being important, making it a perfect candidate for an optical filter. As an atomic species, its spectrum is easier to interpret and model than a molecular spectrum is, the rejection ratio at the line centre being much greater for atomic species, due to the stronger line intensity they possess. As mentioned above, the temperature and pressure control the rejection ratio. The transmission through the mercury cell (calculated using Beer-Lamberts law) as a function of temperature is shown in Fig. 3.1 (note that the calculations are theoretical).

### 3.2.2 Characterization of the mercury absorption filter

Characterization of the transmission profile of the notch filter is crucial in FRS measurements. Scanning the laser over the frequency range of interest, sending it through the mercury filter, and recording the light transmitted allowed an absorption profile, shown in Fig. 3.2 (gray dots), to be obtained. A theoretical absorption profile, in which Doppler broadening, pressure broadening and the

laser linewidth were included, was fitted to the experimental data, using the number density as the fitting parameter. The discrepancy between the theoretical results (dashed line) and the experimental data is shown in Fig. 3.2. In earlier work on FRS, “wings” of the same sort were observed [62]. According to Finkelstein [62], the broadening is non-physical and may be the result of a second spatial mode in the laser. Through introducing an extra Lorentzian contribution ( $\sim 50\text{-}60$  MHz) in the model, much better fit to the experimental data can be obtained, as shown in Fig. 3.2 (solid black line).

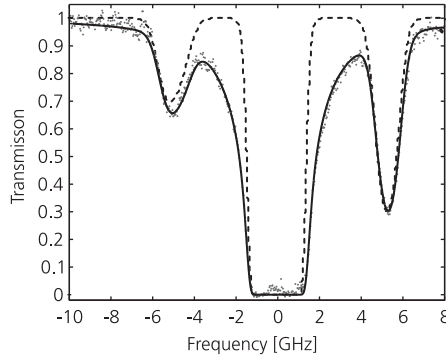


*Figure 3.2 Absorption spectrum for Hg, the dotted line being the experimental results, the dashed line being the spectrum without the Lorentzian contribution and the solid black line the spectrum with the Lorentzian contribution, as modelled at  $20^{\circ}\text{C}$ .*

### 3.2.3 Experimental setup and measurements

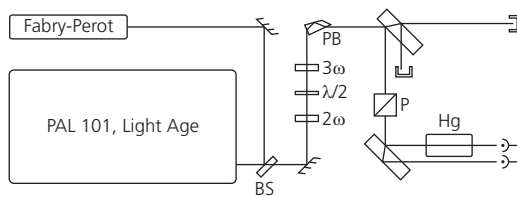


*Figure 3.3 Schematic setup for characterization of the mercury filter; PB, Pellin Broca; P, polarizer; Hg, mercury cell.*

The alexandrite laser described in Section 2.4 was frequency-tripled to achieve the desired wavelength ( $253.6528$  nm). A schematic layout of the experimental setup is shown in Fig. 3.3.

A Pellin-Broca prism was used to disperse and separate the three different wavelengths contained in the tripled beam. Less than a 4 % reflection from a thick fused silica window was picked up after the

Pellin-Broca and was sent through two polarizers and then bounced off a second, thick fused-silica window, the front and back reflection being sent to a pair of identical photodiodes, the front reflection going through the mercury cell. In this way, two signals were detected, one to monitor fluctuations in the laser pulse

energy and the other to monitor the transmission profile of the filter. The laser was then scanned over  $\sim 20$  GHz, the transient signals from the photodiodes being collected, time-integrated and stored in a 3 GHz bandwidth digital oscilloscope (Lecroy, Wavemaster 8300). A small portion of the fundamental was sent simultaneously to a 300 MHz free-spectral range, confocal Fabry-Perot etalon (Coherent). In this way, a relative frequency scale was obtained and corrections for non-linearity in the wavelength scan of the laser could be made, described in further detail in Paper I. As mentioned earlier, the transmission profile of the filter is strongly dependent on temperature, as shown in by Fig. 3.4.

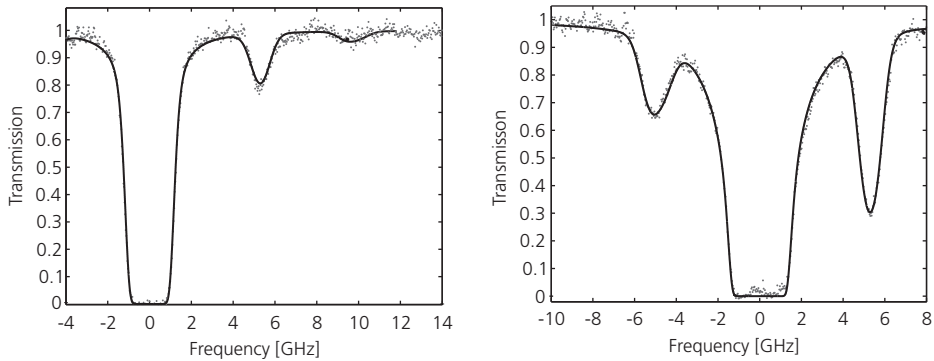


*Figure 3.4 The absorption profile of Hg-cell measured and modelled at  $0^{\circ}\text{C}$  is shown at the left; at 30 % transmission the absorption notch is  $\sim 2,3$  GHz in width. The absorption profile of an Hg-cell measured and modelled at  $20^{\circ}\text{C}$ , is shown at the right; at 30 % transmission the absorption notch is  $\sim 3,2$  GHz in width.*

### 3.3 Rayleigh - Brillouin scattering

The conventions applied in Rayleigh scattered light terminology (i.e. when the size of the particles involved is much smaller than the irradiated wavelength), differ. Under the most general circumstances, when light is scattered the spectrum contains both vibrational Raman scattering and Rayleigh scattering. Consensus in the terminology employed appears to end here, yet according to Young and She (ref. [66] and ref. [67], respectively) the Rayleigh scattering consists of rotational Raman lines (often referred to as Rayleigh-wing scattering) and the central, Doppler-broadened Cabannes line. The Cabannes line is composed of the Brillouin doublet and the unshifted, central Gross or Landau-Placzek line (often called the Rayleigh line, the rotational Raman Q-branch also being included, its representing  $\sim 1\%$  of the signal), shown schematically in Fig. 3.5. Throughout thesis the terminology found in Boyd [68] will be followed, however.

With use of standard lasers and of unfiltered light collection, the Rayleigh signal is the sum of all the abovementioned components, vibrational Raman being the weakest feature of all components (representing typically 0.1% of the signal [69]) so that its contribution can usually be neglected. The largest part of the Rayleigh scattering is polarized, the position of the laser in relation to the detector having a significant impact on the amount of it which is collected.

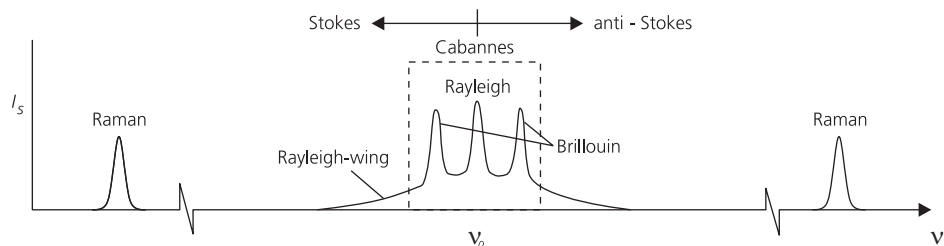


*Figure 3.5* A schematic spectrum of the total scattered light in a gaseous media. The dashed part is termed the Cabannes line.

Rayleigh scattering is usually referred to as an “elastic” process, meaning that it does not exchange energy with the molecule, the scattered light thus having the same frequency as the incident light, which is true for the central part of the scattering. Since no change in the internal energy of the molecule occurs, Rayleigh scattering is not species-specific in a spectral sense. It comes about through non-propagating fluctuations in density.

At high pressure and low temperature the Brillouin scattering becomes noticeable and needs to be taken into account. Brillouin scattering is the scattering of light by sound waves, i.e. propagating pressure (or density) waves.

A brief account of the different conditions that can apply and their impact on the Rayleigh-Brillouin lineshape and the Rayleigh cross-section follows.

### 3.3.1 Rayleigh scattering cross-section

If the molecules are spherical, as in the case of a monoatomic noble gas, there is a lack of rotational Raman scattering. The Rayleigh cross-section can then be derived using the classical model for the radiation from an infinitesimally small oscillating dipole. The differential Rayleigh cross-section can be expressed then as

$$\frac{d\sigma}{d\Omega} = 4\pi^2 \cdot \frac{\nu^4}{c^4} \cdot \frac{|n-1|^2}{N^2} \cdot \sin^2 \phi \quad (3.1)$$

where  $\nu$  is the light frequency,  $n$  the index of refraction,  $c$  the velocity of light,  $N$  the number density and  $\phi$  the angle between the observation direction and the polarization direction of the incident light. A more rigorous derivation taking into account the rotations of diatomic molecules and orientation averaging can be

found in ref. [69] or [70]. The well-known  $\nu^4$  dependence can be noted in equation (3.1). This makes it attractive to perform Rayleigh scattering measurements in the UV-spectral range. It is also clear that the cross-section is dependent upon the index of refraction, which can be used to derive the Rayleigh cross-section from earlier refraction measurements.

*Table 3.2 The refractive indices and differential Rayleigh scattering cross-sections of different combustion-related species at 254 nm, the differential cross-section being calculated from equation (3.1) at standard temperature and pressure, STP.*

Species	Index of refraction $(m_i - 1) \times 10^3$	Rayleigh differential cross-section $d\sigma_{R,i}/d\Omega \times 10^{27} [\text{cm}^2]$	Rayleigh scattering cross-section relative to air
H	0.077 <sup>a</sup>	0.88	0.06
O	0.151 <sup>a</sup>	3.34	0.23
N	0.161 <sup>a</sup>	3.79	0.26
C	0.188 <sup>a</sup>	5.20	0.35
H <sub>2</sub>	0.154 <sup>b</sup>	3.49	0.24
OH	0.228 <sup>d</sup>	7.64	0.52
CO	0.378 <sup>b</sup>	20.95	1.42
N <sub>2</sub> O	0.564 <sup>c</sup>	46.82	3.16
NH <sub>3</sub>	0.461 <sup>c</sup>	31.23	2.11
NO	0.331 <sup>c</sup>	16.06	1.09
O <sub>2</sub>	0.302 <sup>b</sup>	13.42	0.91
H <sub>2</sub> O	0.305 <sup>d</sup>	13.70	0.93
CO <sub>2</sub>	0.490 <sup>e</sup>	35.21	2.38
N <sub>2</sub>	0.321 <sup>f</sup>	15.15	1.02
Air	0.317 <sup>g</sup>	14.80	1.00
CH <sub>4</sub>	0.490 <sup>b</sup>	35.32	2.39
C <sub>2</sub> H <sub>2</sub>	0.706 <sup>d</sup>	73.15	4.94
C <sub>2</sub> H <sub>4</sub>	0.860 <sup>c</sup>	108.7	7.35
C <sub>2</sub> H <sub>6</sub>	0.853 <sup>c</sup>	106.9	7.23
C <sub>3</sub> H <sub>6</sub>	1.263 <sup>c</sup>	234.4	15.84
C <sub>3</sub> H <sub>8</sub>	1.224 <sup>c</sup>	220.3	14.88
C <sub>7</sub> H <sub>16</sub>	2.305 <sup>h</sup>	781.1	55.79
C <sub>8</sub> H <sub>18</sub>	2.610 <sup>h</sup>	1001.4	67.68

<sup>a</sup> Computed from the decomposition of the atomic contributions from H<sub>2</sub>, O<sub>2</sub> and N<sub>2</sub>

<sup>b</sup> From Smith et al. [71]

<sup>c</sup> From Landolt-Börnstein for  $\lambda = 257.7$  nm [72]

<sup>d</sup> Computed from summation of the atomic contributions [73]

<sup>e</sup> From Bideau-Mehu et. al [74]

<sup>f</sup> From Griesmann et al. [75]

<sup>g</sup> From Bates [76]

<sup>h</sup> From Vogel for  $\lambda = 434$  nm [77]

In Table 3.2 the index of refraction and the differential Rayleigh cross-section for an observer located at  $90^\circ$  to the incident laser beam at 254 nm for a number of species important in combustion are listed. In the case of a multi-component mixture, the total differential Rayleigh scattering cross-section is the sum of the cross-sections of each of the individual species,  $d\sigma_{Ri}/d\Omega$ , multiplied by the mole fraction,  $x_i$ , of that species in the mixture, according to equation (3.2).

$$\frac{d\sigma_{Rtot}}{d\Omega} = \sum_i \frac{d\sigma_{Ri}}{d\Omega} \cdot x_i \quad (3.2)$$

### 3.3.2 Lineshapes of Rayleigh-Brillouin scattering

Since in FRS the lineshape is taken into account in deriving the temperature, it is important to take it into account in performing FRS measurements. There are three different regimes that can apply in calculating the FRS lineshape, depending upon the temperature and the pressure: the *Knudsen regime*, the *kinetic regime* and the *hydrodynamic regime*. The Knudsen regime and the hydrodynamic regime are the two extremes.

The simplest of cases is the Knudsen regime. At low pressure or high temperature, i.e. at low gas density, the only thing that affects the Rayleigh line is the thermal motion of the molecules. Each molecule can be seen as an individual scatterer and the mean-free-path is large, minimizing the importance of collisions between the molecules. This results in a purely Gaussian profile, one which follows the Maxwellian velocity distribution at the given temperature,  $T$ , due to Doppler broadening of the incident laser light. The expression for the line profile is given by

$$g(\theta, T, \nu) = \frac{2}{\Delta\nu_T} \sqrt{\frac{\ln 2}{\pi}} \exp\left[-4 \ln 2 \left(\frac{\nu - \nu_0}{\Delta\nu_T}\right)^2\right] \quad (3.3)$$

where

$$\Delta\nu_T = \frac{|\mathbf{k}|}{2\pi} \sqrt{\frac{8kT \ln 2}{m}} \quad |\mathbf{k}| = \frac{4\pi}{\lambda} \sin\left(\frac{\theta}{2}\right) \quad (3.4)$$

where  $m$  is the mass of the molecule and  $\theta$  is the detection angle. Note that  $g(\theta, T, \nu)$  integrated over  $\nu$  is normalized to 1 and  $\Delta\nu_T$ , the width, which is defined as the Full-Width-at-Half-Maximum (FWHM). The temperature can be deduced by measuring the spectral width of this profile. This approach can be employed at flame temperatures and at atmospheric pressure.

At the other extreme, the hydrodynamic regime, pressures are high, the Rayleigh scattering being due to density fluctuations [52]. This splits the original single line into three Lorentzian lines: one central line, that is unshifted, due to isobaric density fluctuations (temperature fluctuations), and two shifted sidebands, termed Brillouin lines, which are due to adiabatic density fluctuations (acoustic

waves). The total lineshape of the scattered light and the mechanisms behind it are discussed more thoroughly in ref. [52] and [68].

The most common region, as could be expected, is the one between the two extremes, termed the kinetic regime. This regime provides a challenge in modeling, several different approaches to it having been adopted, such as Yip et al. [78] and that of Tenti et al. [79]. The S6-model [79,80] that Tenti and co-workers presented is presently considered the most accurate model for diatomic molecules. As Young and Kattawar have pointed out, the S6-model is not exact [81]. It assumes a single-species gas and does not include the Q-branch Raman scattering, yet according to Forkey [70] these errors are negligible in comparison to other sources of uncertainty.

In order to be able to quantify the relative importance of the random and of the correlated motions of the molecules, the S6-model introduces a quantity termed the  $y$ -parameter, defined by Tenti et al. [79] as

$$y = \frac{NkT}{\sqrt{2}k v_0 \eta} \quad (3.5)$$

where  $N$  is the number density of the gas,  $k$  the Boltzmann coefficient,  $\eta$  the shear viscosity,  $k$  is given by equation (3.4) and  $v_0$ , the thermal velocity of the molecules, is given by

$$v_0 = \sqrt{\frac{kT}{m}} \quad (3.6)$$

where  $m$  is the mass of the molecule. If the ideal gas law is assumed and the Sutherland formula for viscosity is employed,

$$\eta = \eta_0 \left( \frac{T}{T_0} \right)^{\frac{3}{2}} \left( \frac{T_0 + S}{T + S} \right) \quad (3.7)$$

where  $\eta_0$  is  $1.716 \times 10^{-5}$  Nsm<sup>-2</sup>,  $T_0$  is 273 K and  $S$  is 111 K for air, then the  $y$ -parameter becomes

$$y = 0.230 \left[ \frac{T(K) + 111}{T^2(K)} \right] \left[ \frac{P(\text{atm}) \lambda(\text{nm})}{\sin \theta / 2} \right] \quad (3.8)$$

where  $P$  is the pressure in atmospheres and  $\lambda$  is the wavelength of the laser in nm. If  $y \gg 1$ , the scattering is in the hydrodynamic regime, whereas if  $y \ll 1$  the scattering is in the Knudsen regime and acoustic effects can be neglected. Throughout the thesis the S6-model, which includes all three regimes, is employed. Both the line profile for the S6-model and the Knudsen regime at ambient temperature and pressure and the dependence of the Rayleigh-Brillouin lineshape on pressure are shown in Fig. 3.6.

It is evident from equation (3.8) that for shorter wavelengths the impact of acoustic phenomena is less, where under ambient conditions, for example,  $\gamma = 0.38$  for 254 nm, whereas  $\gamma = 0.79$  for 532 nm. It is also clear that the higher the temperature, the smaller the  $\gamma$ -parameter becomes (at 2000 K,  $\gamma = 0.04$ ).

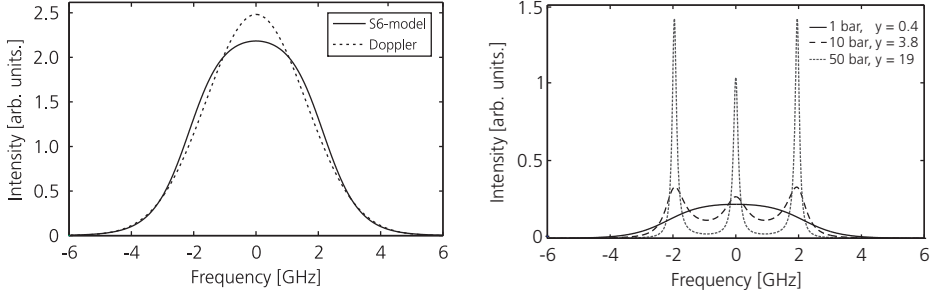


*Figure 3.6 The difference between a Doppler modelled profile and the S6-modelled profile modelled at 1 bar is shown at the left and the Rayleigh-Brillouin scattering profile at various pressures for 300 K is shown at the right.*

### 3.4 Filtered Rayleigh scattering theory

The total spectral intensity of Rayleigh-Brillouin scattered light is given by

$$I(\nu) = CI_0 N \Delta\Omega \sum_i x_i \frac{d\sigma_{Ri}}{d\Omega} r_i(T, P, m_i, \theta, \nu) \quad (3.9)$$

where  $C$  is the optical calibration constant,  $I_0$  the intensity of the incident laser,  $N$  the molecular number density and  $r_i$  the scattering distribution of the  $i$ :th gas species, as calculated by the S6-model and  $\Delta\Omega$  the collection solid angle. As indicated in Section 3.3.2, the S6-model only deals with single species. Accordingly, in the work presented in the thesis, nitrogen, being the major species, has been used to model the lineshape of the Rayleigh-Brillouin scattering. In situations in which light and small fuel molecules are involved this is adequate, but for more applied fuel a more rigorous model as well as lineshape measurements are needed. The FRS signal that is collected, which is an integration over the mercury transmission profile,  $t(\nu)$ , and the total spectral intensity,  $I(\nu)$ , can be expressed as

$$S(\nu_0) = \int_{-\infty}^{+\infty} I(\nu) t(\nu - \nu_0) d\nu \quad (3.10)$$

its being marked by the shaded area in Fig. 3.7. The mercury filter attenuates the central part of the Rayleigh-Brillouin lineshape. In this section of the spectrum,

the non-Doppler broadened elastic scattering from the particles, the optics and the like, having virtually the same spectral width as the incident laser light ( $\Delta\nu_{\text{Laser}} \sim 100$  MHz), are filtered away. The molecular scattering becomes Doppler-broadened ( $\Delta\nu_{\text{Rayleigh}} \sim 6$  GHz at 300 K), causing a portion of the scattered light to pass outside of the absorption profile ( $\Delta\nu_{\text{Hg}} \sim 3$  GHz), as evident in Fig. 3.7.

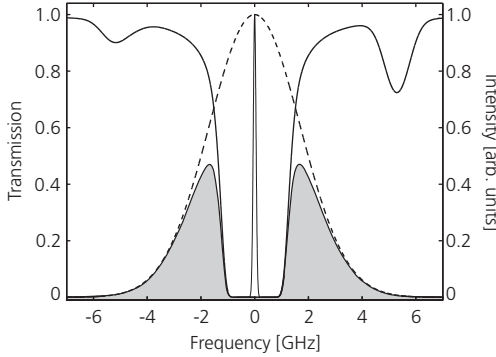


*Figure 3.7* The mercury filter blocks the un-broadened elastically scattered light from particles and from surfaces, whereas the Doppler-broadened wings of the Rayleigh-Brillouin scattering are transmitted. The modelled temperature in the cell is 0°C and the temperature of the scattering medium is 500K.

In determining the temperature on the basis of FRS measurements, the signal intensity is compared with the modelled FRS signal obtained using equation (3.10). However, it is not appropriate to compare the absolute intensities, since measuring the solid angle of collection, losses in the optical arrangement, and the like, is difficult. For convenience, the signal is normalized here to a reference, acquired under identical collection conditions but at known temperature, pressure and species concentration (usually in air at ambient temperature and pressure). In dividing these two detected signals by each other the optics calibration constant  $C$  cancels out. The normalized signal can then be described by

$$\frac{S(\nu_0, T)}{S_{\text{ref}}(\nu_0, T_{\text{ref}})} = \frac{\sum_i \left( N_i \cdot \frac{d\sigma_{Ri}}{d\Omega} \right) \cdot \int_{-\infty}^{+\infty} r_{N_2}(T, P, M_{N_2}, \theta, \nu) \cdot t(\nu - \nu_0) d\nu}{N_{\text{air}} \cdot \frac{d\sigma_{\text{air}}}{d\Omega} \cdot \int_{-\infty}^{+\infty} r_{N_2}(T_{\text{ref}}, P_{\text{ref}}, M_{N_2}, \theta, \nu) \cdot t(\nu - \nu_0) d\nu} \quad (3.11)$$

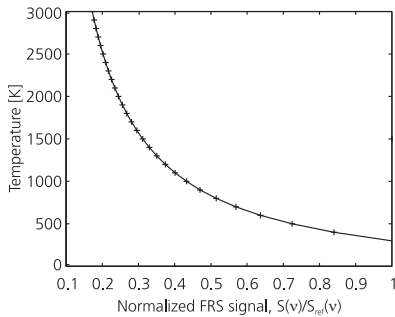


*Figure 3.8* Temperature versus normalized FRS signal.

The ratio of the two is modelled by the S6-modell and the mercury transmission profile. In Fig. 3.8 the relationship is given as a function of temperature.

In the Fig. 3.8 it can be seen that as the temperature increases, the normalized FRS signal decreases. At high temperatures the signal level is low and larger measurement uncertainties are unavoidable. This is not solely a drawback of FRS, since regular Rayleigh scattering is subject to the same decrease in signal. However, whereas the FRS signal is

already reduced by  $\sim 50\%$  through use of the filter, the  $s/n$ -ratio of FRS suffers more from the signal decrease. Further information on filter-based diagnostics can be found in a paper by Boguszko and Elliott [82].

### 3.5 Experimental setup

LRS has been employed due both to its relatively good accuracy and its imaging capability, but its most prominent feature is the simplicity of the setup. As a directly related technique, FRS has the same advantage; the optical alignment is simple, although the filter and a reference setup are added, yet in technical terms FRS is more difficult to deal with. It requires a single-mode, narrow-bandwidth laser, the possibility of frequency controlling the laser very accurately (within  $\sim 100$  MHz) and the frequency stability of the laser during the measurements being crucial to being able to acquire accurate data. The alexandrite laser, described in Section 2.4, has been utilized throughout the FRS work in the thesis work. The development of computer control of the laser wavelength, which is essential in the FRS measurements, is described in Paper I. A schematic setup of FRS is depicted in Fig. 3.9. The part within the dashed rectangle is identical to the setup described in Section 3.2.3 and will thus not be discussed further here, other than stating that the mercury cell is used in the present situation as a frequency reference for the laser system.

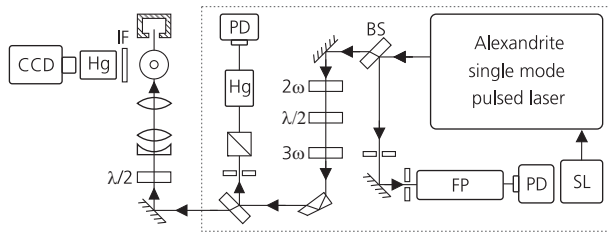


*Figure 3.9 A schematic FRS setup: BS, beam splitter; FP, Fabry-Perot; PD, photo diode; SL, seed laser; Hg, mercury cell; IF, interference filter; CCD, intensified CCD camera.*

The remaining parts are almost identical to a LRS setup. The laser beam polarization (the laser is linearly polarized) is rotated in order to maximize the Rayleigh scattering signal in relation to the position of the observer, as discussed in Section 3.3. Then, dependent on if it is a point, along a line or an imaging measurement the corresponding optics is aligned in the beam path. A typical imaging setup involving standard sheet optics is shown in Fig. 3.9. The laser is focused in the region of interest and is dumped. The detector is placed at a  $90^\circ$  angle to the incident laser beam. The scattered light is observed either through an interference filter or through a reflection filter and an atomic filter and is collected by suitable optics and is registered by a detector, most commonly an ICCD camera, described in Section 2.5.

## 3.6 The application of FRS in combustion diagnostics

In combustion diagnostics FRS is used mainly to measure temperature, but under known conditions it can also be used to measure densities. One can determine the fuel/air-ratio in a binary mixture, if the cross-section of the fuel employed is much larger than that of the air.

Temperature measurement is one of the most important tasks in laser diagnostics. It governs and affects many of the other parameters, e.g. changing it severely influences the chemistry of the flame.

There are different measurement situations, in which reliable, and often two-dimensional, data is required. These can include lean premixed combustion, sooty premixed combustion, diffusion combustion, close-to-surface measurements and measurements in cells at elevated pressures. Various situations of this type will be discussed here briefly and will be coupled with measurements performed within the framework of the thesis.

In developing a technique of this sort, work always starts with use of small-scale laboratory flames that are well characterized or have a simple geometry, in order that the technique can be validated the models and experimental setup be refined to prepare for more complicated measurement situations.

It should be noted that, unless is specifically pointed out to be otherwise, compensation for cross-sections has been made in all the measurements reported.

### 3.6.1 Thermometry measurements in fuel-rich, premixed flames

An attractive case to start with for FRS is to investigate the possibility of obtaining measurements in sooty flames. Measurements in sooty flames, in which acetylene and methane, respectively, were used as fuel, are reported in Paper I and II. The soot particles in these measurements were regarded as being large particles in comparison to the air and fuel molecules, thus falling into the Mie regime. Whether they are is debatable, of course, but close temperature agreement with adiabatic flame temperature calculations is obtained in any case. The principal setup described in the previous section, with the exception of use of an interference filter, was utilized, the cross-sections being taken into account. Estimates of the major species concentrations as well as of the adiabatic flame temperature were made by use of the Olikara and Borman equilibrium routines.

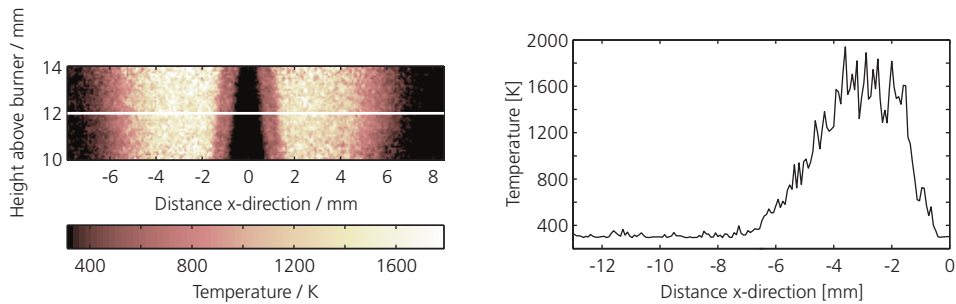


*Figure 3.10* The single-shot temperature distribution in a methane/air flame,  $\Phi = 1.56$ , is shown at the left, and the temperature at a level 12 mm above the burner, a level marked by a white line in the left-hand image, is shown at the right. The adiabatic flame temperature in this flame is  $\sim 1860$  K.

A single-shot temperature distribution for a methane/air flame having a fuel/air ratio of  $\Phi = 1.56$ , is shown in Fig. 3.10. The adiabatic flame temperature was calculated as being  $\sim 1860$  K. It is, of course, not reasonable to reach the adiabatic flame temperature, mainly because of the heat loss due to soot radiation. Thus the temperature data presented is in close agreement with the situation described. In Fig. 3.10, a one-dimensional plot of the radial temperature at a position 12 mm above the burner is shown at the right and a 2D measurement is shown at the left.

### 3.6.2 Thermometry measurements in a lean, premixed, low-swirl burner

The low-swirl burner described in Section 2.7.2 was investigated in Paper III. The measurements made were of the velocity field, the OH- distribution and the temperature, all obtained in two dimensions, for model validation purposes. This was the first step in the development of the detailed large-eddy simulation (LES) database reported on in Paper A.

Simultaneous measurements of FRS and high speed OH-LIF measurements were obtained, an example being presented in Fig. 3.11. The dashed box in the second OH-image indicates the area in which the FRS measurements were obtained at  $400 \mu\text{s}$  following the first OH-LIF image. The signal-to-noise ratio of the temperature measurement was estimated to be 5-10:1 depending on the temperature. The reason for using FRS instead of LRS here is that the system was not completely clean, due to earlier PIV measurements. This potential difficulty was overcome by use of FRS.

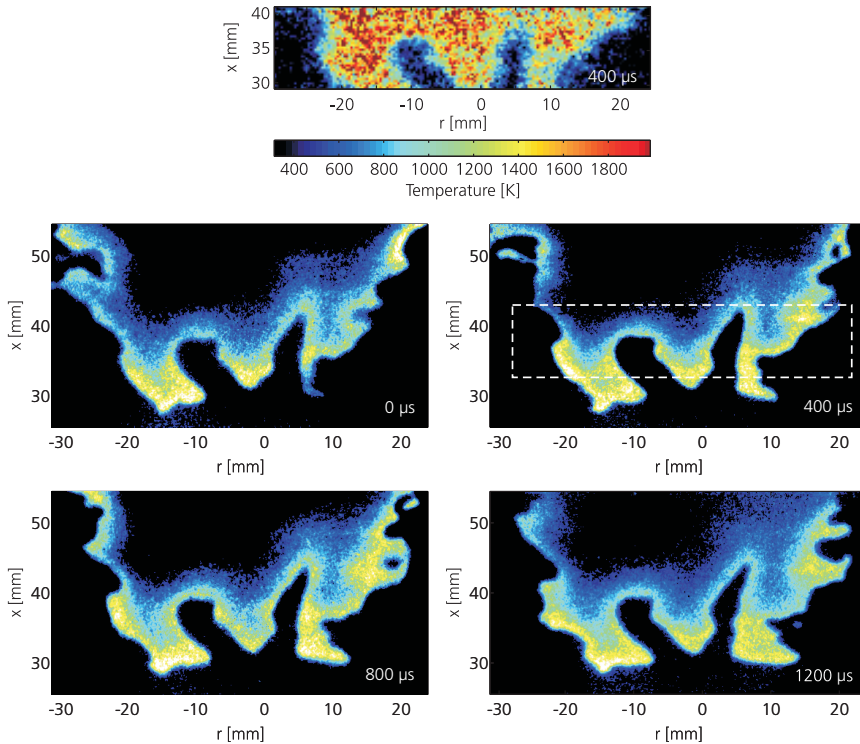


*Figure 3.11* A single-shot FRS temperature image (top) followed by a sequence of four OH-LIF images for which  $\Delta t = 400 \mu\text{s}$ , the white dashed line showing the area in which the temperature measurements were made.

Statistical data on the average radial temperature at two different heights and for two different flames was also acquired and rms values derived, see Fig. 3.12. The temperatures (black lines) were derived from one of the pixel-rows in the two-dimensional data and was averaged over 600 single-shot images, the rms values (gray line) being calculated from these 600 images. The adiabatic temperature of the flame is 1705 K, which is nearly achieved in the postflame zone. The large rms values are due mainly to fluctuations of the flow in the flame, meaning that measurements are sometimes made in the burned and sometimes in the unburned region. A detailed account of this work is presented in Paper III and the LES modelling work is presented in Paper A.

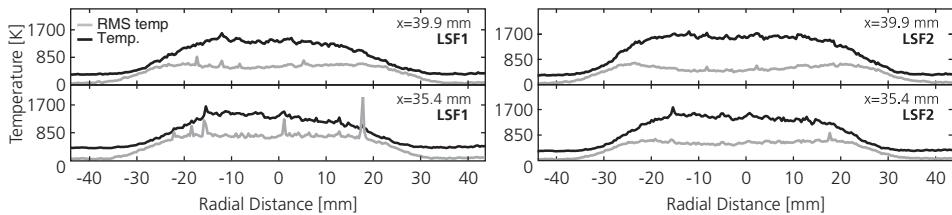


*Figure 3.12 Radial temperature profiles and rms values, the black line denoting the temperature and the gray the rms value.*

Earlier work on simultaneous FRS and PIV measurements has been carried out by Most et al. [58,83] and by Elliott et al. [59]. The measurements were performed in small laboratory flames, with very well controlled seeding of the seeding particles ( $0.3 \mu\text{m TiO}_2$  and  $2.4 \mu\text{m}$  ceramic, respectively). In both cases, a single-mode Nd:YAG laser and a molecular iodine filter were paired with each other. Elliott et al. took up clearly the difficulties there were in blocking the light scattered by the particles. Most et al. stated that rejection was sufficient, with the exception of the occurrence of agglomerates that could not be blocked completely. Since the rejection ratio of the mercury filter is much higher than that of iodine, success was possible. Accordingly, the feasibility of simultaneous FRS and PIV was explored.  $\text{ZrSiO}_4$  particles of  $0.5 \mu\text{m}$  size were used in the measurements. The PIV system employed was a standard PIV system outfitted with two Quantel Brilliant B lasers and an un-intensified LaVison CCD camera; which meant that the PIV was in need of strong seeding in order for reliable results to be obtained. This made the seeding difficult to control, resulting in the production of agglomerates. Thus, obtaining simultaneous PIV and FRS measurements was not feasible here.

### 3.6.3 Thermometry measurements in a Wolfhard-Parker diffusion flame

To study the feasibility of FRS in non-premixed flames, measurements in a methane diffusion flame stabilized on a Wolfhard-Parker burner were conducted. The burner is described in Section 2.7.3 and the principal setup of FRS in Section 3.5. Generally speaking, Rayleigh scattering measurements in non-premixed flames are difficult to obtain due to their dependence on the cross-section. Kearney et al. [84] performed simultaneous FRS and Raman measurements nevertheless, where the Raman data being used then for measurements of species concentrations. In the present measurements, the major species concentrations in the flame were determined from Smyth [85], calibrated thermocouple temperature measurements also being available, making it possible to carry out and validate cross-section-compensated FRS measurements. The results can be found in Fig. 3.13, and the measurements are described in greater detail in Paper II.

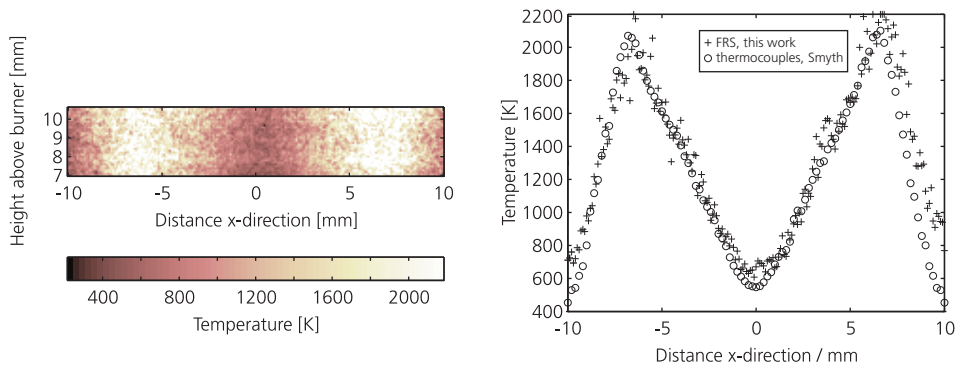


*Figure 3.13* A single shot two-dimensional temperature measurement conducted in a Wolfhard-Parker burner is shown to the left and a 10-shot average-temperature profile of the temperature at a level 9 mm above the burner is shown at the right. The circles indicate calibrated thermocouple measurements made by Smyth [85] and the crosses FRS measurements obtained here.

### 3.6.4 Temperature gradients close to surfaces

The determination of temperature gradients close to a stainless steel surface by use of FRS was reported in Paper IV. Spatially resolved measurements of the heat transfer between solids and the gas phase is important, especially in the design of energy-transforming applications such as gas turbines and combustion engines. In the present study, FRS was used for temperature measurements in the gas phase and a thermographic phosphor for the measurement of surface temperatures.

In the setup, an electrical inline heater with a 10.5 mm nozzle diameter was placed in the centre, beneath a circular stainless steel plate (200 mm in diameter and 10 mm thick). The tripled alexandrite laser sheet was then directed between the inline heater and the steel plate, touching the surface of the steel plate. This enabled measurements as close as possible to the surface to be made.

In the FRS measurements some of the single-shot images showed there to be a highly localized interfering signal. Further investigation indicated the surface-scattered interfering signal that was transmitted through the mercury filter to be 10 times stronger than that of the direct laser beam, showing the frequency to be shifted slightly or to be broadened, that indicating the calculated rejection-ratio of the filter shown in Fig. 3.1 to not be valid. Yet, two-dimensional temperature data down to  $\sim 250 \mu\text{m}$  from the surface could still be derived. Temperature profiles as a function of the distance from the plate at six different radial positions, as well as an averaged two-dimensional temperature distribution, are shown in Fig. 3.14. Further information on the FRS measurements there are presented together with the thermographic phosphor measurements reported in Paper IV.

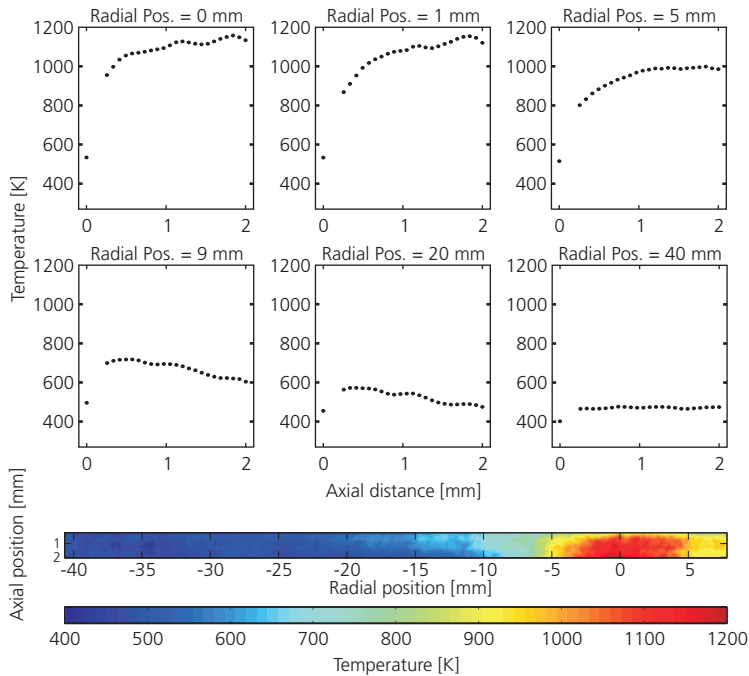


*Figure 3.14 Axial temperature profiles (at the top) at six different radial positions. The temperature at the axial position 0 mm is taken from the phosphor measurements. The averaged temperature distribution of the gas phase was measured by FRS spanning a distance between 250  $\mu\text{m}$  and 2 mm from the plate surface.*

### 3.6.5 Temperature measurements in an ignition cell

An ionization sensor is an electrical sensor for on-line diagnostics in combustion engines. The information collected by the sensor can be used for feedback control of the engine. The energy released by the combustion process leads to an increase in the ionization level in the combustion chamber and hence to a higher conductivity of the gas. Applying a voltage across the electrode gap of the spark plug after ignition of the mixture generates a current that contains information concerning the combustion that occurs [86].

It was of interest to measure the temperature between the electrodes. The measurement conditions, close to the electrodes and in a cell in which there was multi-reflected stray light, made FRS a suitable technique to exploit.

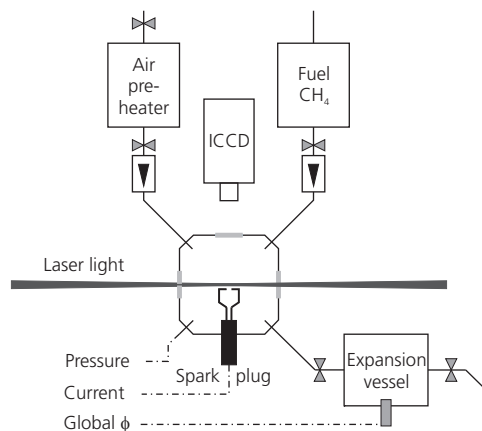


*Figure 3.15 A schematic setup of the ignition cell.*

The experiments were conducted in a constant-volume combustion cell into which air and fuel were injected separately and were ignited after a predetermined mixing time. A schematic layout of the combustion cell is shown in Fig. 3.15.

The combustion chamber is approximately cubic and has a volume of 167 cm<sup>3</sup>. It consists of three orthogonally intersecting cylindrical passages in a block of stainless steel. Each of the cylindrical passages can be sealed by fused silica windows, providing full optical access to the combustion chamber. The cell also has diagonal passages, which are connected to an air injection system

and a fuel injection system for the injection of preheated air and methane, respectively. The mixture of air and fuel is ignited by an inductive ignition system connected to a spark plug having thin (~1 mm) elongated electrodes. The electrode gap is located at the center of the combustion chamber. A vacuum pump system provides for evacuation of the combustion products, direct-acting magnetic valves control the inlet and outlet of gases.

Four parameters were measured in each combustion cycle: the combustion pressure, the ion current, the global equivalence ratio and the two-dimensional temperature distribution. The temperature was measured using FRS. Here a 2 mm vertical sheet having a pulse energy of ~10 mJ was passed ~0.5 mm behind the electrode gap.

The magnetic valves, the ignition system and the FRS system, as well as the logging of pressure, ion current and global equivalence ratio, were controlled by a PC by means of a 12 bit A/D card. A combustion cycle was started by the injection of ~5 bar of air into the evacuated combustion chamber. Methane was then injected into the quiescent air. After a predetermined mixing time, a spark with a duration of approximately 600 μs was fired, igniting the air/fuel mixture. Approximately 40 μs prior to ignition, the laser and the CCD camera were synchronously triggered so as to register the two-dimensional temperature distribution. After combustion, the hot gases were expanded into a vessel for measurement of the global equivalence ratio. Finally, the vessel and the

combustion chamber were evacuated for 15 seconds down to a pressure of  $\sim 0.1$  bar.

The case presented here ( $\lambda = 1.25$ ) is one early in the combustion process, 23 ms after ignition, when both burned and unburned gas were present.

There is approximately a 1.1 mm gap between the electrodes of the spark plug. Figure 3.16 shows clearly how the temperature rises quickly from  $\sim 400$  K to 1700 – 1750 K, with a drop in the middle.

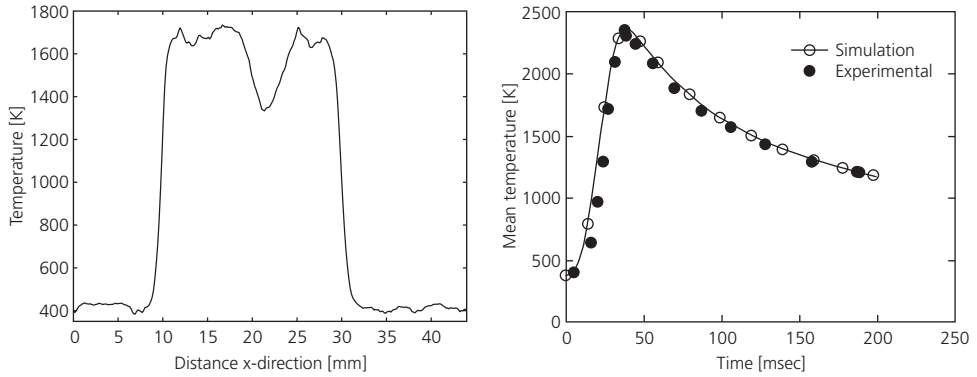


**Figure 3.16** The temperature along a line (on the left) in the ignition cell 23 ms after ignition at  $\lambda = 1.25$  has occurred. Due to heat transfer from the electrodes a temperature dip in the middle of the high temperature region occurs. The temperature profile agrees well with both the modeled and the expected values. Both temperature simulation and measurement of the average temperature in the cell were carried out. The measurements were made with a thermocouple and the simulations by means of a multi-zone model. The simulations were made available at the courtesy of Abdelhadi Ahmed, Energy Sciences, Lund University.

The temperature drop in the middle of the high-temperature region is caused by heat transfer from the gas to the electrodes, providing a cooling effect on the burned gases. The modeled and the measured global temperature, presented as a function of time, are shown in Fig. 3.16. Comparing the measured and the modeled global temperature with the, instantaneous temperature measured by FRS 23 ms after the ignition, showed them to be in close agreement. On this time scale, the temperature of the unburned gas should not have increased, and a temperature of 400 K in the unburned region is reasonable while the initial temperature in the cell was 386 K, as measured by a thermocouple (a slightly elevated starting temperature is preferable experimentally, since water from the combustion process condenses on the inside of the optical windows otherwise).

### 3.6.6 Fuel/air ratio measurements

As mentioned above, Rayleigh scattering can hardly be used for species-specific measurements. However, both density and ratio measurements on binary mixtures under known conditions are feasible if the species involved considerably differ in their cross-section. This can be utilized in measuring the fuel/air ratio. It is tricky to quantify the fuel/air ratio, especially while the Rayleigh-Brillouin scattering profile changes for larger molecules. Earlier studies using LRS in Diesel and spark-ignition engines shows to be promising for use in measuring quantitative fuel distributions, [87,88] and [89], respectively. However, as mentioned earlier, LRS suffers from the elastic scattering, making it very difficult to perform measurements inside small compartments. FRS could thus be an alternative.

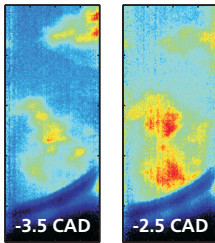


*Figure 3.17 The fuel distribution in the Volvo D5 engine at -3.5 and -2.5 CAD, respectively.*

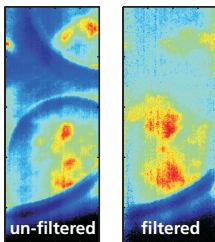


*Figure 3.18 The difference between filtered and un-filtered Rayleigh scattering in the Volvo D5 engine. Note the valves in the left image.*

Proof-of-principle measurements for visualizing the distribution of evaporated fuel in a Diesel engine without use of fuel-tracer have been performed within a Diesel project in which 70% n-heptane and 30% iso-octane were used as fuel. The cross-sections found in Table 3.2, yield a cross-section ratio of fuel to air of  $\sim 60$  and  $80$ , respectively. The measurements were conducted in a Volvo D5 engine, the data being acquired at different crank-angle degrees (CAD). Images from two different CADs are shown in Fig. 3.17, the fuel distribution in the direction of the spray being clearly visible there.

As the fuel decomposes, fluorescence and absorption becomes a problem in the UV-spectral range, as reported by Richter et al. [90], limiting the UV-FRS. This was obvious in the present measurements, the exact time of ignition (approx. at  $-1.5$  CAD) not being possible to determine due to absorption and fluorescence. It was also evident that the scattering from the spray core of the Diesel jet could not be blocked by the mercury filter, although most of the other scattering could be blocked, as shown in Fig. 3.18. This limits the measurement time window to between  $\sim 0.5$  CAD after the injection ends to approximately when the combustion starts. In these measurements, 3.5 % EGR was employed and the injection started at  $\sim 10$  CAD.

In order to continue similar measurements, absorption measurements need to be performed in the engine. To be able to extract quantitative data the Rayleigh-Brillouin lineshape of the large and heavy fuel molecules involved needs to be studied carefully.



# Chapter 4

## Polarization spectroscopy (PS)

Minor species of very low concentration need to be determined accurately, both for validation of specific combustion models and for gaining an overall understanding of combustion processes generally. Polarization spectroscopy (PS), a fully resonant non-linear technique, is well-suited through its coherent nature, creating a laser-like signal beam with very high signal-to-noise ratio, providing measurements of species concentrations even at ppm levels. In this chapter the application of PS to combustion diagnostics, both in the UV/visible and the infrared (IR) spectral regime, will be discussed.

### 4.1 Introduction to polarization spectroscopy

Polarization spectroscopy was first described by Wieman and Hänsch [91], when working on refinements of saturation spectroscopy in order to accurately measure the Rydberg constant ( $109\,737.3156\,852\,7(73)\text{ m}^{-1}$  [92]). It has a better signal-to-background ratio than saturation spectroscopy and provides the same possibilities for Doppler-free detection. The technique is described very well by Teets et al. [93] and Demtröder [94]. A review, from a combustion diagnostics point of view, is presented in [4]. Already in 1984, Tong and Yeung [95] employed PS for the detection of trace element (sodium and barium) in flames. They pointed out that the coherent nature of PS can be used to suppress the emission from such molecular species as OH, CH, C<sub>2</sub> and CN, all of which are important species in combustion. Two years later, the first work involving use of pulsed lasers was published [96]. In that study measurements of the sodium present in a flame were conducted and the dependence of the PS-signal on the crossing-angle was investigated. That same year the first Doppler-free two-photon PS measurements were performed, hydrogen being detected in high-temperature plasmas [97]. Those measurements were also investigated theoretically by Seidel [98].

The application of PS within combustion diagnostics was sparked several years later by Nyholm et al. [99], who in 1993 applied polarization spectroscopy to the detection of the hydroxyl-radical in flames, achieving an estimated detection limit

of better than  $10^{14}$  molecules/cm<sup>3</sup>. Already the same year the first two-dimensional PS measurements in flames were reported, [100], this also involving detection of the hydroxyl-radical in a CH<sub>4</sub>/O<sub>2</sub> flame. Nyholm demonstrated the possibility of measuring temperature by polarization spectroscopy through use of the Boltzmann plotting method [101], obtaining two-dimensional measurements while employing a dual-wavelength approach to probe two rotational lines. Use of PS measurements here was compared with the use of degenerate four-wave mixing. The authors found PS to be superior due in particular to its relative simplicity [102]. In the 90s, several other species important to combustion were measured such as NH<sub>3</sub>, CO [103], C<sub>2</sub> [104], NH [105] and N<sub>2</sub> [106].

The physics of polarization spectroscopy, investigated by direct numerical integration (DNI) of the time-dependent density matrix equation, was explored by Reichardt and Lucht [107], in calculating lineshapes and saturation effects. The model was later developed further to include multi-axial-mode laser effects [108], important for an understanding of polarization spectroscopy and for accurate quantitative concentration measurements. The same research group also investigated the use of saturated polarization spectroscopy for quantitative measurements of OH number densities experimentally [109]. A simplified model describing the curve shape of polarization spectroscopic power-dependence scans in both the saturated and unsaturated regime was proposed later by Walewski et al. [47], the model agreeing well with experimental results concerning lines dominated by inhomogeneous broadening.

Polarization spectroscopy using picosecond lasers has also been investigated, both experimentally [110] and theoretically [111].

In combustion diagnostics there has been a strong interest in measuring species that lacking transitions in the UV/visible spectral range. These include such species as CH<sub>4</sub>, C<sub>2</sub>H<sub>2</sub> and CO<sub>2</sub>. Polarization spectroscopy was first used in the mid-infrared spectral regime to detect carbon dioxide at 2.7  $\mu\text{m}$  [112], an important step for obtaining sensitive, spatially resolved measurements.

Continued development of this sort within the mid-infrared spectral regime was an important goal of the thesis work, measurements of CO<sub>2</sub> and water that were conducted were reported in Paper VII and XI, XII, and measurements of small hydrocarbons in Papers V, VIII, IX and X as well as measurements of CH presented in Paper V. Two-dimensional measurements of atomic hydrogen were also reported in Paper VI.

## 4.2 Basic concepts of polarization spectroscopy

Polarization spectroscopy uses polarized light to selectively detect a given species, a strong either linearly or circularly polarized pump beam being crossed by a weak, linearly polarized probe beam in the region that is investigated. A signal is generated where the beams intersect, the crossing angle determining the spatial

resolution. This can be carried out in either a counter- or a co-propagating manner (see Fig. 4.1), the co-propagating approach providing a stronger signal but the counter-propagating enabling sub-Doppler detection to be preformed.

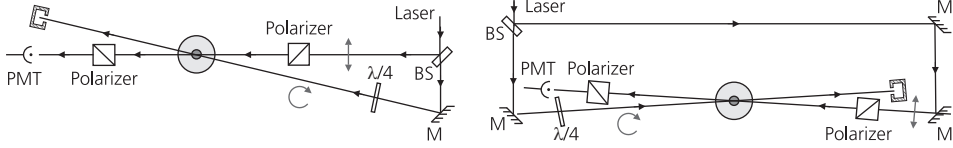


**Figure 4.1** Schematic PS-setup; at the left a co-propagating beam geometry is shown, and at the right a counter-propagating beam geometry used for sub-Doppler measurements. (M, mirror; BS, beam splitter; PMT, detector) Polarization of the pump and of the probe beam is marked by gray arrows.

Usually, the two laser beams are produced by the same laser source, meaning that they have the same initial polarization. Polarization of the pump beam is either rotated by use of a  $\lambda/2$ -plate or is converted into circular polarization by use of a  $\lambda/4$ -plate. The account here will assume there to be a right-hand circularly polarized pump beam and a linearly polarized probe beam.

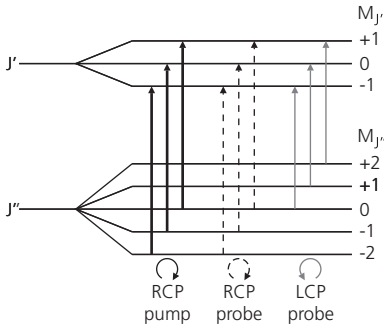


**Figure 4.2** Linearly polarized light can be regarded as a linear superposition of left- and right-circularly polarized light (denoted as LCP and RCP, respectively) of equal amplitude. The right-hand circularly polarized pump beam induces transitions, where  $\Delta M = +1$ . This results in absorption and phase shift for the probe beam components differing.

When the laser is tuned to a particular molecular resonance, the circularly polarized pump beam induces transitions to magnetic sub-levels, but only between levels differing in the magnetic quantum numbers associated with them. Note that  $\Delta M$  equals  $+1$  and  $-1$ , for right- and for left-circularly-polarized light, respectively, see Fig. 4.2. Optical pumping of this sort leads to a non-uniform population distribution over the different ground-state sublevels, resulting in the sample becoming anisotropic, i.e. it changes the real (birefringence) and imaginary (absorption, dichroism) parts of the refractive index in the sample.

The linearly polarized probe beam, which can be considered as representing the sum of left- and right-circularly-polarized components of equal intensity, is affected by the birefringence and dichroism that are induced. The two components differ in the dispersion,  $\Delta n$ , and absorption,  $\Delta\alpha$ , they experience,

which results in the absorption being stronger for the left-hand circularly-polarized light (involving a right-hand circularly-polarized pump). The dispersion that occurs leads to a slight rotation of the polarization, and the absorption that occurs

results in a certain ellipticity, Fig. 4.3. This change of polarization in the probe beam makes it possible for a small part of the probe beam to pass through the second polarizer, often called the analyzer. This signal beam can then be collected by a detector. The stronger the optical transition is, the stronger the tilt of the ellipse and the more pronounced the ellipticity becomes.

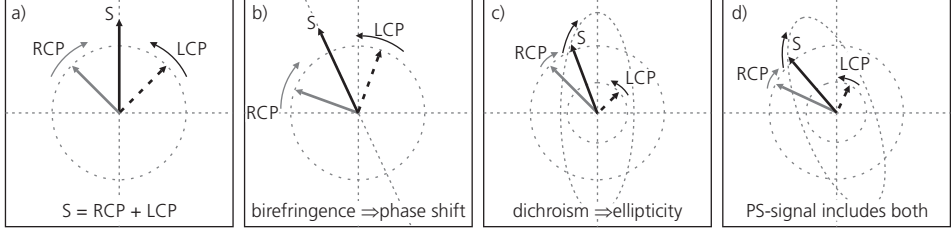


**Figure 4.3** Changes in the polarization of the probe beam where  $S$  is the probe beam vector: a) the probe beam can be regarded as a superposition of a right- and of a left-circularly polarized component (RCP and LCP, respectively, the vectors rotating in the plane indicated by the arrows); b) the birefringence produced causes a phase change, rotating the plane of polarization; c) the dichroism induces ellipticity due to the uneven absorption of the two components; d) both the birefringence and the dichroism give rise to the PS signal.

#### 4.2.1 Line profiles of the PS-signal

A simple model of the polarization signal in the unsaturated or the weakly saturated regime is derived in [93,96]. The model ignores the effects of the repopulation of the ground-state due to fluorescence and to collisions. It also assumes the length of the pump pulse to be shorter than the relaxation time for the ground-state and that the upper state is sufficiently short-lived to not contribute to the anisotropy that is induced.

If the differences in the absorption and the dispersion experienced by the two circularly polarized components is small, i.e. when  $\Delta n$  and  $\Delta\alpha \ll 1$ , the intensity of the probe beam transmitted through the analyzer can be described, as in [99], by

$$I_{PS} = I_{probe} \left[ \xi + \theta^2 + b^2 + \frac{\theta\omega L}{c} \Delta n + \frac{1}{2} b \Delta\alpha L + \left(\frac{L}{4}\right)^2 (\Delta\alpha)^2 + \left(\frac{\omega L}{2c}\right)^2 (\Delta n)^2 \right], (4.1)$$

where  $I_{probe}$  is the incoming probe intensity,  $\omega$  the laser frequency,  $L$  the length of the absorption path,  $b$  an extra ellipticity due to background birefringence from elements introduced between the two polarizers (such as cell windows),  $\xi$  is a background originating from the finite extinction ratio of the polarizer pair, and  $\theta$  is the angle at which the analyser deviates from the perfect crossed position. In most diagnostic measurements (in fact in all the measurements presented in the present work) the crossing of the polarisers is either perfect or close to perfect and

there is no background birefringence in between the polarizer pair or only a negligible amount of it, leaving both  $b$  and  $\theta$  basically equal to zero, simplifying the expression above.

According to Wiemann and Hänsch the line profile of  $\Delta\alpha$ , which is Lorentzian in the case of low laser intensities and lie within the limits of large Doppler widths [91], can be written as

$$\Delta\alpha = \frac{\Delta\alpha_0}{1+x^2}, \quad \text{with} \quad x = \frac{\omega_0 - \omega}{\gamma_s/2}, \quad \text{and} \quad \Delta\alpha_0 = \Delta\alpha(\omega_0) \quad (4.2)$$

where  $\gamma_s$  corresponds to the homogeneous width of the molecular transition saturated by the pump beam and  $\omega_0$  is the central frequency of the transition.

The absorption coefficient,  $\Delta\alpha$ , and the refractive index,  $\Delta n$ , are related to each other by the Kramers-Kronig dispersion relationship [94], meaning that  $\Delta n$  can be expressed as

$$\Delta n = \frac{c}{\omega} \cdot \frac{x\Delta\alpha_0}{1+x^2}. \quad (4.3)$$

If equations (4.1) and (4.2) are inserted into (4.3) and  $b$  and  $\theta$  are equal to zero, the line profile of a circularly polarized pump beam can be expressed as

$$I_{PS} \cong I_{probe} \left[ \xi + \left( \frac{1}{4} \Delta\alpha_0 L \right)^2 \frac{1}{1+x^2} + \left( \frac{1}{2} \Delta\alpha_0 L \right)^2 \left( \frac{x}{1+x^2} \right)^2 \right]. \quad (4.4)$$

In most cases  $\Delta\alpha_0 L \ll 1$ , which means that the last term in (4.4), which is proportional to  $\Delta\alpha_0^2 L^2$ , is negligible, leaving only the first two terms.

$$I_{PS} \cong I_{probe} \left[ \xi + \left( \frac{1}{4} \Delta\alpha_0 L \right)^2 \frac{1}{1+x^2} \right] \quad (4.5)$$

This simplified relationship (4.5) is also valid when a linearly polarized pump beam is employed under the same conditions. The major difference between the linear and the circular pump is in terms of absorption. The absorption occurring can be expressed as

$$\Delta\alpha_0 = -\frac{N^0 \sigma_{JJ'} I_{pump} \zeta_{JJ'}}{S}, \quad \text{with} \quad S = \frac{\hbar\omega}{t\sigma_{JJ'}} \quad (4.6)$$

where  $\sigma_{JJ'}$  is the cross-section, which is not dependent upon the polarization [99],  $I_{pump}$  and  $t$  are the intensity and the pulse length, respectively, of the pump beam,  $S$  is a saturation parameter which is independent of polarization,  $N^0$  is the total number density in the lower state, which is temperature dependent, and  $\zeta_{JJ'}$  is the geometry factor, which is dependent upon the pumping geometry and the angular

momentum of both the upper and the lower states in the transition which is probed being given in [93].

In the case of a circularly polarized pump beam, the  $\zeta_{JJ'}$  factor approaches  $3/2$  for large  $J$  values when  $\Delta J = \pm 1$  but decreases rapidly with increasing  $J$  when  $\Delta J = 0$ . This means that a circularly polarized pump beam favours the  $P$  and the  $R$  lines. When instead a linear pump beam is utilized, the factors approach  $3/10$  for large  $J$ -values and  $J \neq 0$  and  $6/5$  for  $J = 0$ , which means that a linearly polarized pump beam favours the  $Q$  lines [99]. This is shown in Fig. 4.4, where an infrared spectrum of hot water lines (1000 K) is simulated for the different polarization geometries.

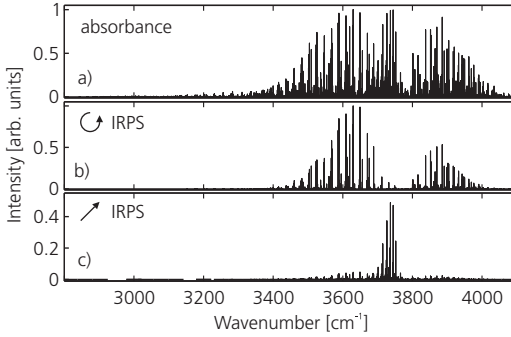


*Figure 4.4 Simulated hot water lines at 1000 K: a) the total spectrum; b) the spectrum simulated for a circularly polarized pump beam, the R- and the P-branch being enhanced; c) the spectrum is simulated for a linear pump beam, the Q-branch being enhanced.*

It should be noted that the Lorentzian profile introduced by Wieman and Hänsch under the abovementioned conditions was confirmed 23 years later, in 1998, by Reichardt and Lucht [107], on the basis of DNI calculations. However, in unsaturated polarization spectroscopy the lineshape for a homogeneously broadened line, i.e. when the collisional broadening predominates, is Lorentzian-cubed. This was shown for  $\text{CO}_2$  in Paper VII. The shape can be described then by

$$I_{PS} \cong I_{probe} \left[ \xi + \left( \frac{N^0 \sigma_{JJ'} L I_{pump} \zeta_{JJ'}}{4S} \right)^2 \left( \frac{1}{1+x^2} \right)^3 \right]. \quad (4.7)$$

Note that, in all the discussions above, dependence upon repopulation of the ground-state is neglected, leaving a squared dependence of the PS-signal on the total number density found in the ground state,  $I_{PS} \propto (N^0)^2$ .

#### 4.2.2 PS-signal dependence on laser fluence

Polarization spectroscopy can be performed either with or without saturation. Most diagnostic measurements are performed during saturation, when the signal is less sensitive to pulse-to-pulse fluctuations and generate a stronger signal, which improves the signal-to-noise ratio, a matter especially important in the IR-regime, because of the low detector sensitivity there. Also, in the saturated regime the signal is less sensitive to collisions than it is in the unsaturated regime [107].

In a Doppler-dominated region, the PS-signal scales as

$$I_{PS,unsaturating} \propto (I_{pump})^2 I_{probe} \left( \frac{1}{\Delta\omega_D} \right)^2 \left( \frac{1}{\Delta\omega_C} \right)^4 \quad (4.8)$$

in the case of unsaturating beams (this is what was discussed above) and

$$I_{PS,saturating} \propto I_{probe} \left( \frac{1}{\Delta\omega_D} \right)^2 \left( \frac{1}{\Delta\omega_C} \right)^{<1} \quad (4.9)$$

in the case of saturating beams [107]. It can be clearly seen from these two expressions, (4.8) and (4.9), that both the pulse-to-pulse fluctuations and the collisions that occur will influence the signal much more strongly in the unsaturated regime than in the saturated regime.

The approach of Reichardt and co-workers [107], involving DNI calculations, is based on complex and numerically demanding calculations. A simplified model that describes the shape of the polarization-spectroscopy-saturation curves when homogeneous broadening predominates, was put forth by Walewski et al. [47]. It is given by

$$I_{PS} = I_{probe} N^2 A \left( \frac{I_{pump}}{I_{pump} + I_{sat}^{PS}} \right)^2 \quad (4.10)$$

where  $A$  is a scaling factor,  $N$  is the number density of the species which is probed, and  $I_{sat}^{PS}$  is the PS saturation intensity. This model provides satisfactory results both in the saturated and in the partially saturated regime; it is not valid, however, when inhomogeneous rather than homogeneous broadening predominates.

### 4.3 Application of PS in combustion diagnostics

As mentioned earlier, measurements of trace species are important in combustion. Polarization spectroscopy, due to its coherent nature, is an attractive option, through its ability to suppress background, by remotely detecting the signal, without signal losses.

In this section, a summary is presented of the results and conclusions reported in the papers included in the thesis. The work contains results from both the UV/visible and the mid-IR spectral region.

### 4.3.1 Detection of the CH radical through PS

CH is a crucial trace species in hydrocarbon combustion. In particular, it takes part in the decomposition reactions of the primary fuel. CH is also widely accepted as one of the best flame front markers for investigating turbulent flame structures, since it only exists in a very thin layer within the reaction zone. In the next chapter laser-induced fluorescence (LIF) for the visualization of CH will be taken up. Here the application of sub-Doppler polarization spectroscopy to the measurement of CH in combustion is focused on.

A counter-propagating beam geometry was used, in order to enable sub-Doppler measurements to be made and measure the line profiles of both LIF and PS.

The experimental setup is described in detail in Paper V. In short, a frequency doubled, single-longitudinal-mode alexandrite laser (described in Section 2.4 and in Paper I) was used for excitation, the measurements being obtained in a slightly rich methane/oxygen porous plug burner flame (described in Section 2.7.4) located in a low pressure chamber (described in detail in [47]), at a pressure of 60 mbar.

These measurements were used to investigate the  $R_2(5)$  line of the B-X(0,0) transition. Saturation curves were obtained for both LIF and PS. The PS saturation curve was fitted by a least square fit to the phenomenological equation in (4.10) and to the LIF by

$$I_{LIF} \propto \left( \frac{I_{pump}}{I_{pump} + I_{sat}^{LIF}} \right) \quad (4.11)$$

where  $I_{sat}^{LIF}$  is the saturation intensity for LIF. The saturation fluences were determined to be 5 J/cm<sup>2</sup> for PS and 70 J/cm<sup>2</sup> for LIF.

Lineshape studies were conducted, the lineshapes being compared with each other. Fig. 4.5 shows two lineprofiles, to the left is a PS-signal close to saturation and to the right a LIF profile for the same laser energy i.e. unsaturated. At this laser energy the LIF signal is strongly affected by noise, however, the noise level decreases substantially at saturation energies as is evident in Paper V.

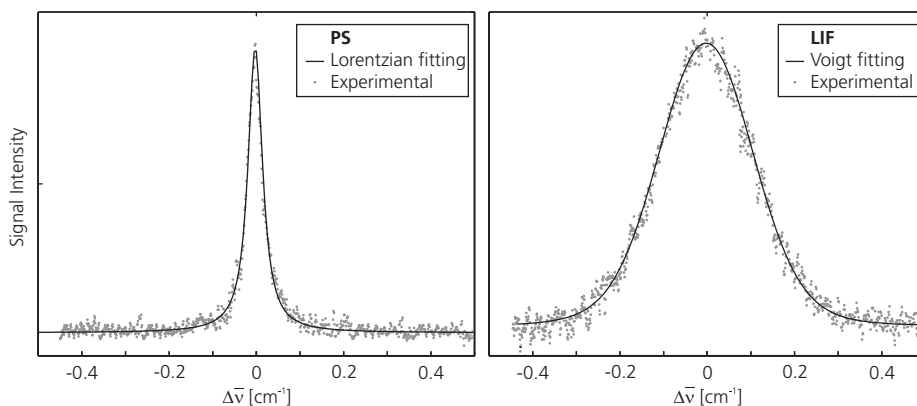


*Figure 4.5 At the left the sub-Doppler PS lineshape of CH just above saturation is shown, and at the right the lineshape of the unsaturated LIF signal, fitted with a Voigt-profile. The substantial Doppler broadening of the LIF profile as compared with the PS is clearly visible.*

The line profile evident in the case of PS was expected from a theoretical standpoint. A pure Lorentzian profile (black solid line) was fitted to the experimental data as discussed in the previous section, implying the signal to be well saturated. This work concerned with lineshapes can be compared to the work dealing with PS in the mid-IR spectral regime, in which the IRPS of CO<sub>2</sub> at 2  $\mu\text{m}$  was investigated and was compared to IRLIF of the same transition. These measurements were conducted under non-saturated conditions. Here a Lorentzian cubed profile could clearly be fitted to the IRPS signal due to the lack of saturation; as is discussed in Section 4.2.1.

The LIF measurements reveal a Voigt-profile having a strong Gaussian contribution originating from inhomogeneous Doppler broadening, as well as a constant Lorentzian contribution due to collisions. Both PS and LIF experienced a substantial power broadening at high laser energies, indicating that accurate measurements should be carried out by PS just above saturation energies.

The work conducted showed there to be the possibility of obtaining high resolution measurements in harsh environments when studying molecular radicals, making it possible to compare PS and LIF directly, since the measurements are conducted simultaneously.

### 4.3.2 Imaging of hydrogen atoms in flames

The hydrogen atom, investigated now for more than a century, is the smallest atom. Study of it has made it easier today for physicists to understand the spectroscopy of much more complicated atoms and molecules. Hydrogen is also an important species in combustion, for instance in flame kinetics, where it is a key species in chain-branching reactions due to its diffusivity and reactivity. Thus, the

sensitive spatially resolved detection of atomic hydrogen is important not only for combustion but also for plasma and fusion studies.

The single-photon excitation of hydrogen is not possible generally, since reaching the lowest excited state requires vacuum ultraviolet (VUV) radiation at 121.6 nm. Multi-photon excitation has been employed, however, in several studies involving use of LIF e.g. [113-115] in flames, or of two-photon polarization spectroscopy (TPPS) in plasmas [97,98,116] and in flames [117], as well as in 2007 by two-colour two-photon-resonant six-wave-mixing spectroscopy [118].

In the present work, Paper VI, a new scheme for atomic hydrogen detection in flames was employed. The scheme, termed two-photon pump polarization spectroscopy probe (TPP-PSP), involves two-photon excitation of the hydrogen atom (the  $1s$ - $2s$  transition) and is achieved by use of a strong pump beam at 243 nm. The population at the  $2s$  level is then probed by conventional polarization spectroscopy, the  $2s$ - $4p$  transition being studied, both the pump and the probe having the same wavelength, 486 nm. In this way only the population at the  $2s$  level is probed, meaning that no phase matching or molecular alignment of the two differing excitation processes is required.

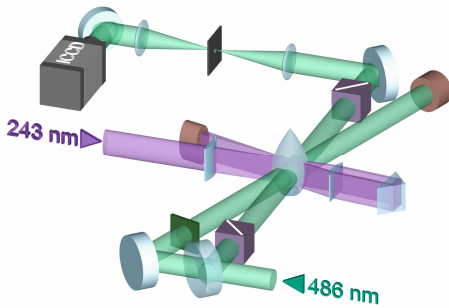


Figure 4.6 Schematic setup of the TPP-PSP.

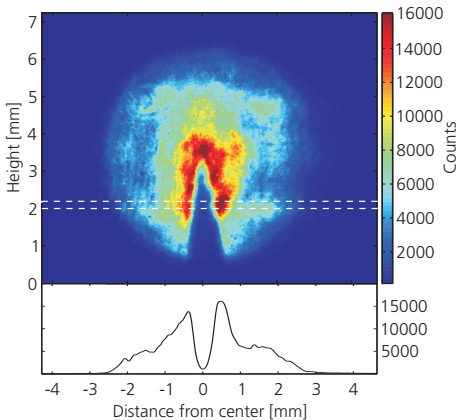


Figure 4.7 Single-shot TPP-PSP image of ground-state hydrogen atoms recorded in a  $\Phi = 1.3$  hydrogen/oxygen flame.

The setup is depicted schematically in Fig. 4.6. An important point is that this excitation scheme requires only one laser source. In the present work, the optical parametric oscillator (OPO) described in Section 2.5.2 was utilized. This system delivered 43 mJ at 486 nm with a pulse length and width of 8 ns and 0.2  $\text{cm}^{-1}$ , respectively. The 486 nm beam was frequency doubled and the frequency components were separated, the remaining 486 nm being utilized for the polarization spectroscopy scheme and the doubled beam at 243 nm being focused to a lasersheet intersecting the pump and probe beam, crossing at the centre of the measurement region, in this case a welding torch flame with a 1 mm diameter nozzle.

The cross-section of the lasersheet

and the probe and pump beam creates a disc-shaped probe volume 6 mm in diameter and about 100  $\mu\text{m}$  thick, the thickness being determined by the waist of the 243 nm lasersheet. The PS-scheme utilized a co-propagating setup using a circularly polarized pump beam. The signal beam was spatially filtered after having passed through the analyzer before being detected by an ICCD camera (Princeton 576S/RB-T, described in Section 2.5.3).

Very little background interference was evident and the signal was roughly two orders of magnitude stronger than the background. Several possible disturbances can arise in obtaining measurements of this sort in which use is made of strong UV-radiation. Effects due to saturation or to photo-ionization from the excited state of hydrogen, or to the photochemical production of atomic hydrogen and of hydroxyl are all possible. Investigations of photo-chemical effects during the multiphoton excitation of atomic hydrogen were carried out by Goldsmith [119], the laser energy in the present work is approximately a factor of two lower than the power limits that were stated.

Results of the 2D-measurements of atomic hydrogen obtained are shown in Fig. 4.7, where the high signal-to-background ratio which is found should be noted. A strong, localized signal from atomic hydrogen, close to the reaction zone, is also evident.

### 4.3.3 Infrared polarization spectroscopy of combustion related species

There are several combustion related species which are not accessible in the UV/visible spectral regime, such as  $\text{CO}_2$ ,  $\text{CH}_4$ ,  $\text{C}_2\text{H}_2$  and  $\text{CH}_3$ . However, most molecules possess vibrational transitions in the mid-IR spectral regime, which makes this spectral regime highly attractive. There have been various difficulties involved in carrying out measurements in this spectral regime, such as the detectors available being expensive and insensitive, and the limited availability of high power laser sources, this resulting in low spatial resolution, low signal levels and difficulties connected with interference stemming from high background radiation. In recent years, technical advances have alleviated some of these difficulties. Various technical specifications and remarks pertaining to this can be found in Chapter 2.

Infrared laser-induced fluorescence, IRLIF, is an attractive technique. Several investigations regarding it have been carried out recently [35,120-123]. In reactive flows, however, the background is an obvious issue. Also, LIF has the inherent problem of quenching, making adequate quantitative measurements by it very difficult, a problem even more serious for IRLIF, due to its weaker transition probabilities in the IR-spectral regime. Another alternative approach, which is developing rapidly due to advances in laser technology is absorption measurements for determining both concentration and temperature [124,125]. Such measurements can be conducted in a variety of ways, although the basic physics stays the same in each case. A major drawback to such an approach is the fact that

absorption measurements are always line-of-sight measurements which provide a kind of integrated quantity over the entire beam path, and lack the spatial precision of IRLIF. Infrared polarization spectroscopy, IRPS, was not introduced until 2002, when Roy et al. published their findings on carbon dioxide [112]. Due to the excitation scheme employed that work suffered from a low signal-to-noise ratio. IRPS have high spatial as well as spectral resolution, however, and shows very effective suppression of the thermal background. In the present work, several species important to combustion including  $\text{CO}_2$ ,  $\text{CH}_4$ ,  $\text{C}_2\text{H}_2$ ,  $\text{C}_2\text{H}_4$ ,  $\text{CH}_3$  and  $\text{H}_2\text{O}$ , were investigated in this way. A brief summary of the fairly extensive work in this area that has been conducted will be provided here. More detailed information concerning it is provided in Papers VII, VIII, IX, and Papers XI, X, XII.

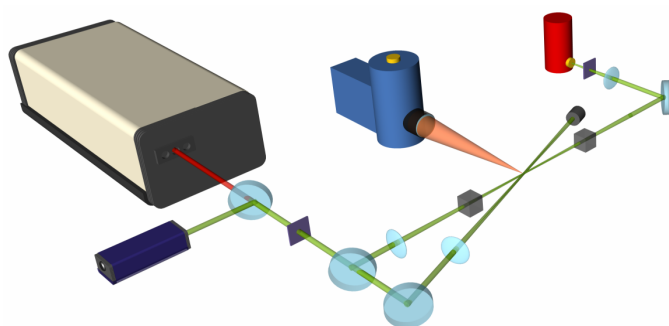


*Figure 4.8 Schematic view of the IRPS setup in which IRLIF being collected by an IR-camera at a  $90^\circ$  angle to the crossing of the beams, the IRPS signal is acquired by an InSb detector (red). Note that an alignment laser overlaps the IR-beam to enable it to be visualized.*

The experimental setup for obtaining IRPS measurements is in many ways very similar to a PS-setup in the UV/visible spectral range, despite certain exceptions. For one thing, while the IR laser beam is invisible, a He-Ne laser overlaps the IR-beam so as to simplify the alignment, allowing the path of the IR-beam to be visualized. Another difference is that other optical materials are needed, since BK7 and fused silica, for example, have little or no transmission in the mid-IR spectral regime. Accordingly, as mentioned in Chapter 2,  $\text{CaF}_2$  is used for beam splitters and lenses, whereas  $\text{YVO}_4$  is used for the polarizers. The specific setups involved are discussed in the papers in question, their not being presented here, although their general characteristics are depicted in Fig. 4.8.

The IRPS measurements reported in this work were performed using the Sirah dye laser system pumped by the QuantaRay, and the frequency conversion extension described in Chapter 2, with the exception of the CO<sub>2</sub> lineshape measurements described in Paper VII, in which an alexandrite laser system and a Raman shifter were used to produce a 2 μm beam. This setup is described in greater detail in Paper VII, B, C and the laser in question in Section 2.4.

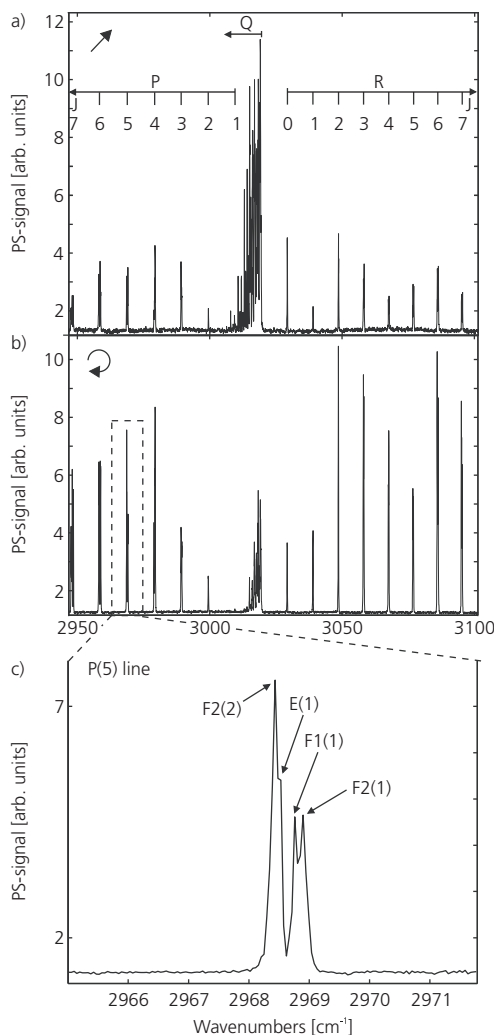


**Figure 4.9** IRPS spectra of the  $\nu_3$  band of  $\text{CH}_4$  obtained through a) use of a linear pump, b) use of a circular pump, and c) expanding of the P(5) line so as to visualize the symmetric fine structures.

The IRPS measurements reported in the thesis were being conducted both in non-reacting and in reacting flows. The characterizing of such stable species as CO<sub>2</sub>, CH<sub>4</sub>, C<sub>2</sub>H<sub>2</sub> and C<sub>2</sub>H<sub>4</sub> in non-reacting flows with different colliding partners can facilitate measurements at elevated temperatures and in more complicated environments and contribute to an understanding of the results. In flow measurements of this type made at atmospheric pressure, the typical detection limits are around 30-100 ppm, the value in question depending upon the species. Signal-to-noise ratios higher than  $10^4$  have been reported. A methane spectrum (Paper VIII) in a cold flow (containing 2 % of methane and 98 % of Ar), acquired by use of a linearly- and circularly polarized pump beam and averaged over 10 laser shots for each data point, is shown in Fig. 4.9. The high signal-to-noise ratio, despite the laser energy being quite low ( $\sim 0.5$  mJ), and the high spectral resolution attained, which resolves the symmetric fine structure of CH<sub>4</sub>, can be clearly seen.

These measurements of the flow of small hydrocarbons were later extended in Paper IX to include ethane, enabling possibilities for multi-species detection to be investigated. The lines were all

successfully assigned. The possibility shown in Fig. 4.10 of enhancing either the  $Q$ -branch or the  $R$ - and  $P$ -branch can be helpful. Simultaneous IRPS and IRLIF measurements were also conducted in the same study, providing the opportunity to compare the two techniques in the mid-IR regime directly. IRPS was found to be superior both in detection sensitivity and in background discrimination. The IR-camera described in Section 2.5.4 was used for detection in the case of IRLIF.

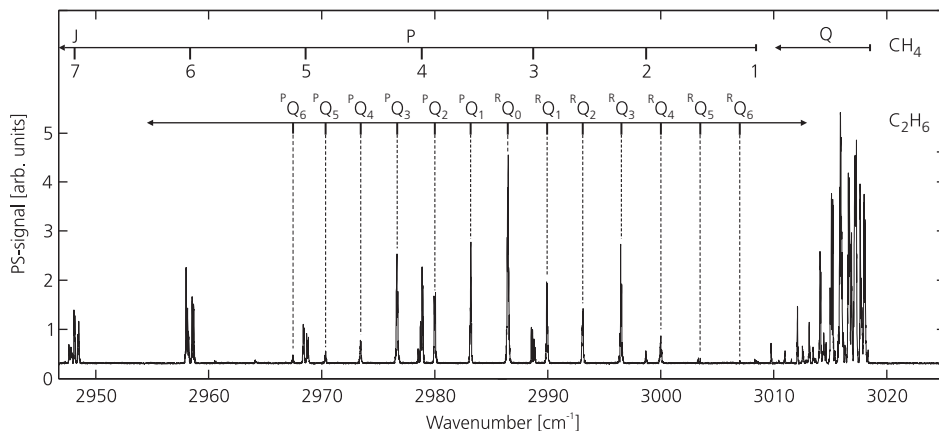


**Figure 4.10** The IRPS excitation spectrum of a gas mixture consisting of methane and ethane at ambient pressure and temperature.

Studies of acetylene, both at atmospheric pressure and at low pressure under well controlled conditions were reported in Paper X. This was done to investigate the pressure and collider dependence of the IRPS signal. It was found that the decay constant for the different colliders were similar, i.e. they had similar quenching rates. This indicates the possibility of employing IRPS in complex environments. The dependence of the IRPS signal on the collider concentration was also investigated. A quadratic dependence was shown, as had been predicted by the phenomenological equation (4.10).

Since the detection of acetylene, as well as of the other molecules discussed above, is of primary interest here when carried out under flame conditions, several flame studies were performed. The abundance of methane was investigated as a function of height above a McKenna burner. Methane was found to be consumed in the reaction zone in a  $\sim 0.5$  mm thick layer. A strong spectrum could be collected, however, even at locations much higher up in the flame. The lines in question have not been assigned, which points to a substantial problem in working at elevated temperatures, namely the lack of reliable high-temperature line-data.

Another task of interest is to measure nascent species in a flame. In the study reported in Paper XI the combustion products  $\text{H}_2\text{O}$  and  $\text{CO}_2$  were probed at  $2.7\ \mu\text{m}$ , both hot water and  $\text{CO}_2$  lines being identified. For the hot water lines, a  $\text{H}_2/\text{air}$  flame was used to minimize interference by other species and to be able to find a window in the water lines in which  $\text{CO}_2$  could be detected. Again, the selectivity of polarization spectroscopy was very useful in its simplifying the spectrum and suppressing unwanted  $P$ -branch water lines in investigating  $\text{CO}_2$ .

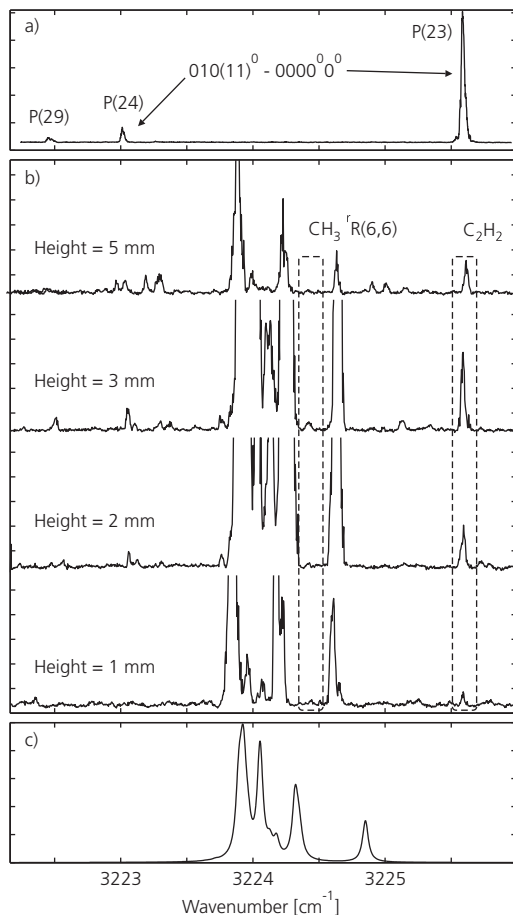


**Figure 4.11** IRPS acetylene spectra in a slightly rich 50 mbar methane/oxygen flame; a) excitation scan of the P(24) and P(23) line of the  $(010(11)^0 - (0000(0)^0)$  band of acetylene in a gas flow; b) excitation scans at different heights above the burner, acetylene, methane and ethyl being visible; c) calculated IRPS spectrum of hot methane.

Nascent  $\text{C}_2\text{H}_2$  was probed in a low pressure (50 mbar),  $\text{CH}_4/\text{O}_2$  flat flame in Paper X. The cold-flow measurements that were presented in the same paper facilitated recognition of the  $\text{C}_2\text{H}_2$  in the spectrum. The measurements were conducted at different heights above the flame. They clearly showed the concentration of acetylene to vary with height above the burner, as expected. This, together with a very weak  $\text{CH}_3$  signal, can be seen in Fig. 4.11.

Hot water is always present in the combustion of hydrocarbon fuel. It has a complicated spectrum, with large numbers of lines in the mid-infrared regime. These lines can interfere with signals from minor species. To analyze possibilities for measuring the minor species satisfactorily in this “forest” of water lines, a study was conducted to measure the occurrence of the hydroxyl radical

in the presence of waterlines. The OH-lines could be identified successfully and be simulated, together with the waterlines in this region. It was evident that the data available in HITRAN and HITEMP [126] are not accurate in terms of line

positions. On the basis of the measurements referred to above, however, it can be stated that mid-IRPS has considerable potential for obtaining experimental data in combustion environments, especially for detailed investigations of flame chemistry.

# Chapter 5

## Laser-induced fluorescence (LIF)

Achieving an adequate understanding of turbulent combustion phenomena often requires obtaining two-dimensional information. Laser-induced fluorescence (LIF), a highly sensitive resonant technique, can readily be employed for studying the distributions of minor species, down to sub-ppm levels, both qualitatively and quantitatively, and for measuring temperature fields and flame front propagation. At present LIF is one of the most widely utilized laser diagnostic techniques in the combustion area. In this chapter a brief account of laser-induced fluorescence will be provided and its application to measure minor species present in turbulent combustion discussed.

### 5.1 A basic account of laser-induced fluorescence

Laser-induced fluorescence is a resonant technique. Thus, the wavelength is chosen to match the transition of a target species, usually from one electronic state to another but sometimes of one rotational-vibrational level to another. The target species is excited by a laser, the light which is emitted on the basis of the de-excitation process being termed fluorescence. Although the fluorescence produced may be resonant, so that the target emits the same wavelength as that which was absorbed, the rotational and vibrational levels in the ground state that are accessible can also differ, depending on the structure of the molecules and the selection rules that apply, leading to the wavelengths emitted being slightly different (usually longer) than those of the excitation source, as shown in Fig. 5.1. This wavelength shift makes the detection of the signal technically simpler, than in Rayleigh scattering, which was discussed in Chapter 3. Interference or colour glass filters can be used to suppress the irradiating laser light. The absorbed and the emitted energies are unique to the target species in question, which can be chosen selectively, identified and information concerning both temperature and concentration extracted from them. Different approaches to extracting this information, for combustion diagnostic purposes, are taken up by Eckbreth [4] and by Daily [127]. In a simplified two-level system in which fluorescence is involved,

the intensity of the fluorescence,  $I_{fl}$ , is proportional to the number density in the excited state  $N_2$ , in accordance with

$$I_{fl} = A_{21} h \nu_{21} \frac{\Omega}{4\pi} V N_2 \quad (5.1)$$

where  $A_{21}$  is the Einstein coefficient for spontaneous emission,  $h$  is the Planck constant,  $\nu_{21}$  is the frequency of the emitted radiation,  $\Omega$  is the detection solid angle and  $V$  is the observation volume.

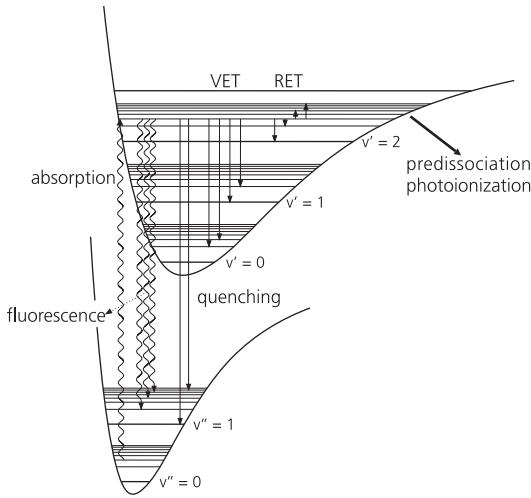


*Figure 5.1 Schematic diagram showing energy transfer processes in a typical radical.*

Unfortunately, just as with most diagnostic techniques in this area, LIF has certain inherent difficulties. The long lifetime of the fluorescence (typically on the order of tens of or even hundreds of nanoseconds) makes the signal very sensitive to collisions (typical collision times under atmospheric conditions are  $\sim 100$  ps), which compete with the signal-generating process. This process termed quenching, and denoted  $Q_{21}$ , is what makes quantitative LIF difficult to obtain. Even at 1 bar, the quenching rate for most radicals relevant to combustion is 2-4 times the rate of spontaneous emission of a fluorescence

photon [128]. At elevated pressures, the collision times are diminished and can be on the order of only a few picoseconds.

In the linear regime of laser-induced fluorescence, the upper state population is given by

$$N_2 = N_1^0 \frac{I_{laser}}{c} \frac{B_{12}}{A_{21} + Q_{21}} \quad (5.2)$$

where  $N_1^0$  is the lower state population,  $I_{laser}$  the irradiated laser intensity, and  $B_{12}$  the Einstein coefficient of stimulated absorption. Taking account both of (5.1) and (5.2) indicates the fluorescence intensity to be linearly dependent upon the lower-state population, the laser intensity and the  $B_{12}$  coefficient. The quenching term in the denominator is what makes quantitative LIF measurements difficult, especially because this term is dependent upon temperature, pressure, the collisional

environment, and the quantum numbers of the different states. All of these parameters are difficult to determine satisfactorily at any given moment in a specific measurement situation.

Unless used wisely, LIF is also sensitive to both photoionization and predissociation, which means that an excited molecule can become ionized or dissociate prior to emitting a photon. When LIF is used carefully, however, photoionization and predissociation may both be negligible. Fig. 5.1 shows schematically the different processes involved in LIF. Two of these, rotational energy transfer (RET) and vibrational energy transfer (VET), can result in extra spectral lines in the spectrum through the collisions that occur.

There are a number of different approaches in dealing with quenching, involving either avoiding it entirely or measuring it. In predissociative LIF and ionization LIF, for example, loss terms can be increased to the point of making quenching negligible, but weakening the fluorescence signal dramatically. Saturated LIF, an approach in which a strong excitation laser is employed is strongly affected by the energy transfer in the ground state, leaving the fluorescence signal largely independent of both quenching and laser irradiance. Use of short excitation pulses, such that the pulse duration is shorter than collision times typically are, is a further option, one that enables quenching-free measurements to be performed, yet the short pulses involved can introduce other problems, such as limited spectral resolution, through the linewidth of the laser being related to the pulse duration. The shorter the duration is, the broader the spectral profile becomes.

## 5.2 Laser-induced fluorescence for CH detection

There are many intermediate species that are important in combustion research. The spectrum of one of these, CH, was first studied in Lund by Heurlinger in 1918 [129]. It took until the 1960s, however, due to its low concentration, before Gaydon et al. [130] could detect it in a low-pressure acetylene/oxygen flame through use of absorption spectroscopy. Porter et al. [131], were later able, through use of the same technique, to make point measurements in acetylene and methane/air flames and to map concentration profiles point-wise. They found CH to be confined to a very narrow region in the high-temperature reaction zone.

Somewhat more than a decade later, the first laser-induced fluorescence measurements of CH in atmospheric flames were performed [132]. In this work, CH was excited at 427.3 nm corresponding to the  $X^2\Pi \rightarrow A^2\Delta (0,0), K''=6 \rightarrow K'=7$  transition in the *R*-branch of CH. The first imaging work was conducted by Allen et al. [133] in the mid 80s when technical advances in lasers and detectors made this possible, their being able, through probing the *R*(5) line of the A-X system mentioned above, to obtain single-shot distributions in a premixed ethylene/air flame.

Another excitation scheme that has been employed is the  $X^2\Pi \rightarrow A^2\Delta$  (0,1) transition at  $\sim 387$  nm, first examined in [134], the combined fluorescence from the diagonal (1,1) and (0,0) bands being detected there at 431 nm. Due to the low transition probabilities [135] and electronic energy transfer from the A(1) to the B(0) state, the fluorescence signal that was detected was relatively weak, however. An additional possibility is the  $C^2\Sigma^+ \rightarrow X^2\Pi$  transition, which, according to Hirano et al. [136], is highly predissociative and is thus unsuitable for sensitive CH detection.

A successful excitation scheme used quite frequently for flame structure studies in both turbulent premixed flames [137-139] and non-premixed flames [140-143] during the last few years, is that of the excitation of the  $B^2\Sigma^- \rightarrow X^2\Pi$  (0,0) band followed by the detection of fluorescence from the B-X (0,1) and the A-X bands.

In the work presented in Paper XIII, excitation was carried out at  $\sim 387.3$  nm in the R-branch of the (0,0) band of the B-X system. The fluorescence was collected at around 431 nm from the B-X (0,1), A-X (1,1) and A-X (0,0) bands. The population in the A band originated from electronic energy transfer from the B state. This wavelength shift made it easy to separate the elastic scattering at the laser wavelength from the fluorescence through use of a colour glass filter (GG-400).

The laser used in the present work was an alexandrite laser (described in Section 2.4) characterized by a long pulse duration ( $\sim 150$  ns) and a pulse energy of  $\sim 200$  mJ. Its pulse energy is increased by a factor of almost two by a flash lamp pumped amplifier and its frequency is doubled so as to obtain the desired wavelength of 387.3 nm. The laser has the possibility of being run either in single- or multi-mode with a linewidth of 100 MHz or  $8\text{ cm}^{-1}$ , respectively. The narrow linewidth option was used to determine the line positions in the CH spectrum.

The simultaneous recording of LIF from iodine, excited by the first anti-Stokes component of hydrogen gas at 585 nm, helped in determining the line positions and enabled an absolute frequency scale to be employed. The experimental setup is shown in Fig. 5.2.

Most of the measurements were made using the multi-mode option, which enables 7 rotational lines to be excited simultaneously. This, together with the long pulse duration and the high peak power, increased the sensitivity of CH detection. The long pulse duration enabled the same molecule to be excited several times

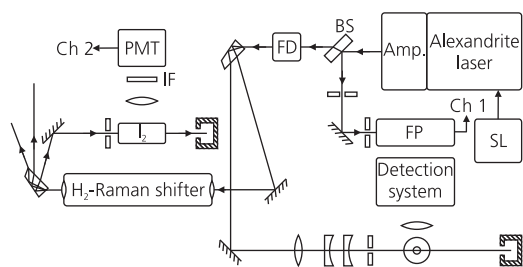


**Figure 5.2** Schematic view of the experimental setup: BS, beamsplitter; SL, seeding laser; FP, Fabry-Perot etalon; IF, interference filter; FD, frequency doubling; PMT, photo-multiplier tube; Ch 1 and Ch 2, input channels to the oscilloscope.

during a given pulse, since the lifetime in the excited state is in the order of 1 ns. The pulse energy at 387.3 nm was  $\sim 70$  mJ, which is to be compared with  $\sim 20$  mJ for a conventional Nd:YAG pumped dye system. Taking all of this into account, the sensitivity can be estimated as being two orders of magnitude higher than for a conventional Nd:YAG pumped dye-laser system. This enables two-dimensional measurements to be performed within a wide range of stoichiometries, from  $\Phi = 0.6$  to  $\Phi = 2$ , with high signal-to-noise ratios. The signal peaks at  $\Phi \sim 1.3$ .

This was demonstrated by single shot imaging at a high spatial resolution in a lean and highly turbulent methane/air jet flame, as shown in Fig. 5.3. The co-axial burner is described in Section 2.7.1. The work was continued, simultaneous OH/CH measurements performed using the scheme mentioned above, being presented in Paper D.

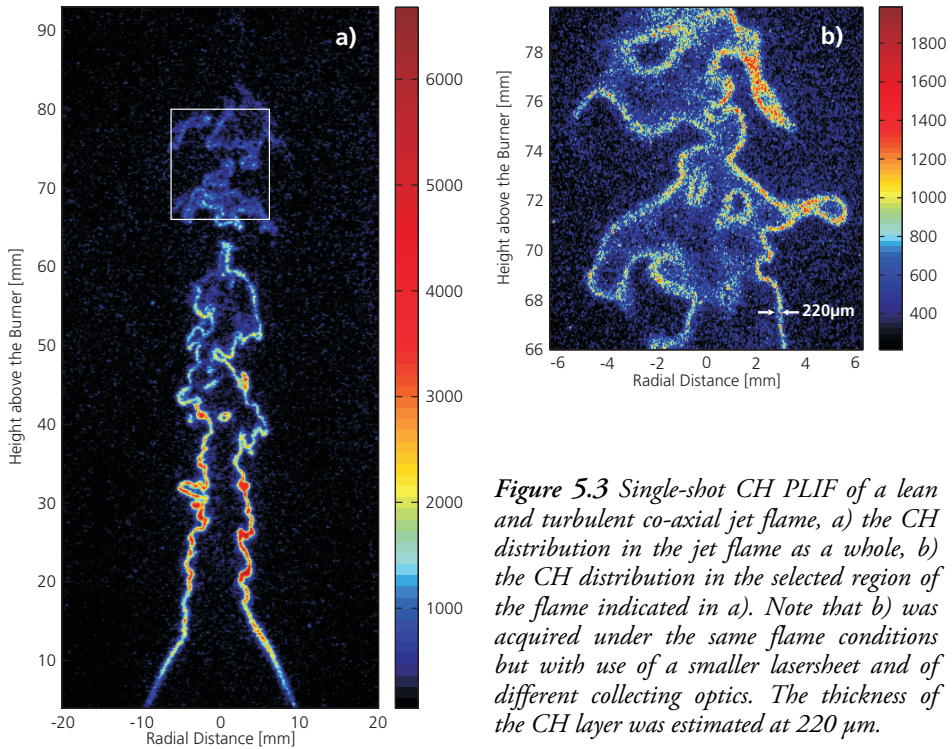


*Figure 5.3 Single-shot CH PLIF of a lean and turbulent co-axial jet flame, a) the CH distribution in the jet flame as a whole, b) the CH distribution in the selected region of the flame indicated in a). Note that b) was acquired under the same flame conditions but with use of a smaller lasersheet and of different collecting optics. The thickness of the CH layer was estimated at  $220 \mu\text{m}$ .*

### 5.3 Mid-infrared laser-induced fluorescence (IRLIF)

There are several molecular species that for different reasons are not readily accessible in the UV/visible spectral range. Several of these have IR-active ro-vibrational transitions that can be excited in the mid-IR range. Small hydrocarbons ( $C_1$ - $C_3$ ) also have special spectral features in the IR spectral regime, creating the possibility of their being identified there on this basis. This makes investigation of laser-induced fluorescence in the mid-infrared spectral regime of particular interest as such, although to date only few studies aimed at exploiting this have been made, mainly due to the lack of effective detectors or suitable laser sources. These technical problems have been addressed during the last years, however, and better laser sources and more sensitive detectors having become available. This has sparked a number of publications in this area by Hanson and co-workers [35,120-123]. In the present work, several investigations of the feasibility of applying IRLIF to combustion have also been conducted.

An investigation of  $CO_2$  at 2  $\mu m$  with use of IRPS is described briefly in Papers VII, B and C, IRLIF measurements were also obtained there, various comparisons being made with the lineshapes obtained by IRPS, and the dependence upon collisions in the two cases. The alexandrite laser described in Section 2.4, was utilized in this work, the laser being Raman-shifted in order to achieve the desired wavelength through use of the 2<sup>nd</sup> Stokes. A single-shot image of a  $CO_2$  flow in open air is shown in Fig. 2.9, the IR-camera from Santa Barbara Focalplane (described in Section 2.5.4) being used to obtain it. The transition that was probed,  $(00^0) \rightarrow (12^0)$ , was too weak, however, for IRLIF to be performed in a realistic case, with all the background emissions this could be expected to involve. Accordingly, the Nd:YAG-pumped dye laser system outfitted with a frequency extension unit (described in Section 2.3) was selected later for probing the  $(00^0) \rightarrow (10^0)$  transition at 2.7  $\mu m$ . This transition was approximately 45 times stronger than the one just referred to, yielding the signal increase that was needed. In both cases the fluorescence signal was detected at 4.3  $\mu m$ .

An excitation scan with 2.7  $\mu m$  laser excitation of  $CO_2$  is shown in Fig. 5.4, a) is the acquired spectrum and b) a simulation using parameters from the HITRAN database [126]. The measured line positions and strengths correspond well to the simulated spectrum. The evident discrepancies are due to water line absorption in the ambient air as the IR-beam passes through it.

Cell measurements under elevated pressure conditions showed the IRLIF signal from  $CO_2$  to drop and become undetectable when the pressure reached  $\sim 10$  bar, a limitation due mainly to absorption and to collisional quenching, suggesting that obtaining measurements under conditions of elevated pressures could be difficult to perform.

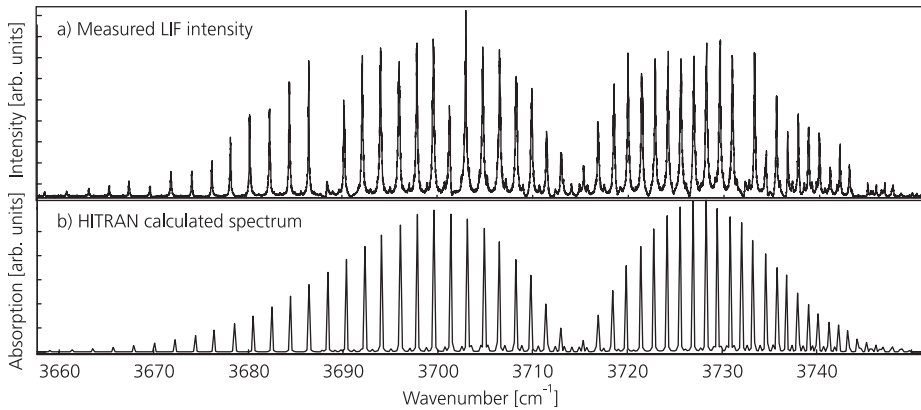


**Figure 5.4** LIF excitation-scan of the  $(00^0) \rightarrow (10^1)$  band by  $2.7 \mu\text{m}$  IR laser excitation. The spectrum was acquired in a gas jet at atmospheric pressure containing 5%  $\text{CO}_2$  diluted with Ar, a) being the measured spectrum and b) a simulation using parameters from the HITRAN database.

Two-dimensional measurements in cold  $\text{CO}_2/\text{Ar}$  jets were also performed at ambient air of varying  $\text{CO}_2$  concentration, see Fig. 5.5. The signal-to-background ratios obtained give promise of future measurements for gas phase diagnostics in cold flows succeeding well. As can be seen in Fig. 5.5 a), the signal strength is sufficiently strong, even at  $\text{CO}_2$  concentrations as low as 0.26% and at 1 mJ in an  $\sim 10$  mm high lasersheet.

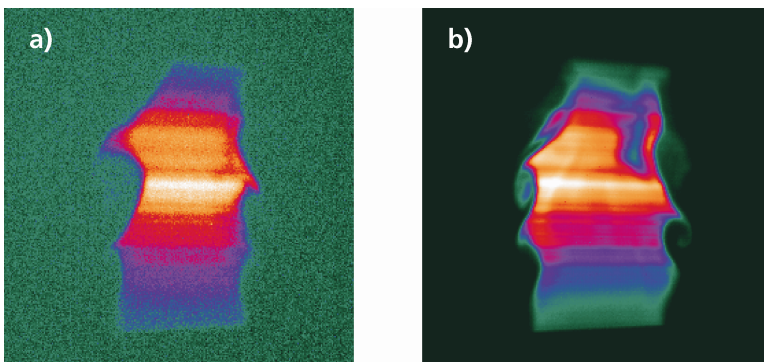


**Figure 5.5** Single-shot LIF images of  $\text{CO}_2$  in free gas jets of 1 mJ per pulse at  $2.7 \mu\text{m}$ . a) 0.26%  $\text{CO}_2$  in Ar, signal - background = 69 counts; b) 4.50%  $\text{CO}_2$  in Ar, signal - background = 810 counts.

The overall impression one gains from the results is that quantification of the IRLIF signal will be a challenging task, due to the complex collision dynamics and energy-transfer processes involved, at the same time as IRLIF possesses considerable potential for sensitive instantaneous gas diagnostics in cold flows.

# Chapter 6

## Summary and outlook

The thesis dealt with the development of new detection schemes for laser combustion diagnostics. It took up three different topics: filtered Rayleigh scattering, polarization spectroscopy and laser-induced fluorescence. The various schemes differ considerably from each other, each having its pros and cons yet all of them contribute to an appreciable degree of achieving a better understanding of combustion-related phenomena.

An approach to filtered Rayleigh scattering (FRS) utilizing a single-longitudinal mode alexandrite laser, which is rare within the combustion community, was developed. The alexandrite laser was paired with an isotopically enhanced mercury filter. The laser itself, with its long pulse duration, high peak power and narrow linewidth, proved very useful. For FRS in the UV-spectral regime the system is able to deliver a maximum of 50 mJ at 253.7 nm, the absorption wavelength of the mercury filter. The aim was to be able to perform FRS measurements in the UV, since the cross-section scales as  $\sigma \propto \nu^4$ . The technique is able to perform measurements in environments unsuitable for conventional Rayleigh scattering. Its use was demonstrated in Paper I and II, and in applications taken up in Paper III and IV. Attempts were also made to measure fuel/air distributions in Diesel and HCCI engines. Although in Diesel engines there may be a possibility in the future of performing quantitative measurements, at present only qualitative information can be obtained, as discussed in Chapter 3. Measurements of the fuel/air ratio in HCCI combustion were also found to be difficult to obtain, due to the low fuel concentration, although measuring absolute temperature distributions with use of refined models was considered to be feasible.

A possible development of FRS is to change the species in the molecular filter, while a UV-laser beam sometimes can introduce interfering fluorescence and absorption that might be avoided if the wavelength is increased. Use of rubidium at 780 nm, which is still within reach with use of the alexandrite laser system, is regarded as a possible candidate. It involves a decrease in the signal due to the dependence on wavelength, but part of that signal decrease can be compensated as the laser energy is increased by at least a factor of ten at that wavelength.

Polarization spectroscopy (PS) was developed and utilized for minor species detection, both in the UV/visible spectral regime (Paper V, VI) and in the mid-infrared (Paper VII, VIII, IX, X, XI, XII). The high signal-to-background ratio of PS is not easily obtained by use of any other technique. In the present work the detection of the CH radical demonstrated the sub-Doppler capability of the approach and imaging of atomic hydrogen its capability of providing two-dimensional measurements. Most of the work in this area has been directed, however, at the mid-infrared spectral regime, since there are many combustion-related species that have no electronic transitions in the UV/visible spectral regime. In addition, the background may be suppressed to a sufficient extent in the PS measurements, something which is difficult in e.g. LIF.

In the present work the alexandrite laser system was used for high resolution PS directed both at CH and CO<sub>2</sub>, due to its advantages pointed out to possess. In the other IR-measurements a Nd:YAG pumped dye laser provided with a frequency conversion unit was utilized to probe IR-active molecules. The work began with the detection of small hydrocarbons in non-reacting flows and was continued in reacting flows. The aim was to develop the method so as to be able to study potential problems connected with interfering water lines and possibilities of detecting trace species such as CH<sub>3</sub> in flames. The work was successful, possibilities for measuring further radicals appearing to be just around the corner. The development of two-dimensional measurements utilizing IRPS is a next natural step. What is needed to make PS still more useful is a simplified model for performing quantitative measurements, both of species concentrations and for temperatures. An interesting approach is pico-second PS in which short pulses are utilized. Attempts in this direction have been made [110,111] but further investigation aimed at reducing collisional dependence could be of considerable interest. It would also be of interest to compare results of PS measurements with those of such probing techniques as mass-spectrometry.

Laser-induced fluorescence (LIF) is probably the most commonly used laser diagnostic technique. In the present work, the LIF signal was compared with the PS signal, both in the visible range (Paper V) and in the mid-IR-spectral range (Paper VII), although the emphasis here was on the use of LIF for CH detection in lean combustion. A new detection scheme, probing several lines simultaneously, was developed. This was made possible by the exploration again of the properties of the alexandrite laser. No effort has been done thus far to quantify the results, but the results have become important in collaboration with modelers and it is already an important tool in efforts to better understand turbulent reacting flows and can be expected to become more important in this area. Already, simultaneous measurements of CH and OH (Paper D) have been performed, and other measurements are on the way. This excitation scheme holds promise for other species as well. In the near future, single-shot HCO can be expected to appear [144].

# Bibliography

1. *NE.se*, Nationalencyklopedin: Malmö, 2000
2. IEA, *Key World Energy Statistics 2006*, International Energy Agency, 2006, Available at: <http://www.iea.org/statist/index.htm>
3. Kohse-Höinghaus, K., Barlow, R.S., Aldén, M., and Wolfrum, J., *Combustion at the focus: laser diagnostics and control*. Proceedings of the Combustion Institute, **30**:89-123, 2005
4. Eckbreth, A.C., *Laser diagnostics for combustion temperature and species*. 2nd ed. Combustion science and technology book series ; v. 3, Gordon and Breach Publishers: Amsterdam, The Netherlands, 1996
5. Seyfried, H., Särner, G., Omrane, A., Richter, M., Schmidt, H., and Aldén, M., *Optical diagnostics for characterization of a full-size fighter-jet afterburner*. in *Proceedings of the ASME Turbo Expo*, Reno, Nevada, USA: American Society of Mechanical Engineers, 2005
6. Olofsson, J., Seyfried, H., Richter, M., Aldén, M., Vressner, A., Hultqvist, A., Johansson, B., and Lombaert, K., *High-Speed LIF Imaging for Cycle-Resolved Formaldehyde Visualization in HCCI Combustion*. SAE Transactions, Journal of Engines, **114**:645-652, 2005
7. Brackmann, C., Nygren, J., Bai, X., Li, Z., Bladh, H., Axelsson, B., Denbratt, I., Koopmans, L., Bengtsson, P.-E., and Aldén, M., *Laser-induced fluorescence of formaldehyde in combustion using third harmonic Nd:YAG laser excitation*. Spectrochimica Acta Part A: Molecular and Biomolecular Spectroscopy, **59**:3347-3356, 2003
8. Svelto, O. and Hanna, D.C., *Principles of lasers*. 4th ed., Plenum Press: New York, 1998
9. Siegman, A.E., *Lasers*, University Science Books: Mill Valley, CA., 1986
10. Newport Corporation, *Quanta-Ray Pro Series Pulsed Nd:YAG Lasers*, 2007, Available at: <http://www.newport.com/store/product.aspx?id=368168&lang=1033>

11. Continuum, *Operation and Maintenance Manual NY80*, 81, 82, Continuum, Editor., Continuum: Santa Clara, 1990
12. Quantel, *Q-switched Nd:YAG laser, Brilliant B*, 2007, Available at: [http://www.quantel.fr/uk/fiche\\_produit.php?id\\_produit=3](http://www.quantel.fr/uk/fiche_produit.php?id_produit=3)
13. Sirah Laser- und Plasmatechnik GmbH, *Service Manual Sirah Pulsed Dye Laser*, 2003
14. Giordmai.Ja and Miller, R.C., *Tunable Coherent Parametric Oscillation in LiNbO<sub>3</sub> at Optical Frequencies*. Physical Review Letters, 14:973-, 1965
15. Zhou, J.X., Hou, X.D., Tsai, S.J.J., Yang, K.X., and Michel, R.G., *Characterization of a tunable optical parametric oscillator laser system for multielement flame laser excited atomic fluorescence spectrometry of cobalt, copper, lead, manganese, and thallium in buffalo river sediment*. Analytical Chemistry, 69:490-499, 1997
16. Zhou, J.X., Hou, X.D., Yang, K.X., Tsai, S.J., and Michel, R.G., *Lasers based on optical parametric devices: Wavelength tunability empowers laser-based techniques in the UV, visible, and near-IR*. Applied Spectroscopy, 52:176A-189A, 1998
17. Sirah Laser- und Plasmatechnik GmbH, *Infra-Red Generation*, Available at: [http://www.sirah.com/PDF/InfraRed\\_Web.pdf](http://www.sirah.com/PDF/InfraRed_Web.pdf)
18. Sirah Laser- und Plasmatechnik GmbH, *Infra-Red Amplification*, Available at: <http://www.sirah.com/PDF/OPANIR.pdf>
19. Kagami, S., Asahina, A., Watanabe, R., Mimura, Y., Shirai, A., Hattori, N., Watanabe, T., and Tamaki, K., *Treatment of 153 Japanese patients with Q-switched alexandrite laser*. Lasers in Medical Science, 22:159-163, 2007
20. Wulfmeyer, V., Bosenberg, J., Lehmann, S., and Senff, C., *Injection-Seeded Alexandrite Ring Laser - Performance and Application in a Water-Vapor Differential Absorption Lidar*. Optics Letters, 20:638-640, 1995
21. Wulfmeyer, V., *Ground-based differential absorption lidar for water-vapor and temperature profiling: development and specifications of a high-performance laser transmitter*. Applied Optics, 37:3804-3824, 1998
22. Wulfmeyer, V. and Bosenberg, J., *Single-mode operation of an injection-seeded alexandrite ring laser for application in water-vapor and temperature differential absorption lidar*. Optics Letters, 21:1150-1152, 1996

23. Bakule, P., Baird, P.E.G., Boshier, M.G., Cornish, S.L., Heller, D.F., Jungmann, K., Lane, I.C., Meyer, V., Sandars, P.H.G., Toner, W.T., Towrie, M., and Walling, J.C., *A chirp-compensated, injection-seeded alexandrite laser*. Applied Physics B-Lasers and Optics, 71:11-17, 2000
24. Walling, J.C., Jenssen, H.P., Morris, R.C., Odell, E.W., and Peterson, O.G., *Tunable-Laser Performance in BeAl<sub>2</sub>O<sub>4</sub>-Cr<sup>3+</sup>*. Optics Letters, 4:182-183, 1979
25. Walling, J.C. and Peterson, O.G., *High-Gain Laser Performance in Alexandrite*. Ieee Journal of Quantum Electronics, 16:119-120, 1980
26. Walling, J.C., Peterson, O.G., Jenssen, H.P., Morris, R.C., and Odell, E.W., *Tunable Alexandrite Lasers*. IEEE Journal of Quantum Electronics, 16:1302-1315, 1980
27. Walling, J.C., Heller, D.F., Samelson, H., Harter, D.J., Pete, J.A., and Morris, R.C., *Tunable Alexandrite Lasers - Development and Performance*. IEEE Journal of Quantum Electronics, 21:1568-1581, 1985
28. Svanberg, S., *Atomic and molecular spectroscopy: basic aspects and practical applications*. 4th, rev. ed. Advanced texts in physics, Springer: Berlin ; New York, 2004
29. Hamamtsu Photonics K.K., *Photomultiplier tubes - Basics and applications*, 2006, Available at: [http://sales.hamamatsu.com/assets/applications/ETD/pmt\\_handbook\\_complete.pdf](http://sales.hamamatsu.com/assets/applications/ETD/pmt_handbook_complete.pdf)
30. Princeton Instruments inc., *Operation manual for: Model ST-130/135 Detector Controller Manual*, 1992
31. Princeton Instruments inc., *Selecting the Right ICCD Camera*, 2007, Available at: <http://www.roperscientific.de/datasheets/select%20iccd%20camera%20tech%20note%20revised2.pdf>
32. Schrader, C., *Untersuchungen von Hochfrequenzentladungen an mikrostrukturierten Elektrodensystemen (MSE) zur Oberflächenmodifikation*, Fakultät für Lebenswissenschaften, Technischen Universität Carolo-Wilhelmina: Braunschweig, 2006
33. Judson Technologies, *Indium Antimonide Detectors*, 2003, Available at: <http://www.judsontechnologies.com/indiumAnt.htm>

34. Santa Barbara Focalplane, *SBF-134 Operation Manual*, 2002
35. Kirby, B.J., *Infrared planar laser-induced fluorescence imaging and applications to imaging of carbon monoxide and carbon dioxide*, Report # TSD-140, Department of Mechanical Engineering, Stanford University: Palo Alto, 2001
36. CVI Laser, *Optical Components and Assemblies*, 2007, Available at: <http://www.cvilaser.com/PublicPages/Pages/default.aspx>
37. FOCTek Photonics Inc., *Polarizer*, 2007, Available at: [http://www.foctek.com/products/optics/P\\_Pola.htm](http://www.foctek.com/products/optics/P_Pola.htm)
38. Lee, T.W. and Mitrovic, A., *Structure of lean turbulent partially-premixed flames stabilized in a co-axial jet flame burner*. Combustion Science and Technology, 127:231-249, 1997
39. Lee, T.W. and Mitrovic, A., *Highly turbulent premixed flames stabilized in a co-axial jet flame burner*. Proceedings of the Combustion Institute, 26:455-460, 1996
40. Chan, C.K., Lau, K.S., Chin, W.K., and Cheng, R.K., *Freely propagating open premixed turbulent flames stabilized by swirl*. Proceedings of the Combustion Institute, 24:511-518, 1992
41. Cheng, R.K., Yegian, D.T., Miyasato, M.M., Samuelsen, C.E., Benson, C.E., Pellizzari, R., and Loftus, P., *Scaling and development of low swirl burners for low-emission furnaces and boilers*. Proceedings of the Combustion Institute, 28:1305-1313, 2000
42. Johnson, M.R., Littlejohn, D., Nazeer, W.A., Smith, K.O., and Cheng, R.K., *A comparison of the flowfields and emissions of high-swirl injectors and low-swirl injectors for lean premixed gas turbines*. Proceedings of the Combustion Institute, 30:2867-2874, 2005
43. Wolfhard, H.G. and Parker, W.G., *A New Technique for the Spectroscopic Examination of Flames at Normal Pressures*. Proceedings of the Physical Society of London Section A, 62:722-8, 1949
44. Smyth, K.C., Miller, J.H., Dorfman, R.C., Mallard, W.G., and Santoro, R.J., *Soot Inception in a Methane Air Diffusion Flame as Characterized by Detailed Species Profiles*. Combustion and Flame, 62:157-181, 1985

45. Vestin, F., Afzelius, M., and Bengtsson, P.-E., *Development of rotational CARS for combustion diagnostics using a polarization approach*. Proceedings of the Combustion Institute, **31**:833-840, 2007
46. Beyrau, F., Datta, A., Seeger, T., and Leipertz, A., *Dual-pump CARS for the simultaneous detection of  $N_2$ ,  $O_2$  and  $CO$  in  $CH_4$  flames*. Journal of Raman Spectroscopy, **33**:919-924, 2002
47. Walewski, J., Kaminski, C.F., Hanna, S.F., and Lucht, R.P., *Dependence of partially saturated polarization spectroscopy signals on pump intensity and collision rate*. Physical Review A, **64**:063816, 2001
48. Kaminski, C.F., Engström, J., and Aldén, M., *Quasi-instantaneous two-dimensional temperature measurements in a spark ignition engine using 2-line atomic fluorescence*. Proceedings of the Combustion Institute, **27**:1998
49. Fourchette, D.C., Zurn, R.M., and Long, M.B., *Two-Dimensional Rayleigh Thermometry in a Turbulent Nonpremixed Methane Hydrogen Flame*. Combustion Science and Technology, **44**:307-317, 1986
50. Miles, R. and Lempert, W., *2-Dimensional Measurement of Density, Velocity, and Temperature in Turbulent High-Speed Air-Flows by UV Rayleigh-Scattering*. Applied Physics B-Photophysics and Laser Chemistry, **51**:1-7, 1990
51. Miles, R.B., Forkey, J.N., and Lempert, W.R., *Filtered Rayleigh scattering measurements in supersonic/hypersonic facilities* AIAA Pap. 1992-3894, 1992
52. Hoffman, D. and Leipertz, A., *Temperature field measurements in a sooting flame by filtered Rayleigh scattering (FRS)*. Proceedings of the Combustion Institute, **26**:945-950, 1996
53. Hoffman, D., Munch, K.U., and Leipertz, A., *Two-dimensional temperature determination in sooting flames by filtered Rayleigh scattering*. Optics Letters, **21**:525-527, 1996
54. Elliott, G.S., Samimy, M., and Arnette, S.A., *Study of Compressible Mixing Layers Using Filtered Rayleigh-Scattering Based Visualizations*. AIAA Journal, **30**:2567-2569, 1992
55. Reeder, M.F., Samimy, M., and Elliott, G.S., *Investigation of the effect of tabs on supersonic jets using advanced diagnostics*. Journal of Propulsion and Power, **12**:742-751, 1996

56. Elliott, G.S. and Samimy, M., *Rayleigh scattering technique for simultaneous measurements of velocity and thermodynamic properties*. AIAA Journal, **34**:2346-2352, 1996
57. Elliott, G.S. and Beutner, T.J., *Molecular filter based planar Doppler velocimetry*. Progress in Aerospace Sciences, **35**:799-845, 1999
58. Most, D. and Leipertz, A., *Simultaneous two-dimensional flow velocity and gas temperature measurements by use of a combined particle image velocimetry and filtered Rayleigh scattering technique*. Applied Optics, **40**:5379-5387, 2001
59. Elliott, G.S., Glumac, N., and Carter, C.D., *Molecular filtered Rayleigh scattering applied to combustion*. Measurement Science & Technology, **12**:452-466, 2001
60. Yalin, A.P. and Miles, R.B., *Ultraviolet filtered Rayleigh scattering temperature measurements with a mercury filter*. Optics Letters, **24**:590-592, 1999
61. Yalin, A.P. and Miles, R.B., *Temperature measurements by ultraviolet filtered Rayleigh scattering using a mercury filter*. Journal of Thermophysics and Heat Transfer, **14**:210-215, 2000
62. Finkelstein, N.D.M., *An ultraviolet source and spectral imaging filters for non-intrusive laser-based diagnostics, Source DAI-B 58/11*, Department of Mechanical Engineering, Princeton University: Princeton, N.J., 1998
63. Proffitt, C.R., Brage, T., Leckrone, D.S., Wahlgren, G.M., Brandt, J.C., Sansonetti, C.J., Reader, J., and Johansson, S.G., *Mercury in the HgMn stars  $\chi$ -Lupi and HR 7775*. Astrophysical Journal, **512**:942-960, 1999
64. Bitter, F., *Magnetic resonance in radiation or absorbing atoms*. Applied Optics, **1**:1-10, 1962
65. Douglas, T.B., Ball, A.F., and Ginnings, D.C., *Heat Capacity of Liquid Mercury between 0 °C and 450 °C - Calculation of Certain Thermodynamic Properties of the Saturated Liquid and Vapor*. Journal of Research of the National Bureau of Standards, **46**:334-348, 1951
66. Young, A.T., *Rayleigh-Scattering*. Applied Optics, **20**:533-535, 1981
67. She, C.Y., *Spectral structure of laser light scattering revisited: bandwidths of nonresonant scattering lidars*. Applied Optics, **40**:4875-4884, 2001
68. Boyd, R.W., *Nonlinear optics*. 2nd ed., Academic Press: San Diego, CA, 2003

69. Miles, R.B., Lempert, W.R., and Forkey, J.N., *Laser Rayleigh scattering*. Measurement Science & Technology, **12**:R33-R51, 2001
70. Forkey, J.N. and Princeton University. Dept. of Mechanical and Aerospace Engineering., *Development and demonstration of filtered Rayleigh Scattering : a laser based flow diagnostic for planar measurement of velocity, temperature and pressure*, Thesis Ph D --Princeton University 1996. 1996
71. Smith, P.L., Huber, M.C.E., and Parkinson, W.H., *Refractivities of H<sub>2</sub>, He, O<sub>2</sub>, CO, and Kr for 168 ≤ λ ≤ 288 nm*. Physical Review A, **13**:1422-1434, 1976
72. Landolt, H.H., Hellwege, K.-H., Hellwege, A.M., and Börnstein, R., *Zahlenwerte und Funktionen aus Physik, Chemie, Astronomie, Geophysik und Technik*. 6. Aufl. ed., Springer-Vlg: Berlin ; New York, 1962
73. Gaydon, A.G., *The spectroscopy of flames*. 2d ed., Chapman and Hall: London, 1974
74. Bideau-Mehu, A., Guern, Y., Abjean, R., and Johannin-Gilles, A., *Interferometric determination of the refractive index of carbon dioxide in the ultraviolet region*. Optics Communications, **9**:432-434, 1973
75. Griesmann, U. and Burnett, J.H., *Refractivity of nitrogen gas in the vacuum ultraviolet*. Optics Letters, **24**:1699-1701, 1999
76. Bates, D.R., *Rayleigh-Scattering by Air*. Planetary and Space Science, **32**:785-790, 1984
77. Vogel, A.I., *Physical Properties and Chemical Constitution .9. Aliphatic Hydrocarbons*. Journal of the Chemical Society, 133-139, 1946
78. Yip, S. and Neklin, M., *Application of Kinetic Model to Time-Dependent Density Correlations in Fluids*. Physical Review a-General Physics, **135**:1241-8, 1964
79. Tenti, G., Boley, C.D., and Desai, R.C., *Kinetic-Model Description of Rayleigh-Brillouin Scattering from Molecular Gases*. Canadian Journal of Physics, **52**:285-290, 1974
80. Boley, C.D., Tenti, G., and Desai, R.C., *Kinetic Models and Brillouin-Scattering in a Molecular Gas*. Canadian Journal of Physics, **50**:2158-8, 1972

81. Young, A.T. and Kattawar, G.W., *Rayleigh-Scattering Line-Profiles*. Applied Optics, **22**:3668-3670, 1983
82. Boguszko, M. and Elliott, G.S., *Property measurement utilizing atomic/molecular filter-based diagnostics*. Progress in Aerospace Sciences, **41**:93-142, 2005
83. Most, D., Dinkelacker, F., and Leipertz, A., *Direct determination of the turbulent flux by simultaneous application of filtered Rayleigh scattering thermometry and particle image velocimetry*. Proceedings of the Combustion Institute, **29**:2669-2677, 2003
84. Kearney, S.P., Schefer, R.W., Beresh, S.J., and Grasser, T.W., *Temperature imaging in nonpremixed flames by joint filtered Rayleigh and Raman scattering*. Applied Optics, **44**:1548-1558, 2005
85. K.C. Smyth, <http://www.bfrl.nist.gov> (1999)
86. Franke, A., *Characterization of an Electrical Sensor for Combustion Diagnostics*, Lund reports on combustion physics, Combustion Physics, Lund Institute of Technology, P.O. Box 118, SE-22100 Lund, Sweden: Lund, 2002
87. Espey, C., Dec, J.E., Litzinger, T.A., and Santavicca, D.A., *Planar laser Rayleigh scattering for quantitative vapor-fuel imaging in a diesel jet*. Combustion and Flame, **109**:65-86, 1997
88. Espey, C., Dec, J.E., Litzinger, T.A., and Santavicca, D.A., *Quantitative 2-D Fuel Vapor Concentration Imaging in a Firing D.I. Diesel Engine Using Planar Laser-Induced Rayleigh Scattering*. SAE Technical Papers, **940682**:1994
89. Zhao, F.Q., Taketomi, M., Nishida, K., and Hiroyasu, H., *Quantitative Imaging of the Fuel Concentration in a SI Engine With Laser Rayleigh Scattering*. SAE Technical Papers, **932641**:1993
90. Richter, M., Franke, A., Aldén, M., Hultqvist, A., and Johansson, B., *Optical Diagnostics Applied to a Naturally Aspirated Homogeneous Charge Compression Ignition Engine*. SAE Technical Papers, **1999-01-3649**:1999
91. Wieman, C. and Hänsch, T.W., *Doppler-Free Laser Polarization Spectroscopy*. Physical Review Letters, **36**:1170-1173, 1976
92. Mohr, P.J. and Taylor, B.N., *CODATA recommended values of the fundamental physical constants: 2002*. Reviews of Modern Physics, **77**:1-107, 2005

93. Teets, R.E., Kowalski, F.V., Hill, W.T., Carlson, N., and Hänsch, T.W., *Laser polarization spectroscopy*, San Diego, CA, USA: Soc. Photo-Optical Instrumentation Engrs, 1977
94. Demtröder, W., *Laser spectroscopy: basic concepts and instrumentation*. 3rd ed. Advanced texts in physics, Springer: Berlin ; New York, 2003
95. Tong, W.G. and Yeung, E.S., *Polarization Spectroscopy for Elemental Analysis at Trace Concentrations*. Analytical Chemistry, 57:70-73, 1985
96. Zizak, G., Lanauze, J., and Winefordner, J.D., *Cross-Beam Polarization in Flames with a Pulsed Dye-Laser*. Applied Optics, 25:3242-3246, 1986
97. Danzmann, K., Grutzmacher, K., and Wende, B., *Doppler-Free 2-Photon Polarization-Spectroscopic Measurement of the Stark-Broadened Profile of the Hydrogen  $L_{\alpha}$  Line in a Dense-Plasma*. Physical Review Letters, 57:2151-2153, 1986
98. Seidel, J., *Theory of 2-Photon Polarization Spectroscopy of Plasma-Broadened Hydrogen  $L_{\alpha}$  Line*. Physical Review Letters, 57:2154-2156, 1986
99. Nyholm, K., Maier, R., Aminoff, C.G., and Kaivola, M., *Detection of OH in flames by using polarization spectroscopy*. Appl. Opt., 32:919, 1993
100. Nyholm, K., Fritzon, R., and Alden, M., *2-Dimensional Imaging of OH in Flames by Use of Polarization Spectroscopy*. Optics Letters, 18:1672-1674, 1993
101. Nyholm, K., *Measurements of OH rotational temperatures in flames by using polarization spectroscopy*. Optics Communications, 111:66-70, 1994
102. Nyholm, K., Fritzon, R., and Alden, M., *Single-Pulse 2-Dimensional Temperature Imaging in Flames by Degenerate 4-Wave-Mixing and Polarization Spectroscopy*. Applied Physics B-Lasers and Optics, 59:37-43, 1994
103. Nyholm, K., Fritzon, R., Georgiev, N., and Aldén, M., *Two-photon induced polarization spectroscopy applied to the detection of  $NH_3$  and CO molecules in cold flows and flames*. Optics Communications, 114:76-82, 1995
104. Nyholm, K., Kaivola, M., and Aminoff, C.G., *Polarization Spectroscopy Applied to  $C_2$  Detection in a Flame*. Applied Physics B-Lasers and Optics, 60:5-10, 1995

105. Dreizler, A., Dreier, T., and Wolfrum, J., *Polarization spectroscopic measurement of the NH ( $A^3\Pi - X^3\Sigma$ ) transition in an ammonialoxygen flame.* Journal of Molecular Structure, **349**:285-288, 1995
106. Kaminski, C.F. and Dreier, T., *Investigation of two-photon-induced polarization spectroscopy of the  $a-X(1,0)$  transition in molecular nitrogen at elevated pressures.* Applied Optics, **39**:1042-1048, 2000
107. Reichardt, T.A. and Lucht, R.P., *Theoretical calculation of line shapes and saturation effects in polarization spectroscopy.* Journal of Chemical Physics, **109**:5830-5843, 1998
108. Giancola, W.C., Reichardt, T.A., and Lucht, R.P., *Multi-axial-mode laser effects in polarization spectroscopy.* Journal of the Optical Society of America B-Optical Physics, **17**:1781-1794, 2000
109. Reichardt, T.A., Giancola, W.C., and Lucht, R.P., *Experimental investigation of saturated polarization spectroscopy for quantitative concentration measurements.* Applied Optics, **39**:2002-2008, 2000
110. Reichardt, T.A., Di Teodoro, F., Farrow, R.L., Roy, S., and Lucht, R.P., *Collisional dependence of polarization spectroscopy with a picosecond laser.* Journal of Chemical Physics, **113**:2263-2269, 2000
111. Roy, S., Lucht, R.P., and Reichardt, T.A., *Polarization spectroscopy using short-pulse lasers: Theoretical analysis.* Journal of Chemical Physics, **116**:571-580, 2002
112. Roy, S., Lucht, R.P., and McIlroy, A., *Mid-infrared polarization spectroscopy of carbon dioxide.* Applied Physics B-Lasers and Optics, **75**:875-882, 2002
113. Aldén, M., Schawlow, A.L., Svanberg, S., Wendt, W., and Zhang, P.L., *3-Photon-Excited Fluorescence Detection of Atomic-Hydrogen in an Atmospheric-Pressure Flame.* Optics Letters, **9**:211-213, 1984
114. Lucht, R.P., Salmon, J.T., King, G.B., Sweeney, D.W., and Laurendeau, N.M., *2-Photon-Excited Fluorescence Measurement of Hydrogen-Atoms in Flames.* Optics Letters, **8**:365-367, 1983
115. Gasnot, L., Desgroux, P., Pauwels, J.F., and Sochet, L.R., *Improvement of two-photon laser induced fluorescence measurements of H- and O-atoms in premixed methanelair flames.* Applied Physics B-Lasers and Optics, **65**:639-646, 1997

116. Dux, R., Grutzmacher, K., Delarosa, M.I., and Wende, B., *Absolute Determination of Local Ground-State Densities of Atomic-Hydrogen in Nonlocal-Thermodynamic-Equilibrium Environments by 2-Photon Polarization Spectroscopy*. Physical Review E, **51**:1416-1427, 1995
117. Kulatilaka, W.D., Lucht, R.P., Hanna, S.F., and Katta, V.R., *Two-color, two-photon laser-induced polarization spectroscopy (LIPS) measurements of atomic hydrogen in near-adiabatic, atmospheric pressure hydrogen/air flames*. Combustion and Flame, **137**:523-537, 2004
118. Kulatilaka, W.D., Lucht, R.P., Roy, S., Gord, J.R., and Settersten, T.B., *Detection of atomic hydrogen in flames using picosecond two-color two-photon-resonant six-wave-mixing spectroscopy*. Applied Optics, **46**:3921-3927, 2007
119. Goldsmith, J.E.M., *2-Photon-Excited Stimulated-Emission from Atomic-Hydrogen in Flames*. Journal of the Optical Society of America B-Optical Physics, **6**:1979-1985, 1989
120. Kirby, B.J. and Hanson, R.K., *Planar laser-induced fluorescence imaging of carbon monoxide using vibrational (infrared) transitions*. Applied Physics B-Lasers and Optics, **69**:505-507, 1999
121. Kirby, B.J. and Hanson, R.K., *Imaging of CO and CO<sub>2</sub> using infrared planar laser-induced fluorescence*. Proceedings of the Combustion Institute, **28**:253-259, 2000
122. Kirby, B.J. and Hanson, R.K., *CO<sub>2</sub> imaging with saturated planar laser-induced vibrational fluorescence*. Applied Optics, **40**:6136-6144, 2001
123. Kirby, B.J. and Hanson, R.K., *Linear excitation schemes for IR planar-induced fluorescence imaging of CO and CO<sub>2</sub>*. Applied Optics, **41**:1190-1201, 2002
124. Webber, M.E., Kim, S., Sanders, S.T., Baer, D.S., Hanson, R.K., and Ikeda, Y., *In situ combustion measurements of CO<sub>2</sub> by use of a distributed-feedback diode-laser sensor near 2.0  $\mu\text{m}$* . Applied Optics, **40**:821-828, 2001
125. Sanders, S.T., *Wavelength-agile fiber laser using group-velocity dispersion of pulsed super-continua and application to broadband absorption spectroscopy*. Applied Physics B-Lasers and Optics, **75**:799-802, 2002

126. Rothman, L.S., Rinsland, C.P., Goldman, A., Massie, S.T., Edwards, D.P., Flaud, J.M., Perrin, A., Camy-Peyret, C., Dana, V., Mandin, J.Y., Schroeder, J., McCann, A., Gamache, R.R., Wattson, R.B., Yoshino, K., Chance, K.V., Jucks, K.W., Brown, L.R., Nemtchinov, V., and Varanasi, P., *The HITRAN molecular spectroscopic database and HAWKS (HITRAN Atmospheric Workstation): 1996 edition*. Journal of Quantitative Spectroscopy & Radiative Transfer, **60**:665-710, 1998
127. Daily, J.W., *Laser induced fluorescence spectroscopy in flames*. Progress in Energy and Combustion Science, **23**:133-199, 1997
128. Kohse-Höinghaus, K. and Jeffries, J.B., *Applied combustion diagnostics*, Taylor & Francis: New York, 2002
129. Heurlinger, T., *Untersuchungen über die Struktur der Bandenspektren*, C. W. Lindströms bokh.: Lund, 1918
130. Gaydon, A.G., Spokes, G.N., and Vansuchtelen, J., *Absorption Spectra of Low-Pressure Flames*. Proceedings of the Royal Society of London Series a-Mathematical and Physical Sciences, **256**:323-&, 1960
131. Porter, R.P., Clark, A.H., Kaskan, W.E., and Browne, W.E., *A study of hydrocarbon flames*. Symposium (International) on Combustion, **11**:907-917, 1967
132. Bonczyk, P.A. and Shirley, J.A., *Measurement of CH and CN Concentration in Flames by Laser-Induced Saturated Fluorescence*. Combustion and Flame, **34**:253-264, 1979
133. Allen, M.G., Howe, R.D., and Hanson, R.K., *Digital Imaging of Reaction Zones in Hydrocarbon Air Flames Using Planar Laser-Induced Fluorescence of CH and C<sub>2</sub>*. Optics Letters, **11**:126-128, 1986
134. Paul, P.H. and Dec, J.E., *Imaging of Reaction Zones in Hydrocarbon Air Flames by Use of Planar Laser-Induced Fluorescence of CH*. Optics Letters, **19**:998-1000, 1994
135. Luque, J. and Crosley, D.R., *Electronic transition moment and rotational transition probabilities in CH. - I. A<sup>2</sup>Δ-X<sup>2</sup>Π system*. Journal of Chemical Physics, **104**:2146-2155, 1996
136. Hirano, A., Ippommastu, M., and Tsujishita, M., *2-Dimensional Digital Imaging of the CH Distribution in a Natural-Gas Oxygen Flame at Atmospheric-Pressure and Detection of A-State Emission by Means of C-State Excitation*. Optics Letters, **17**:303-304, 1992

137. Bergthorson, J.M., Goodwin, D.G., and Dimotakis, P.E., *Particle streak velocimetry and CH laser-induced fluorescence diagnostics in strained, premixed, methane-air flames*. Proceedings of the Combustion Institute, **30**:1637-1644, 2005
138. Tanahashi, M., Murakami, S., Choi, G.M., Fukuchi, Y., and Miyauchi, T., *Simultaneous CH-OHPLIF and stereoscopic PIV measurements of turbulent premixed flames*. Proceedings of the Combustion Institute, **30**:1665-1672, 2005
139. Vagelopoulos, C.M. and Frank, J.H., *An experimental and numerical study on the adequacy of CH as a flame marker in premixed methane flames*. Proceedings of the Combustion Institute, **30**:241-249, 2005
140. Carter, C.D., Donbar, J.M., and Driscoll, J.F., *Simultaneous CH planar laser-induced fluorescence and particle imaging velocimetry in turbulent nonpremixed flames*. Applied Physics B-Lasers and Optics, **66**:129-132, 1998
141. Watson, K.A., Lyons, K.M., Carter, C.D., and Donbar, J.M., *Simultaneous two-shot CH planar laser-induced fluorescence and particle image velocimetry measurements in lifted CH<sub>4</sub>/air diffusion flames*. Proceedings of the Combustion Institute, **29**:1905-1912, 2003
142. Kothnur, P.S., Tsurikov, M.S., Clemens, N.T., Donbar, J.M., and Carter, C.D., *Planar imaging of CH, OH, and velocity in turbulent non-premixed jet flames*. Proceedings of the Combustion Institute, **29**:1921-1927, 2003
143. Lyons, K.M., Watson, K.A., Carter, C.D., and Donbar, J.M., *On flame holes and local extinction in lifted-jet diffusion flames*. Combustion and Flame, **142**:308-313, 2005
144. Kiefer, J., Li, Z.S., Seeger, T., Leipertz, A., and Aldén, M., *Planar Laser-Induced Fluorescence of HCO for instantaneous flame front imaging in HC flames*. Proceedings of the Combustion Institute, **32**:Submitted, 2008



# Acknowledgements

The end is closing in, but before it is time to say good bye let me take a moment to reflect and thank the people who have been involved, in one way or another.

First of all I would like to thank my main supervisor and the Head of the Division of Combustion Physics, *Professor Marcus Aldén*. I am very grateful for the opportunity that I was given, coming to Combustion Physics already to finish my Masters. Although it took a while, that book is now closed! The possibility to work in one of the world's best laser-spectroscopic laboratories with a variety of international researchers and visitors has been very stimulating.

I would also like to acknowledge my co-supervisor *Zhongshan Li*, without whom I would probably have been completely lost in the laboratory, our chats about everything from molecular physics to Chinese culture and politics has always been very enlightening. Thanks for all the help!

*Mikael Afzelius*, helped me out in the beginning, especially with the filtered Rayleigh work and with MatLab. The hours we spent together in the lab was always fun, sometimes due to our discussions about life and everything and sometimes about work (isn't that life and everything...) and luckily not in French.

*Martin Linvin* and I shared an awful lot of lab-time in the polarization spectroscopy lab, almost always with a little bit of music on, because Martin is not only excellent with the polarizers he is also a true music lover and our evening together with "the Boss" at Ullevi is an evening to remember.

*Professor Per-Erik Bengtsson* is responsible for the teaching at the division. Per-Erik, always well prepared and very seldom in a hurry, you are an inspiration to the others at the division in many respects, especially when it comes to sports. I thought you would get slower over the years but... Nope!

I only had one measurement campaign together with *Jimmy Olofsson* but we have worked side by side for more than 5 years. It has been more than 5 visits to Bishops and about 5 conference or course trips together, the conference trip to Chicago being the one furthest away and the most memorable one, after which Jimmy made a fantastic Chicago DVD. The Combustion Devices course trip to Gothenburg being the shortest, we dropped an ill Jimmy off at his parents in Helsingborg. Jimmy you have become a close friend, and I really miss our long evenings at Bishops discussing a little of everything until closing time. *Hans Seyfried* and I have had very few measurements together but were both involved in a lot of teaching together. We always had the same view of the trade and got good evaluations from the students. Hans being a high school teacher had always the

feeling of giving the students the right amount of information for the given time. Hans, you have become a close and dear friend. For some reason we almost always get to watch soccer when we travel together. In Chicago it was Man. United vs. Bayern München, in Milan it was AC Milan vs. Juventus. You are an easy going person with a great sense of humour and I am looking forward to a continuing strong friendship. *Henrik Bladh* and I have never shared any academic work, but we have shared work. Lately, it has involved the colour of the LU logo, the colour scale of the colour printer and the right font at the right place. We have also organized at least one conference (ADP) and a Jimmy-tribute-Star-Wars-multimedia-lasershow, your live piano part dressed in a homemade Darth Vader suit was priceless! You have a big heart and I am proud to call you my friend. Another person contributing to the division and its great atmosphere is *Gustav Särner*. You are always happy, always nerdy enough with technical details and you always follow your gut feeling, all of which is admirable. CARS has never been my thing but *Fredrik Vestin* lived it for 5 years. I enjoyed your company in Chicago and Heidelberg and I wish you the best of luck up north. *Andreas Ehn*, it took me a while to get a good understanding of your humour but when it sank in you are actually quite funny, one day I might even remember your kids' names, Olle and Ester... *David Sedarsky* is a laid back and really nice guy and I do hope that we will do "the cowboy thing" together some day.

What would Forbrf be without its own engine specialist? *Mattias Richter* was a graduate student when I came to the division. You are always very helpful, an excellent travelling companion and a great guy. For more fundamental physics questions *Joakim Bood* is a good guy to ask. Joakim, you always takes the time to answer questions and I prefer to have you on my basketball team. *Robert Collin* one of the pillars on the lab floor, thanks for all the help and all the songs in the early days. I would here also like to pose a "thank you" to the rest of the "old gang" you know who you are. After about five years at the division I got a new roommate, *Andreas Lantz*. It has been nice to share office with you. You were a bit quiet at the beginning but who can blame you with a roommate like me. Your sense of humour is excellent but please... Turn on the light! As everybody knows a research division would not survive without administrative and technical staff. *Anneli Nilsson* you have always been there when needed, both on work and non-work issues, I am glad to see you happy again, thanks for everything! *Elna Brodin* you were a great deal of help in the beginning. *Cecilia Bille*, you are always helpful on all trivial and non-trivial matters. The engineer *Tomas Wendel*, you came as a saviour and were missed when you left. *Rutger Lorensen* combustion physics own Rock n' Roll star, thanks for all those small things that needed fixing but I am still waiting for that live gig.

I would like to thank all not mentioned by name from the division, you are all contributing to an outstanding atmosphere and I am happy to have been part of it. "Triselkommitten" and its members, both past and present, needs an extra applaud, without somebody organizing events to encourage people to come together the atmosphere at the division would fall, keep up the good work.

Working at a highly international place like Combustion Physics has given me the opportunity to collaborate with people from several different countries, both within and outside Europe. I would like to thank all the visitors and especially *Zeyad Alwahabi, Johannes Kiefer* and *Jan Brübach*. Zeyad, you and I have spent many days and nights together in the lab working on IRPS. You are a great guy and I really enjoyed my visit in Adelaide, who knows... I might come back someday. Johannes, thank you for a very fruitful collaboration, you are very easy to work with and a really nice guy.

For financial support I gratefully thank the *Centre of Combustion Science and Technology, CECOST*, and the *Swedish Research Council*.

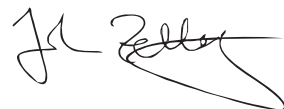
My work at the Department of Physics has not only involved research but also teaching and outreach. With this in mind I would like to thank the UDIF staff, you have not only created the most attractive physics education in Sweden but also the best. *PO Zetterberg, dad*, our work together has meant and taught me a lot. I admire you and am very proud of you. *Tomas Brage* thanks for believing in me, I value our friendship. *Margareta Andersson* you are doing all the work no one else does and you do it splendidly. *Carl-Erik Magnusson*, a little bit of energy-history is never a bad thing. *Martin Andersson*, I miss the good times we had, you are a true physicist but also a great teacher and friend. "*Föreningen Rydbergs Minne*", with the support from UDIF we have created something very unique.

An extra thought goes to the *Fysik & lasershow crew*, both past and present. *Sven, Benny, Hans, Fredrik, Malin, Magnus, Sara, Elias* and all the rest of you, together we have worked endless days and along the way created friends for life. We have made more than 700 shows peaking at ~120 last year, spreading the word of physics to more than 100 000 kids (~20 000 last year alone); now that is what I call an outreach program! In connection to this I would like to thank the Australian crew from University of Melbourne, *Max Thompson* and *Roger Rassool* in particular, for a great collaboration.

I would like to thank all of my friends, *Roger, Jocke, Magnus, Hasse*, and *Erik* to mention a few. You have never let me down and I appreciate and treasure your friendship dearly.

Finally I would like to thank my family: my sister, *Cecilia*, and my parents, *Anette* and *Per Olof*. Cecilia, I admire your strength and I am proud to be your brother. Mom and dad, you have always supported me and given me every possible chance to fulfil my dreams. Your everlasting encouragement has helped me during all these years. Without you I would never have made it this far – Thank You!

Last but not least – thank you my beloved *Sara*. I feel very fortunate to have met you. You are an extraordinary and loving person, with a will of iron and a heart of gold. What we share is, and always will be, very special!



Lund, January 2008



# Summary of papers

- I. In this paper, the use of a single-longitudinal-mode alexandrite laser is described. The laser system is explained and a system for absolute frequency calibration and for computer control of frequency scanning, are taken up. High-resolution two-photon CO laser-induced fluorescence, temperature imaging by filtered Rayleigh scattering (FRS), and infrared polarization spectroscopy (IRPS) for detection of CO<sub>2</sub>, are presented so as to demonstrate the wide diversity of the laser system.  
*I helped set up the absolute frequency control, although Mikael Afzelius and Zhongshan Li did most of the work. I did not participate in the CO measurements but performed and evaluated the FRS measurements. I took part in the IRPS measurements and carried out some of the evaluation. The order of the authors reflects my relative contribution to writing of the manuscript.*
  
- II. The development of UV-FRS at 254 nm is reported here. A single-longitudinal-mode alexandrite laser was utilized to obtain the tunable 254 nm beam, the wavelength coinciding with a strong absorption line of mercury. Mercury was chosen as an atomic filter. The characteristics of the filter and the basic concept of FRS are discussed, measurements in both premixed and diffusion flames being presented and in some cases being compared with earlier measurements.  
*I did the major part of the work in developing FRS, in this aided by Mikael Afzelius and Zhongshan Li, and I performed all the measurements. I was responsible for preparing the manuscript.*
  
- III. Three different techniques – particle-induced velocimetry (PIV) for flow field measurements, laser-induced fluorescence (LIF) for flame front propagation studies, and FRS for temperature measurements – were performed in pairs in a newly developed low-swirl burner as a first step in the development of a detailed large-eddy simulation validation database for turbulent combustion.  
*I performed the FRS measurements and evaluated the data. Hans Seyfried, Jimmy Olofsson and Christian Brackmann performed the OH LIF measurements and Per Petersson and Andreas Nauert the PIV measurements. The burner was controlled by Andreas Nauert. Per Peterson prepared the manuscript, in which I contributed with the part concerning FRS.*

- IV. Surface temperature measurements by thermographic phosphors (TPP) and gas phase measurements close to a stainless steel surface by FRS were conducted. Stray light from the surface was found to be strongly suppressed using FRS. Gas-phase temperature measurements as close as 250  $\mu\text{m}$  from the surface were performed. The results obtained and challenges connected with use of the approach were discussed.  
*I performed the FRS measurements and evaluated the FRS data together with Jan Brübach. Alaa Omrane and Jan Brübach performed the TPP measurements. Jan Brübach had the major responsibility for preparing the manuscript. I contributed in the part concerning FRS.*
- V. Simultaneous PS and LIF measurements of CH were conducted here in a low-pressure flat flame. Counter-propagating beam geometry was utilized in the PS setup for sub-Doppler measurements. PS and LIF lineshapes were compared and saturation energies extracted. The saturation energy for LIF was found to be more than one order of magnitude higher than for PS.  
*I took part in the measurements. Johannes Kiefer carried out most of the data analysis and prepared the major part of the manuscript.*
- VI. A novel nonlinear laser spectroscopic technique for single-shot imaging of atomic hydrogen is reported on here. The hydrogen atoms were pumped to the  $2s$  state via two-photon excitation by a 243 nm laser beam. The population in the  $2s$  state was then probed at 486 nm by use of conventional polarization spectroscopy. A single Nd:YAG pumped optical parametric oscillator was used in the scheme. Single-shot visualization of atomic hydrogen with high spatial resolution was demonstrated.  
*All three authors co-planned the measurements. Martin Linvin and I conducted the measurements. Martin Linvin carried out most of the data evaluation and had the major responsibility for preparing the manuscript.*
- VII. IRPS and IRLIF of  $\text{CO}_2$  were performed at 2  $\mu\text{m}$  using a single-longitudinal-mode alexandrite laser. IRPS and IRLIF lineshapes were extracted. The IRLIF lineshapes were pure Lorentzian, whereas the IRPS lineshapes were Lorentzian-cubed, due to the lack of saturation. The broadening coefficients were determined and were compared to earlier results. The IRPS broadening coefficient was  $\sim 8\%$  larger than for IRLIF.  
*Zeyad Alwahabi, Zhongshan Li and I planned the work and performed the measurements. Zeyad Alwahabi conducted most of the data analysis and was responsible for preparing the manuscript. The theory on line broadening coefficients was applied by Zeyad Alwahabi.*

- VIII. In this study the detection of methane was performed by probing asymmetrical ro-vibrational transitions around  $3000\text{ cm}^{-1}$  by means of IRPS. All the measurements were performed at ambient temperature and pressure in a jet of methane diluted with argon. The signal-to-noise ratio in the measurements was higher than 10000:1. The dependence on methane molefraction and laser pump power was investigated.  
*The authors planned the measurements together. Martin Rupinski (later Linvin) and I conducted all of the measurements and had an equal part in evaluation of the data. We also prepared all of the figures for the manuscript. Zhongshan Li had the major responsibility for preparing the manuscript, Martin and I both contributed to its preparation.*
- IX. In this work the detection of methane and ethane in both cold and reacting flows is reported. The  $\nu_3$ -band of methane and the  $\nu_7$ -band of ethane were both probed by IRPS. The IRPS signal was compared to that of IRLIF, the IRPS signal proving to be much stronger. The detection limit for ethane was estimated as being 50 ppm at ambient temperature and pressure. Measurements of methane in a premixed flat flame were also conducted successfully.  
*Zhongshan Li, Martin Rupinski (later Linvin) and I planned the work. Martin Linvin and I conducted the measurements and evaluated the data. Martin Linvin and I also prepared all of the figures for the manuscript. Zhongshan Li had the major responsibility in preparing the manuscript, Martin and I contributing to this. I presented the work at the 30<sup>th</sup> International Symposium on Combustion.*
- X. Mid-infrared polarization spectroscopy was used to probe non-intrusively and in a spatially-resolved manner the asymmetric C-H stretching vibration of acetylene at  $\sim 3\text{ }\mu\text{m}$ , from 70 mbar to ambient pressure. Dependence of the signal on laser fluence, acetylene molefraction and the colliding partners involved was investigated. Detection of nascent acetylene in a low-pressure premixed methane/oxygen flame was conducted, the methyl radical being detected there.  
*Zhongshan Li did most of the planning, Martin Linvin and I contributing to it. Zhongshan Li, Martin Linvin, Johannes Kiefer and I conducted the measurements. Zhongshan Li did most of the data processing. I prepared most of the figures for the manuscript, which Zhongshan Li had the major responsibility in preparing, Johannes Kiefer and I contributing to the preparation of it.*

- XI. The detection of water and carbon dioxide in low-pressure lean premixed flames is reported in this paper, which aimed at investigating the potential application of IRPS to the diagnosis of reactive flows in the presence of strong background IR emission, as well as the potential interference of hot water lines in measuring CO<sub>2</sub>. The molecules were probed at around ~2.7 μm. Both water and CO<sub>2</sub> were found to have strong absorption. The lines both for water and for CO<sub>2</sub> were simulated using parameters taken from the HITRAN/HITEMP database, satisfactory results being obtained.  
*Zhongshan Li planned the work, Martin Linvin and I performed the measurements together with Zhongshan Li. Zhongshan Li conducted the simulations and had the major responsibility in organizing the manuscript. I prepared some of the figures and proofread the manuscript.*
- XII. In this study, hot water and OH was probed by IRPS in low pressure, lean premixed flames. The interference of the hot waterlines in the detection of minor species was investigated. Temperature estimates obtained by simulation of the water lines (using the HITRAN/HITEMP database) were extracted.  
*Zhongshan Li planned most of the work. Changhong Hu and Zhongshan Li performed most of the measurements, with some assistance by Martin Linvin and me. Zhongshan Li carried out the simulations and prepared the major part of the manuscript. I prepared the figures and proofread the manuscript.*
- XIII. The development of a new and improved excitation scheme for the LIF detection of CH is reported here. An alexandrite laser was used to excite the B-X (0,0) band of CH. The laser was used in both a broadband (8 cm<sup>-1</sup>) and a single mode (100 MHz). Broadband excitation allowed several lines absorption lines to be probed simultaneously. The long pulse duration also helped increase the signal. Single-shot data was collected over a large range of stoichiometries. Use of the technique in a highly turbulent, lean, partially premixed methane/air flame established on a co-axial burner was demonstrated.  
*Zhongshan Li, Johannes Kiefer and I planned and performed the measurements. Zhongshan Li and Johannes Kiefer had the major responsibility for preparing the manuscript. I also contributed to preparing it. Martin Linvin and I prepared the figures.*